

# NANTEN Survey of Molecular Clouds toward the Galactic Center; Association of Compact Astronomical Objects

Tomotake TAKEUCHI,<sup>1</sup> Hiroaki YAMAMOTO,<sup>1</sup> Kazufumi TORII,<sup>1</sup> Natsuko KUDO,<sup>1</sup> Takahiro HAYAKAWA,<sup>1</sup> Akiko KAWAMURA,<sup>1</sup> Norikazu MIZUNO,<sup>2</sup> Toshikazu ONISHI,<sup>1,3</sup> Akira MIZUNO,<sup>4</sup> Hideo OGAWA,<sup>3</sup> and Yasuo FUKUI<sup>1</sup>

<sup>1</sup>Department of Astrophysics, Nagoya University, Furo-cho, Chikusa-ku, Nagoya 464-8602

tomotake@aphys.nagoya-u.ac.jp, fukui@aphys.nagoya-u.ac.jp

<sup>2</sup>National Astronomical Observatory of Japan, 2-21-1 Osawa, Mitaka, Tokyo 181-8588

<sup>3</sup>Department of Physical Science, Osaka Prefecture University, Sakai, Osaka 599-8531

<sup>4</sup>Solar-Terrestrial Environment Laboratory, Nagoya University, Furo-cho, Chikusa-ku, Nagoya 464-8601

(Received 2008 March 13; accepted 2010 March 3)

## Abstract

In order to better understand molecular clouds and their properties toward the Galactic center region, we have analyzed the NANTEN database of  $^{12}\text{CO}$  ( $J = 1-0$ ) and  $^{13}\text{CO}$  ( $J = 1-0$ ) to search for associations with candidates for young high-mass star-forming regions, such as IRAS point sources, radio continuum sources, recombination line sources, maser line sources, and other molecular line sources. We have also compared the data with TeV  $\gamma$ -ray sources. The analyzed region covers  $-12^\circ \leq l \leq 12^\circ$  and  $-1.5^\circ \leq b \leq 1.5^\circ$  for  $^{12}\text{CO}$ , and  $-6^\circ \leq l \leq 8^\circ$  and  $-1^\circ \leq b \leq 1^\circ$  for  $^{13}\text{CO}$ . As a result, we identified 167 IRAS point sources, 73 recombination line sources, 58 maser sources, 107 radio continuum sources, and 77 molecular line sources associated with 169 positions with the CO emission. The associations among the objects with known velocity are fairly certain (68%), while those with only positional coincidence are less reliable (32%). We present a catalog of these CO clouds in a form useful for future follow-up studies. As specific examples of usage of the catalog, we highlight three outstanding regions of active star formation: W 28, W 30, and W 31. In particular, we have discovered that the W 30 region shows a striking correlation between the extended TeV  $\gamma$ -ray source and the molecular gas. This is a second case of such a good correlation identified from the NANTEN dataset subsequent to W 28 (Aharonian et al. 2008, A&A, 481, 401). We suggest that the pulsar PSR J1803–2137 near the molecular features may play a role in  $\gamma$ -ray production. The W 31 region exhibits another active star formation, while no  $\gamma$ -ray source is yet known.

**Key words:** ISM: clouds — ISM: H II regions — ISM: supernova remnants

## 1. Introduction

The central 1 kpc of the Galaxy, the high-density concentration of stars and the interstellar matter, exhibits unusual properties quite different from those in the Galactic disk, including violent motions and high temperatures of the molecular gas and strong ordered magnetic fields (see e.g., Morris 2006). Many unknowns including crucial processes, like star formation, remain in our astronomical and astrophysical understanding of the Galactic center. It is generally difficult to disentangle the objects toward the Galactic center into the actual central components within  $\sim 1$  kpc in  $R$  and the individual disk components both in the foreground and background, because many objects overlap along the line of sight in the sky, and also in velocity space. Nonetheless, we recognize that there are increasing demands for separating objects toward the Galactic center in distance in order to analyze and interpret new observational results at various wavelengths. These new observations include the Spitzer (Ramírez et al. 2008; Hinz et al. 2009) and AKARI (Murakami et al. 2007) surveys at infrared wavelengths and TeV  $\gamma$ -ray observations with the High Energy Stereoscopic System (hereafter HESS) and other instruments (Aharonian et al. 2006).

The 21 cm line spectrum of atomic hydrogen has been most

extensively used to probe the interstellar gas in the Galaxy, but this spectrum suffers from serious foreground/background contamination of the Galactic disk over a velocity range of  $\sim 100 \text{ km s}^{-1}$  centered at  $0 \text{ km s}^{-1}$  in  $V_{\text{LSR}}$  toward the Galactic center (Kerr 1967). The CO  $J = 1-0$  emission at 2.6 mm wavelength offers a better tool with less contamination than H I. This is because the velocity range of the disk CO emission is narrower than H I, typically less than  $\sim 40 \text{ km s}^{-1}$ , centered at  $0 \text{ km s}^{-1}$ , and because the CO emission is much more clumpy than H I, allowing us to look deeper along the line of sight.

Most of the previous molecular line studies toward the Galactic center focused on the central molecular zone (CMZ) including the Sgr A and B2 molecular clouds, which lie within a few degrees, corresponding to a few 100 pc, of the center (e.g., Scoville et al. 1975; Fukui et al. 1977; Güsten & Henkel 1983; Oka et al. 1998; Tsuboi et al. 1999; Martin et al. 2004; see also for a recent review, Güsten & Philipp 2004). Larger areas of kpc scales toward the Galactic center were covered in the  $^{12}\text{CO}$   $J = 1-0$  and  $2-1$  emission lines, most usual probes of molecular gas, at lower angular resolutions of  $8.8'$  and  $9'$  by Bitran et al. (1997) [ $(25^\circ \times 2^\circ)$  in  $(\Delta l \text{ and } \Delta b)$ ] and by Sawada et al. (2001) [ $(12^\circ \times 4^\circ)$  in  $(\Delta l \text{ and } \Delta b)$ ]. However, these observations are too coarse to resolve individual clouds and to identify associated objects. NANTEN, a 4-m millimeter-wave

telescope in Chile, has carried out the most extensive observations toward the Galactic center in  $^{12}\text{CO}$   $J = 1-0$  emission covering  $\pm 5^\circ$  in galactic latitude along the Galactic plane at a  $4'$  grid spacing with a  $2.6'$  beam. These observations have offered a kpc-scale molecular view of the region at  $\sim 10$  pc resolution for the first time. By using this NANSEN dataset, Fukui et al. (2006) discovered two molecular loops toward  $l \sim 355^\circ\text{--}359^\circ$ , and interpreted them as being due to magnetic flotation, providing a viable tool to explain the violent states of molecular gas in the Galactic center.

Molecular clouds are the principal sites of star formation, and it is important to have comprehensive knowledge concerning the properties of molecular clouds in our efforts to understand the evolution of the Galaxy. Toward a goal to reveal details of star formation in the Galactic center region, we need to acquire a uniform view of the association between molecular clouds and other astronomical objects, particularly young high-mass stars and their candidates. For this purpose we have analyzed the NANSEN CO dataset for a wide region of  $\pm 12^\circ$  in galactic longitude, covering a latitude range of  $3^\circ$  centered on the mid-plane, and have made a catalog of CO clouds associated with known astronomical objects that radiate in the infrared and radio wavelengths. Radiations at radio and infrared wavelengths are not subject to dust extinction, like optical radiation, and are suitable to be compared with the CO dataset.

The present study will allow us to discern candidates of youngest high-mass stars by association with molecular clouds, while we are not able to reach low-mass stars because of limited sensitivities at distances greater than a few kpc. A straightforward follow-up of the present catalog is to proceed to more intensive studies focused on an object at various wavelengths, which may lead to a better understanding of individual star formation, including dense cloud cores and the accurate determination of a distance. Also, the spatial and kinematic distributions of a molecular cloud associated with multiple young objects will help us to identify physical association among young stars. Finally, we shall be able to construct an improved view of high-mass young stars toward the Galactic center, and to quantify the star-formation activity in the central 1 kpc by eliminating the disk components.

The following objects, classified into five types, are all good candidates of high-mass star-forming regions. They are likely to be associated with molecular clouds, if they are young enough and if cloud dissipation is not yet significant. The astronomical objects utilized are in the SIMBAD database, as divided into the five types: (1) IRAS point sources (candidates for embedded young stars), (2) radio recombination line sources (candidates for young OB stars), (3) maser line sources [candidates for young OB stars and supernova remnants (SNRs)], (4) other molecular line sources (candidates for massive cloud cores), and (5) radio continuum sources (candidates for H II regions ionized by young OB stars). Considering the highly complicated properties of the region, we did not intend to make a fully reliable identification of the physical association in the present study. Rather, we intended to make a uniform list of candidate molecular features that are worthy of future follow-up studies at various wavelengths. Nonetheless, some of the associated sources seem to be very

firm and enlightening, as discussed in section 5.

In addition to young stars, the association of molecular clouds with  $\gamma$ -ray sources is of keen interest. One of such examples is the W28 region, where Aharonian et al. (2008) discovered that molecular clouds observed with NANSEN show a remarkably good spatial correlation with a TeV  $\gamma$ -ray distribution. This offers one of the most promising candidates in the Galaxy for  $\gamma$ -ray production via interactions between cosmic-ray protons and molecular gas, followed by neutral pion decay (Y. Fukui et al. 2010, in preparation). These high-energy observations are being rapidly developed and source catalogs are continuously being revised. They include the HESS collaboration, the Fermi project etc. In such a fluid situation, it is required to identify candidate molecular clouds associated with the  $\gamma$ -ray sources by morphology only like in the case of W 28, while we need follow-up studies to firmly establish the physical connection. The present catalog is applied for such targets as well.

The present paper is organized as follows. We give details of the NANSEN CO datasets in section 2 and astronomical objects to be compared with CO in section 3. We present the CO velocity channel maps, the method of comparison, and the lists of identified objects in section 4 and discuss three outstanding star-forming regions in section 5. We then conclude the present study in section 6.

## 2. Observations

### 2.1. $^{12}\text{CO}$

We used the NANSEN  $^{12}\text{CO}$  ( $J = 1-0$ ) Galactic Plane Survey dataset (Mizuno & Fukui 2004) in the present analysis. The observations were carried out with NANSEN, a millimeter-wave telescope of Nagoya University, located at Las Campanas Observatory in Chile. The diameter of the telescope was 4 m, which provided a half-power beamwidth (HPBW) of  $2.6'$  at 115 GHz. The receiver was an SIS mixer (Ogawa et al. 1990), providing a system temperature of  $\sim 250$  K in the single side band, including the atmosphere toward the zenith. The spectrometer was an acousto-optical spectrometer (AOS) with 2048 channels. The frequency coverage and resolution were 250 MHz and 250 kHz, corresponding to a velocity coverage of  $\pm 300$  km s $^{-1}$  and a velocity resolution of 0.65 km s $^{-1}$ , respectively, at 115 GHz. The observations were carried out by position switching at a  $4'$  grid spacing. The integration time per point was  $\sim 5$  s, and the r.m.s. noise fluctuation of the spectral data was  $\sim 0.45$  K at a velocity resolution of 0.6 km s $^{-1}$ . The  $^{12}\text{CO}$  distribution is shown as the distribution of the total intensity integrated from  $-300$  km s $^{-1}$  to  $300$  km s $^{-1}$  in figure 1 and a longitude–velocity diagram integrated over  $3^\circ$  in galactic latitude in figure 2. Figure 1 shows that most of the CO emission in the Galactic plane is confined to within  $|b| \sim 1^\circ$ , and we analyzed the data in the latitude range from  $b = -1.5$  to  $1.5$ . The longitude range was chosen to be within  $|l| = 12^\circ$  so as to ensure a full coverage of the emission within 1 kpc of the Galactic center. The total number of observed positions was  $\sim 16200$ . At a distance of  $\sim 8$  kpc to Sgr A\*,  $12^\circ$  corresponds to  $\sim 1.7$  kpc. Figure 2 shows that the broad emission originating within 1 kpc of the center has much broader velocity dispersions than the disk emission, which is

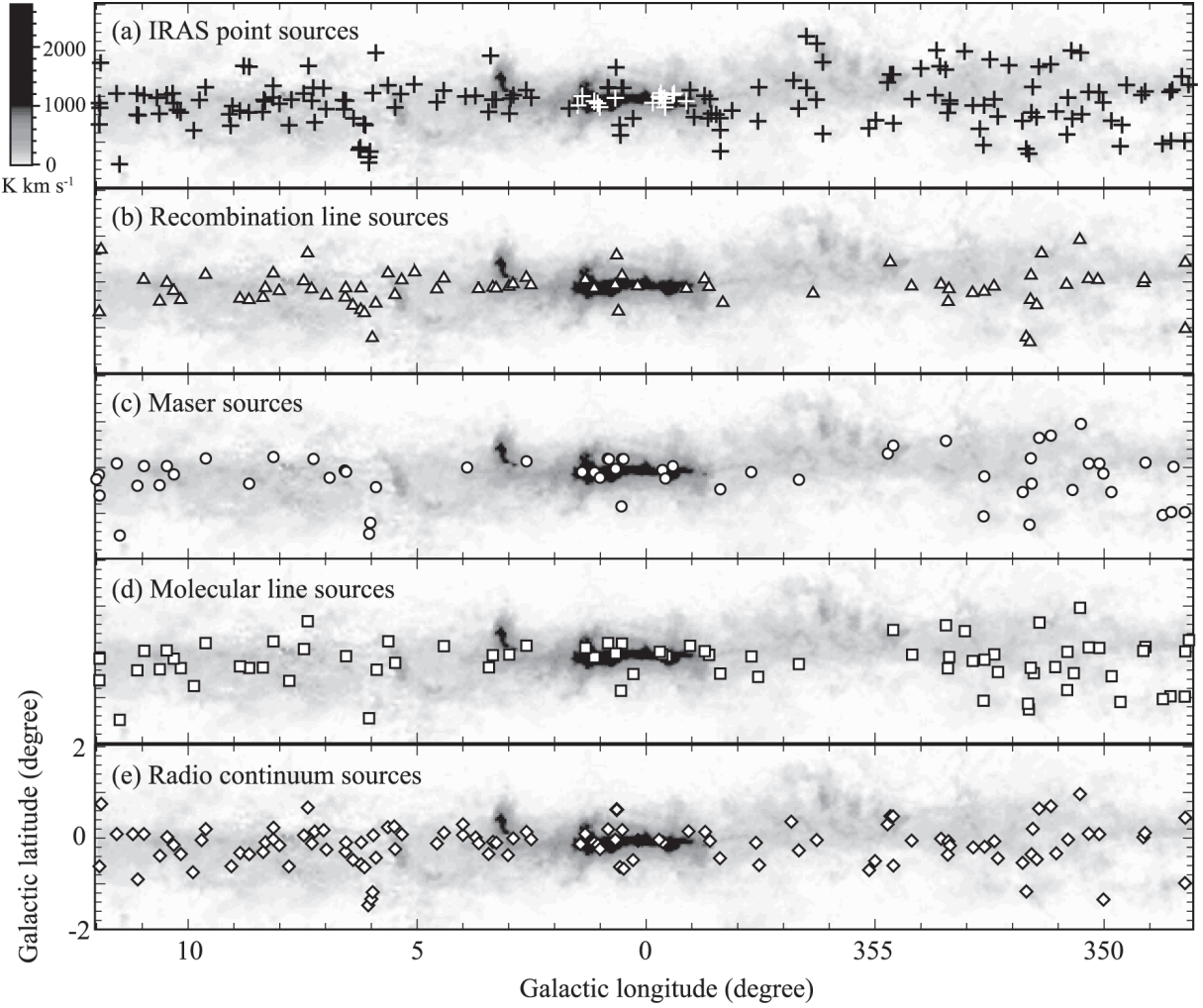


**Fig. 1.**  $^{12}\text{CO}$  velocity-integrated intensity distributions (gray scale image) overlaid with (a) IRAS point sources (crosses), (b) radio recombination line sources (triangles), (c) maser sources (circles), (d) other molecular line sources (squares), and (e) radio continuum sources (diamonds).

confined to within an  $\sim 30 \text{ km s}^{-1}$  velocity width.

## 2.2. $^{13}\text{CO}$

We also used the  $^{13}\text{CO}$  ( $J = 1-0$ ) NANTEN Galactic Plane Survey dataset obtained with the same telescope, NANTEN, and the SIS receiver. The beamwidth was  $2.7'$  at 110 GHz, with a typical systems temperature of  $\sim 130 \text{ K}$  in the single side band, including the atmosphere toward the zenith. The observations were made at a  $2'$  grid spacing, and the r.m.s. noise fluctuations were typically  $\sim 0.2 \text{ K}$  for a  $0.1 \text{ km s}^{-1}$  velocity resolution. A position-switching technique was used. We used data covering  $l = -6^\circ$  to  $8^\circ$  and  $|b| \leq 1^\circ$ , and the total number of observed points was  $\sim 14600$ .

## 3. Astronomical Objects for Comparison

Figure 1 summarizes the distributions of the objects compared with the CO distribution in the present work, including the IRAS sources (a), radio recombination line sources (b), maser line sources (c), other molecular lines (d), and radio continuum sources (e). We shall give more details of

these objects in the following. The results of these identifications are listed in table 1.

Column (1), CO cloud name in  $l$  and  $b$ ; Column (2),  $V_{\text{LSR}}$  of CO determined by a Gaussian fitting; Column (3), IRAS source name; Column (4), criteria of the IRAS source, ultra compact H II region (UCH II) or planetary nebula (PN); Column (5),  $V_{\text{LSR}}$  of the radio recombination line sources; Column (6),  $V_{\text{LSR}}$  of maser line sources; Column (7),  $V_{\text{LSR}}$  of other molecular line sources; Column (8), radio continuum sources; “D” stands for detected; Column (9), rank; Column (10), additional remarks.

### 3.1. IRAS Point Sources

IRAS observed in four wavelength bands centered at  $12 \mu\text{m}$ ,  $25 \mu\text{m}$ ,  $60 \mu\text{m}$ , and  $100 \mu\text{m}$ . The ratio of the flux densities in the 4 bands is one of the most powerful tools for discriminating between different classes of objects, such as high-mass star-forming regions (Wood & Churchwell 1989), PNe (Pottasch et al. 1988), young stellar objects (YSOs) (Chan et al. 1996; Felli et al. 2002), and external galaxies. We selected the sources in the present area as listed in table 1.

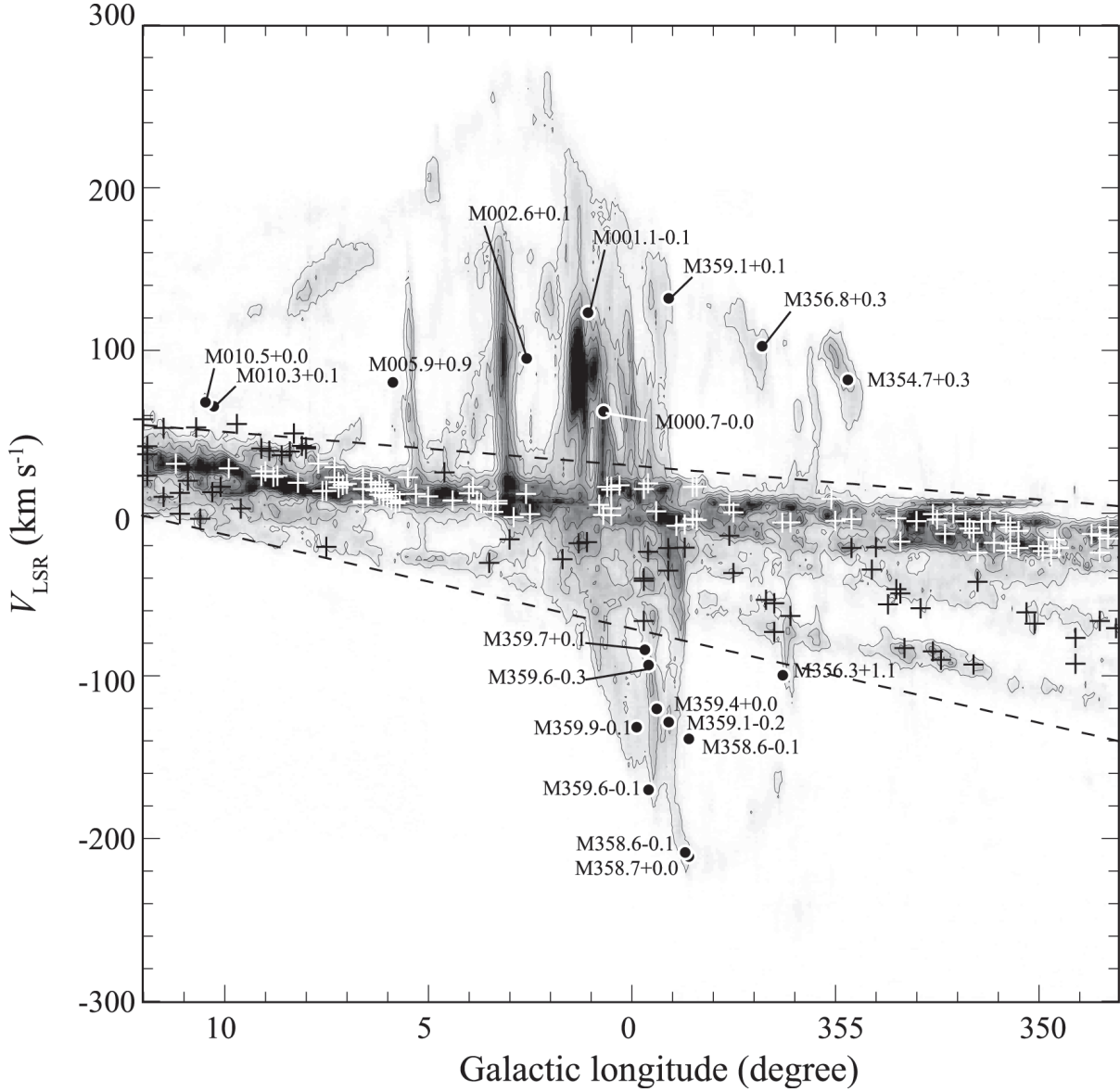


**Fig. 2.** Position–velocity diagram of  $^{12}\text{CO}$  (gray scale image) integrated over the galactic latitude range from  $b = -1.5^\circ$  to  $1.5^\circ$ . Annotated symbols indicate the positions of CO molecular clouds that are associated with astronomical objects; filled circles are those identified to be located in the Galactic center because of their large velocity separation from the disk features and the 3-kpc arm, and the crosses are tentatively assigned to be in the Galactic disk or in the 3-kpc arm. The two dashed lines show the adopted boundaries to discriminate the central sources from the rest.

### 3.1.1. Ultra compact H II regions

H II regions are markers where massive OB stars have ionized their environmental gas, and where high-mass star formation is taking place. In particular, ultra compact (UC) H II regions are representative of active star-forming regions. UCH II regions typically have electron densities greater than  $\sim 10^4 \text{ cm}^{-3}$ , diameters less than  $\sim 0.1 \text{ pc}$ , and an ambient temperature of  $\sim 30 \text{ K}$  (Wood & Churchwell 1989). Their spectral energy distributions approximate a blackbody with its emission peak at around  $100 \mu\text{m}$ . Analyses of IRAS flux densities can be powerful for identifying such regions, since almost the entire sky has been surveyed by IRAS at the far infrared wavelengths. In order to distinguish embedded UCH II regions from other IRAS sources, Wood and Churchwell

(1989) derived the following color criteria, using the  $12 \mu\text{m}$ ,  $25 \mu\text{m}$ , and  $60 \mu\text{m}$  bands:

$$\log(F_{25}/F_{12}) \geq 0.57 \quad \text{and} \quad \log(F_{60}/F_{12}) \geq 1.30. \quad (1)$$

From our initial list of 189 IRAS sources, a total of 77 UCH II region candidates were selected according to their selection criteria (figure 3). In those CO clouds associated with these IRAS point sources, active star formation is likely to be occurring.

### 3.1.2. Planetary nebulae

About 2000 PNe are now known to exist in the Galaxy. In our survey, around twenty isolated molecular clouds associated with faint IRAS point sources flux are found. Moreover, some of them are also associated with thermal radio continuum

**Table 1.** List of CO clouds associated with astronomical objects.\*

CO cloud	$V_{\text{LSR}}$ (km s $^{-1}$ )	IRAS	Criteria	Radio recombination (km s $^{-1}$ )	Maser line (km s $^{-1}$ )	Molecular line (km s $^{-1}$ )	Radio source	Rank $^{\dagger}$	Remarks
M 348.1+0.3	-70.3	17095–3837	UCH II	—	—	-70.4 <sup>(9)</sup>	—	a	
M 348.3–1.0	-15.3	17149–3916	UCH II	-18 <sup>(15)</sup>	-12 <sup>(70)</sup>	-13.7 <sup>(9)</sup>	—	a	
M 348.3+0.4	-8.5	17092–3823		-12 <sup>(15)</sup> , -14.0 <sup>(25)</sup>	—	-7 <sup>(15)</sup>	—	a	RCW 120
M 348.5+0.1	-65.9	17111–3824		—	-65.2 <sup>(27)</sup>	—	—	a	CTB 37A
	-23.9	17110–3823		—	-23.3 <sup>(27)</sup>	—	—	a	CTB 37A
M 348.5–1.0	-13.5	17158–3901	UCH II	—	-19.7 <sup>(12)</sup> , -16 <sup>(18)</sup> , -13 <sup>(70)</sup>	-13.4 <sup>(9)</sup> , -16.16 <sup>(76)</sup>	D <sup>(44)</sup>	a	
M 348.7–1.1	-12.5	17167–3854		-13 <sup>(15)</sup>	-8 <sup>(17)</sup> , -11 <sup>(18)</sup> , -9.1 <sup>(69)</sup>	-13.4 <sup>(15)</sup>	D <sup>(44)</sup>	a	RCW 122
M 349.1+0.1	-76.3	17130–3756		-74 <sup>(15)</sup>	-77 <sup>(17)</sup> , -78.0 <sup>(67)</sup> , -76.7 <sup>(69)</sup>	-76.7 <sup>(15)</sup>	D <sup>(77)</sup>	a	
M 349.1+0.0	-92.1	17135–3755		-92 <sup>(15)</sup>	—	-97 <sup>(15)</sup>	D <sup>(77)</sup>	a	
M 349.5+0.2	-21.0	17136–3731		—	—	—	—	c	
M 349.6–0.6	-16.0	17175–3757		—	—	—	—	c	
M 349.7–1.1	-25.3	17195–3811	UCH II	—	—	-26.5 <sup>(9)</sup>	—	a	
M 349.9–0.5	-23.0	17178–3742	UCH II	-25 <sup>(15)</sup>	—	-25.1 <sup>(9)</sup>	—	a	
M 350.0–1.3	-20.0	17216–3801		—	-19.7 <sup>(4)</sup> , -18.3 <sup>(12)</sup> , -21 <sup>(18)</sup>	—	D <sup>(5)</sup>	a	
M 350.1+0.1	-67.5	17160–3707	UCH II	-69 <sup>(15)</sup> , -70.3 <sup>(48)</sup>	-74 <sup>(17,70)</sup> , -66.6 <sup>(69)</sup>	-69.5 <sup>(9)</sup> , -68 <sup>(15)</sup>	D <sup>(5,77)</sup>	a	
M 350.3+0.1	-60.6	17166–3656	UCH II	-66.1 <sup>(48)</sup>	-64 <sup>(12)</sup> , -62.2 <sup>(69)</sup> , -66 <sup>(70)</sup>	-63.5 <sup>(9)</sup>	D <sup>(5,77)</sup>	a	
M 350.5–0.4	-21.0	17190–3705		—	—	—	—	c	
M 350.5+1.0	-10.6	17136–3617	UCH II	-10 <sup>(15)</sup> , -11.4 <sup>(48)</sup>	-11 <sup>(18)</sup>	-10.3 <sup>(9)</sup>	D <sup>(44)</sup>	a	GMC 350.5+1.0
M 350.7–0.5	-18.4	17200–3658	UCH II	—	-14.5 <sup>(12)</sup> , -14.0 <sup>(53)</sup>	-18.6 <sup>(9)</sup>	—	a	
M 350.7+0.9	-8.2	17141–3606		—	—	—	—	c	GMC 350.5+1.0
M 350.8+0.0	-5.5	17184–3638	UCH II	-5 <sup>(15)</sup> , 0.3 <sup>(48)</sup>	—	-5.7 <sup>(58)</sup>	D <sup>(5,77)</sup>	a	
M 350.8–0.8	-22.6	17218–3704		—	—	-20.41 <sup>(26)</sup>	—	a	
M 351.1–0.3	-17.9	17204–3636	UCH II	—	—	-18.0 <sup>(9)</sup>	D <sup>(5,77)</sup>	a	
M 351.2+0.7	-4.5	17165–3554		—	-9.65 <sup>(4)</sup> , -5 <sup>(17)</sup> , -5.4 <sup>(69)</sup>	-3.5 <sup>(56)</sup>	D <sup>(5,77)</sup>	a	NGC 6334
M 351.4+0.7	-5.0	17175–3544	UCH II	-3 <sup>(15)</sup> , -3.6 <sup>(48)</sup>	-9.1 <sup>(12)</sup> , -10 <sup>(53)</sup> , -6.7 <sup>(69)</sup>	-6.9 <sup>(9)</sup> , -8.8 <sup>(51)</sup> , -4.28 <sup>(54)</sup>	D <sup>(77)</sup>	a	NGC 6334F
M 351.5+0.2	-41.8	17197–3552		-44.8 <sup>(48)</sup>	-39 <sup>(14)</sup>	—	D <sup>(5,77)</sup>	a	
M 351.5–0.5	-23.9	17221–3619	UCH II	-21 <sup>(15)</sup>	—	-22.3 <sup>(9)</sup>	D <sup>(52)</sup>	a	
M 351.6–1.3	-11.8	17258–3637	UCH II	-13 <sup>(15)</sup> , -14.0 <sup>(48)</sup>	-13 <sup>(18,67)</sup>	-11.9 <sup>(9)</sup>	—	a	GMC 351.7–1.1
M 351.6–0.3	-92.6	17220–3609	UCH II	-94 <sup>(15)</sup> , -91.8 <sup>(48)</sup>	-97.6 <sup>(12)</sup> , -95 <sup>(53)</sup>	-98.5 <sup>(9)</sup>	D <sup>(5,77)</sup>	a	
M 351.7–1.1	-9.1	17256–3631	UCH II	-13 <sup>(15)</sup>	—	-8.8 <sup>(62)</sup>	D <sup>(44)</sup>	a	GMC 351.7–1.1
M 351.8–0.5	-4.7	17233–3606	UCH II	—	-2 <sup>(12)</sup> , 1.0 <sup>(69)</sup>	-3.4 <sup>(9)</sup> , -3.9 <sup>(51)</sup>	D <sup>(77)</sup>	a	
M 352.1+0.7	0.1	17192–3510		—	—	—	—	c	
M 352.3–0.5	-12.4	17244–3536	UCH II	—	—	-10.8 <sup>(9)</sup>	D <sup>(5,77)</sup>	a	
M 352.4–0.1	-89.8	17231–3520	UCH II	-89 <sup>(15)</sup> , -87.0 <sup>(48)</sup>	—	-90.2 <sup>(9)</sup> , -86 <sup>(15)</sup>	D <sup>(5)</sup>	a	GMC 352.6–0.2
M 352.5+0.8	-3.6	17199–3446	UCH II	—	—	-2.7 <sup>(9)</sup>	—	a	
M 352.6–1.1	-0.3	17278–3541	UCH II	—	0.0 <sup>(53)</sup> , -3 <sup>(70)</sup>	-0.0 <sup>(3)</sup> , -0.4 <sup>(9)</sup>	—	a	
M 352.6–0.2	-84.5	17242–3513	UCH II	-82 <sup>(15)</sup> , -81.9 <sup>(48)</sup>	-96.0 <sup>(53)</sup> , -96 <sup>(70)</sup>	-86.5 <sup>(9)</sup>	—	a	GMC 352.6–0.2#
M 352.9–0.2	-58.2	17249–3501	UCH II	-58 <sup>(15)</sup>	—	-56.0 <sup>(9)</sup>	D <sup>(5,77)</sup>	a	
M 353.0+0.5	-4.6	17228–3430	UCH II	—	—	-3.4 <sup>(9)</sup>	—	a	NGC 6357
M 353.3–0.2	-82.6	17262–3435	UCH II	-82 <sup>(15)</sup>	—	-81.2 <sup>(9)</sup>	D <sup>(5,77)</sup>	a	
M 353.4–0.3	-17.2	17271–3439	UCH II	-16.2 <sup>(48)</sup>	-20.7 <sup>(11)</sup> , -19.7 <sup>(12)</sup> , -20.0 <sup>(53)</sup>	-17.5 <sup>(3)</sup> , -16.7 <sup>(9,51)</sup>	D <sup>(5,77)</sup>	a	
M 353.4–0.1	-49.0	17258–3432		-54 <sup>(15)</sup> , -58.1 <sup>(48)</sup>	—	-51.8 <sup>(58)</sup>	D <sup>(77)</sup>	a	
M 353.5+0.6	-46.4	17234–3405	UCH II	—	-45 <sup>(12)</sup> , -50 <sup>(53,70)</sup>	-47.1 <sup>(9)</sup>	—	a	
M 353.5+1.0	-2.9	17223–3341		—	—	—	—	c	
M 353.7+0.0	-55.6	17262–3413		-56.7 <sup>(48)</sup>	—	—	D <sup>(5,77)</sup>	a	
M 354.0+0.6	-20.7	17248–3338		—	—	—	—	c	
M 354.1–0.1	-34.3	17279–3350	UCH II	-33 <sup>(15)</sup> , -34.1 <sup>(48)</sup>	—	-32.3 <sup>(9)</sup>	D <sup>(5,28,77)</sup>	a	
M 354.6–0.6	-3.4	17312–3347		—	—	—	D <sup>(71)</sup>	c	SNR G354.8–0.8\$
M 354.6+0.5	-21.1	17269–3312	UCH II	—	-15.4 <sup>(12)</sup> , -16 <sup>(18)</sup> , -23 <sup>(70)</sup>	-21.0 <sup>(9)</sup>	D <sup>(77)</sup>	a	
	17271–3309	UCH II		-27 <sup>(15)</sup> , -21.2 <sup>(48)</sup>	—	-20.9 <sup>(9)</sup>	D <sup>(77)</sup>	a	
M 354.7+0.3	82.2	17279–3311	UCH II	—	95 <sup>(12)</sup> , 93.7 <sup>(69)</sup> , 94 <sup>(70)</sup>	—	D <sup>(5)</sup>	b	
M 355.0–0.5	-4.5	17319–3326	UCH II	—	—	—	D <sup>(71)</sup>	a	SNR G354.8–0.8\$
M 355.1–0.7	9.0	17331–3324		—	—	—	D <sup>(20)</sup>	c	
M 356.1–0.8	-5.4	17361–3237		—	—	—	—	c	
M 356.1+0.7	-62.8	17299–3146		—	—	—	—	c	
M 356.3+1.1	-99.9	17286–3126		—	—	—	—	c	
M 356.3–0.1	-5.5	17335–3206	UCH II	-2 <sup>(15)</sup> , -4.0 <sup>(48)</sup>	—	—	D <sup>(5,31)</sup>	a	SNR G356.3–0.3\$
M 356.5+0.2	-55.0	17330–3147		—	—	—	—	c	
M 356.5+1.3	-72.6	17286–3109		—	—	—	—	c	
M 356.7–0.3	-52.9	17352–3153	UCH II	—	-52.4 <sup>(12)</sup> , -54 <sup>(53,70)</sup>	-52.3 <sup>(9)</sup>	D <sup>(5)</sup>	a	
M 356.8+0.3	103.0	17331–3127		—	—	—	D <sup>(5,77)</sup>	a	
M 357.5+0.2	-36.5	17356–3054		—	—	—	—	c	
M 357.5–0.5	0.8	17385–3116	UCH II	—	—	0.9 <sup>(9)</sup>	D <sup>(77)</sup>	a	
M 357.6–0.1	-13.6	—		—	-12.4 <sup>(27)</sup>	9 <sup>(60)</sup>	D <sup>(61,63)</sup>	a	MSH 17–39
	5.4	—		—	—	—	D <sup>(61,63)</sup>	a	MSH 17–39
M 358.4–1.2	16.6	17432–3055		—	—	—	—	c	
M 358.4–0.5	-3.9	17403–3032	UCH II	—	1.0 <sup>(53)</sup> , -3.1 <sup>(65)</sup> , 2 <sup>(70)</sup>	-3.0 <sup>(9)</sup>	D <sup>(77)</sup>	a	
M 358.5–0.4	-3.2	17402–3025		-4.0 <sup>(49)</sup>	—	—	—	a	
M 358.5–0.4	16.3	17404–3019		—	—	—	—	c	
M 358.6–0.1	-211.6	17392–3008	UCH II	-212 <sup>(15)</sup> , -211.7 <sup>(23)</sup>	—	—	D <sup>(1,5)</sup>	a	Sgr E33
	-138.9	—		—	—	—	—	c	
M 358.7–0.5	-20.9	17410–3019		—	—	—	—	c	
	-6.6	—		—	—	—	—	c	
M 358.7+0.0	-208.9	17392–2959	UCH II	-210.1 <sup>(23)</sup>	—	—	D <sup>(5)</sup>	a	Sgr E35
M 358.9–0.5	-7.5	17416–3003		—	-5.57 <sup>(74)</sup>	—	—	a	SNR G359.1–0.5\$
M 359.1+0.1	132.4	17395–2939		—	—	135 <sup>(38)</sup> , 133.9 <sup>(39)</sup>	D <sup>(77)</sup>	a	

Table 1. (Continued)

CO cloud	$V_{\text{LSR}}$ (km s $^{-1}$ )	IRAS	Criteria	Radio recombination (km s $^{-1}$ )	Maser line (km s $^{-1}$ )	Molecular line (km s $^{-1}$ )	Radio source	Rank $^{\dagger}$	Remarks
M 359.1–0.2	–128.3	17410–2948		—	—	—	—	c	
	–21.2			—	—	—	—	c	
M 359.1–0.1	–35.0	17408–2942		—	—	—	—	c	
M 359.4+0.0	–120.5	17409–2926		—	—	—	—	c	
M 359.4+0.1	1.5	17409–2923		—	8 <sup>(66)</sup>	1 <sup>(33)</sup>	—	a	
M 359.6–0.1	–23.5	17419–2921		—	—	–20 <sup>(38)</sup> , –18.2 <sup>(39)</sup>	—	a	
M 359.6–0.1	–170.3	17416–2916		—	—	—	—	c	
M 359.6–0.3	–93.7	17423–2924		—	–87 <sup>(66)</sup>	–102 <sup>(33)</sup>	—	b	
	18.5			—	22.5 <sup>(10)</sup> , 20.2 <sup>(16)</sup>	—	—	a	
M 359.7–0.1	–41.3	17418–2914	UCH II	—	20 <sup>(62)</sup>	–42.7 <sup>(9)</sup>	D <sup>(1)</sup>	a	GMC 359.7–0.1
	15.1			—	—	—	D <sup>(1)</sup>	a	
M 359.7+0.1	–84.3	17413–2909		—	—	—	—	c	
M 359.7–0.0	–65.8	17418–2910		—	—	–61.4 <sup>(39)</sup>	D <sup>(5)</sup>	a	
	–39.9			—	—	–33, –38 <sup>(38)</sup>	D <sup>(5)</sup>	a	GMC 359.7–0.1
M 359.9–0.1	–131.7	17426–2907		—	—	—	—	c	
M 000.3–0.5	17.4	17449–2855	UCH II	—	—	18.5 <sup>(9)</sup>	D <sup>(1,77)</sup>	a	
M 000.5–0.7	14.8			—	—	—	D <sup>(1,44)</sup>	c	
M 000.5+0.1	3.3 $^{\ddagger}$	17429–2832		—	–5.5 <sup>(12)</sup> , 0.8 <sup>(53)</sup> , 1 <sup>(70)</sup>	—	—	a	
M 000.5+0.2	–1.0 $^{\ddagger}$	17430–2822	UCH II	–2.3 <sup>(49)</sup>	0 <sup>(62)</sup> , 3 <sup>(70)</sup>	–3.8 <sup>(9)</sup>	D <sup>(1,5)</sup>	a	
M 000.5–0.7	16.5	17462–2845		16.8 <sup>(55)</sup>	—	—	D <sup>(1,44)</sup>	a	
M 000.6–0.9	16.4	17470–2853		—	13.8 <sup>(16)</sup> , 13.6 <sup>(69)</sup> , 14 <sup>(70)</sup>	14 <sup>(41)</sup> , 16.6 <sup>(56)</sup>	D <sup>(1,44)</sup>	a	RCW 142
M 000.7+0.6	–0.8	17415–2801		3.7 <sup>(49)</sup>	—	—	D <sup>(1,34)</sup>	a	
M 000.7–0.0	62.6	17441–2822	UCH II	62 <sup>(24)</sup> , 65.2 <sup>(72)</sup>	68.5 <sup>(10)</sup> , 72.2 <sup>(11)</sup> , 68.6 <sup>(70)</sup>	50.8, 81.6 <sup>(9)</sup> , 66.1 <sup>(56)</sup>	D <sup>(1,5,77)</sup>	a	Sgr B2  #
M 000.8+0.2	5.3	17436–2806	UCH II	—	3.5 <sup>(10)</sup> , 3.4 <sup>(68)</sup>	5.4 <sup>(9)</sup>	D <sup>(1,5)</sup>	a	
	5.3	17436–2807		—	—	—	D <sup>(1,5)</sup>	a	
M 001.1–0.1	123.7	17455–2805	UCH II	—	—	—	D <sup>(1)</sup>	a	
M 001.1–0.1	–17.5 $^{\ddagger}$	17455–2800	UCH II	–19.9 <sup>(72)</sup>	–15.2 <sup>(21)</sup> , –16.2 <sup>(73)</sup>	–15.6 <sup>(9)</sup> , –15 <sup>(38)</sup>	D <sup>(1,5)</sup>	a	Sgr D
M 001.3+0.1	–18.2			–12 <sup>(15)</sup>	—	–25 <sup>(15)</sup>	D <sup>(1,5,77)</sup>	b	
M 001.7–0.3	–28.0	17474–2738	PN	—	—	—	—	c	
M 002.5–0.0	–0.2	17484–2647		8.3 <sup>(49)</sup>	—	—	D <sup>(1)</sup>	a	
M 002.6+0.1	12.2	17480–2636	UCH II	—	3 <sup>(70)</sup>	12.0 <sup>(9)</sup>	D <sup>(1,5)</sup>	a	
	95.3			—	—	96.1 <sup>(9)</sup>	—	a	
M 002.9+0.0	–2.2 $^{\ddagger}$	17491–2625	UCH II	–2 <sup>(15)</sup> , –1.5 <sup>(48)</sup>	—	—	D <sup>(1,5,77)</sup>	a	
M 003.0–0.1	–15.8	17495–2624	UCH II	D <sup>(57)</sup>	—	–13, –12 <sup>(38)</sup>	—	a	
M 003.3–0.4	6.1 $^{\ddagger}$	17508–2633		—	—	—	D <sup>(5)</sup>	c	
M 003.3–0.1	6.1	17504–2609	PN	4.9 <sup>(48)</sup>	—	—	D <sup>(1,5)</sup>	a	
M 003.3–0.1	7.9 $^{\ddagger}$	17505–2605	UCH II	8.3 <sup>(48)</sup> , 8.0 <sup>(72)</sup>	—	9.5 <sup>(9)</sup>	D <sup>(1,5,77)</sup>	a	
M 003.4+0.9	1.0	17470–2533		—	—	—	—	c	
M 003.5–0.3	–30.2	17517–2609		—	—	–23 <sup>(9)</sup>	D <sup>(5,77)</sup>	b	
M 003.7–0.1	6.5 $^{\ddagger}$			3 <sup>(15)</sup> , 4.6 <sup>(48)</sup>	—	—	D <sup>(1,5)</sup>	a	
M 003.8+0.0	7.9 $^{\ddagger}$	17510–2543		—	—	—	D <sup>(5,77)</sup>	c	
M 003.9–0.0	16.5	17516–2532		—	17.5 <sup>(12)</sup> , 17 <sup>(17)</sup>	—	D <sup>(5,77)</sup>	a	
M 004.0+0.3	12.6			—	—	—	D <sup>(6,31)</sup>	c	SNR G3.8+0.3 <sup>§</sup>
M 004.4+0.1	8.1	17522–2504	UCH II	4.1 <sup>(48)</sup>	—	4.0 <sup>(9)</sup>	D <sup>(1,5)</sup>	a	
M 004.6–0.1	25.3	17535–2504		18 <sup>(15)</sup> , 23.3 <sup>(48)</sup>	—	—	D <sup>(1)</sup>	a	
M 005.0+0.2	10.6 $^{\ddagger}$	17531–2426	UCH II	12.0 <sup>(48)</sup>	—	—	D <sup>(1)</sup>	a	
M 005.3+0.1	12.1	17543–2419		11.8 <sup>(49)</sup>	—	—	D <sup>(1)</sup>	a	
	12.1	17546–2418		11.8 <sup>(49)</sup>	—	—	D <sup>(1)</sup>	a	
M 005.5–0.2	22.3	17559–2420	UCH II	21.4 <sup>(48)</sup> , 28.3 <sup>(72)</sup>	—	26.0 <sup>(9)</sup> , 21.8 <sup>(43)</sup>	D <sup>(1,5)</sup>	a	
M 005.7+0.3	7.5	17545–2357	UCH II	9.7 <sup>(59)</sup>	—	8.7 <sup>(2)</sup> , 9.1 <sup>(9)</sup>	D <sup>(1,5,77)</sup>	a	
M 005.8–0.1	6.4			—	—	—	—	c	
	11.9			—	—	—	—	c	HESS J1800–240C
M 005.9–0.4	8.4	17574–2403	UCH II	9.49 <sup>(2)</sup> , 10.1 <sup>(48)</sup> , 8.6 <sup>(72)</sup>	10 <sup>(17)</sup> , 9 <sup>(30)</sup> , 10.1 <sup>(69)</sup>	9.3 <sup>(9)</sup> , 9.8 <sup>(56)</sup>	D <sup>(1)</sup>	a	HESS J1800–240C
M 005.9+0.9	80.6	17524–2321		—	—	—	—	c	W 28 A2
M 006.0–0.1	9.9	18008–2421		3.9 <sup>(48)</sup>	10 <sup>(18)</sup>	—	D <sup>(34)</sup>	a	M 8
M 006.0–1.3	13.7	18013–2423		—	—	—	D <sup>(34)</sup>	c	
M 006.1–1.5	10.9	18018–2426		—	11.13 <sup>(4)</sup> , 11.2 <sup>(12)</sup>	11.0 <sup>(56)</sup>	D <sup>(34)</sup>	a	M 8 E
M 006.1–0.6	15.5	17588–2358		22.7 <sup>(48)</sup>	—	—	D <sup>(1)</sup>	b	HESS J1800–240A
M 006.2–0.6	17.9	17588–2356		20.3 <sup>(48)</sup>	—	—	D <sup>(1,77)</sup>	a	HESS J1800–240A
M 006.2–0.1	11.6 $^{\ddagger}$			14.5 <sup>(48)</sup>	—	—	D <sup>(1)</sup>	a	
M 006.3–1.1	14.4	18009–2407		—	—	—	—	c	
	14.4	18012–2407		—	—	—	—	c	
M 006.4–0.5	19.2	17588–2340	PN	19.0 <sup>(48)</sup> , 18.0 <sup>(49)</sup>	—	—	D <sup>(1)</sup>	a	W 28
M 006.6–0.1	15.1 $^{\ddagger}$	17577–2320		15.0 <sup>(48)</sup> , 13.2 <sup>(72)</sup>	13.2 <sup>(69)</sup> , 13 <sup>(70)</sup> , 12.47 <sup>(75)</sup>	14.8 <sup>(9)</sup>	D <sup>(1,5)</sup>	a	W 28
M 006.6–0.3	7.7	17585–2323	UCH II	—	7.24 <sup>(22)</sup> , 6.85 <sup>(75)</sup>	—	D <sup>(1)</sup>	a	W 28  #
	21.5			20.9 <sup>(48)</sup>	—	—	D <sup>(1)</sup>	a	
M 006.6–0.1	6.7			—	5.81 <sup>(22)</sup>	—	—	a	
M 007.0–0.3	18.3	17594–2303		13.8 <sup>(48)</sup>	16.1 <sup>(35)</sup>	—	D <sup>(1,5)</sup>	a	M 20#
M 007.1+0.2	17.7	17578–2246		15.3 <sup>(49)</sup>	—	—	D <sup>(1,5)</sup>	a	
M 007.2–0.5	19.3	18010–2259		—	—	—	—	a	
M 007.2+0.2	15.9 $^{\ddagger}$	17582–2234		—	—	—	D <sup>(1,5)</sup>	a	
M 007.3–0.1	22.2	17572–2234		17.9 <sup>(48)</sup>	—	—	D <sup>(1)</sup>	a	
M 007.3+0.7	28.6	17567–2215		22 <sup>(15)</sup> , 22.0 <sup>(48)</sup>	—	—	D <sup>(1)</sup>	b	
M 007.5+0.1	–20.4	17591–2228	UCH II	–17.8 <sup>(48)</sup> , –16.0 <sup>(72)</sup>	—	–13.9 <sup>(9)</sup>	—	a	
	14.0			—	—	15.4 <sup>(9)</sup>	—	a	
M 007.6–0.1	13.9	18002–2218		—	—	—	—	c	

**Table 1.** (Continued)

CO cloud	$V_{\text{LSR}}$ (km s $^{-1}$ )	IRAS	Criteria	Radio recombination (km s $^{-1}$ )	Maser line (km s $^{-1}$ )	Molecular line (km s $^{-1}$ )	Radio source	Rank $^{\dagger}$	Remarks
M 007.7–0.7	30.8	18024–2231	—	—	—	—	D $^{(1)}$	c	
M 008.0–0.3	40.9	18016–2209	—	—	—	—	—	c	
M 008.0–0.1	40.0	18011–2206	42.6 $^{(48)}$	—	—	—	D $^{(1)}$	a	
M 008.1–0.0	41.6	18009–2155	UCH II	—	—	—	D $^{(5,52)}$	a	W 30
M 008.2+0.2	19.0	17599–2148	UCH II	20.6 $^{(48)}$ , 22.1 $^{(72)}$	19 $^{(53)}$ , 20.0 $^{(69,70)}$	18.6 $^{(56)}$	D $^{(1,5,52)}$	a	
M 008.3–0.1	49.2	18016–2148	—	46.8 $^{(48)}$	—	—	D $^{(1,5,52)}$	a	
	49.2	18015–2146	—	46.8 $^{(48)}$	—	—	D $^{(1,5,52)}$	a	
M 008.4–0.3	38.1	18026–2153	UCH II	—	—	36.7 $^{(9)}$	D $^{(1,5,52)}$	a	W 30 $^{\#}$
M 008.6–0.3	35.8	18032–2137	UCH II	41.9 $^{(48)}$ , 42.7 $^{(72)}$	44.1 $^{(16)}$ , 35.3 $^{(21)}$ , 42.8 $^{(69)}$	33.5 $^{(9)}$ , 36 $^{(56)}$	D $^{(1,5,52)}$	a	W 30 $^{\#}$
M 008.7+0.7	23.3	17595–2108	—	—	—	—	—	c	
M 008.8+0.7	22.6	17597–2101	—	—	—	—	—	c	
M 008.9–0.3	38.5	18035–2126	UCH II	31.0 $^{(48)}$	—	40.2 $^{(9)}$	D $^{(1,5,52)}$	a	
M 009.0–0.2	26.0	18035–2114	—	—	—	—	—	c	
M 009.1–0.7	23.2	18052–2125	—	—	—	—	D $^{(1,77)}$	c	
M 009.1–0.4	40.0	18043–2116	—	—	—	—	—	c	
M 009.6+0.2	3.2	18032–2032	UCH II	4.1 $^{(48)}$	5.5 $^{(12)}$ , 1.1 $^{(69)}$ , 1 $^{(70)}$	5.0 $^{(9)}$ , 4.4 $^{(37)}$ , 4.3 $^{(56)}$	D $^{(1)}$	a	
M 009.7–0.1	55.0	18045–2033	—	—	—	—	D $^{(1,8)}$	c	SNR G9.7–0.0 $^{\$}$
M 009.9–0.7	27.8	18073–2046	UCH II	—	—	28.0 $^{(9)}$	D $^{(1,8)}$	a	SNR G9.9–0.8 $^{\$}$
M 010.1–0.3	16.4	18064–2020	UCH II, PN	14.2 $^{(48)}$ , 12.5 $^{(72)}$	—	12.8 $^{(9)}$	D $^{(1,5)}$	a	W 31
M 010.3–0.1	13.2	18060–2005	UCH II	12.6 $^{(2)}$ , 11.0 $^{(48)}$	9.9 $^{(69)}$ , 11 $^{(70)}$	13.1 $^{(9)}$	D $^{(1,5)}$	a	W 31
M 010.3+0.1	66.0	18052–1958	—	—	—	—	—	c	
M 010.5+0.0	68.2	18056–1952	UCH II	70.2 $^{(2)}$ , 70.1 $^{(48)}$	73.4 $^{(64)}$ , 61.7 $^{(67)}$ , 74.8 $^{(69)}$	68.9 $^{(9)}$ , 66.7 $^{(37)}$ , 67.1 $^{(56)}$	D $^{(1,5)}$	a	
M 010.6–0.3	-3.2	18075–1956	—	0.4 $^{(48)}$ , 0.3 $^{(72)}$	-2 $^{(12)}$ , -8.0 $^{(36)}$ , 4.6 $^{(69)}$	-2.9 $^{(37)}$ , -2.2 $^{(56)}$	D $^{(1,5)}$	a	W 31
M 010.7–0.1	52.9	18063–1943	—	—	—	—	—	c	
M 010.9+0.0	20.2	18067–1927	UCH II	18.5 $^{(48)}$ , 16.3 $^{(59)}$	23.9 $^{(64)}$ , 24.4 $^{(69)}$	20.6 $^{(9)}$	D $^{(1,5)}$	a	
M 011.1–0.4	-0.1	18085–1931	UCH II	—	—	-1.1 $^{(9)}$	D $^{(1,5)}$	a	SNR G11.2–0.3 $^{\$}\#$
	-0.1	18085–1933	—	—	—	—	D $^{(1,5)}$	c	
M 011.1+0.1	12.7	18068–1917A	—	7.3 $^{(48)}$	—	—	D $^{(1)}$	b	
M 011.2–1.0	30.6	—	—	—	—	—	D $^{(8)}$	c	SNR G11.1–1.0 $^{\$}$
M 011.5–1.5	10.3	18134–1942	UCH II	—	7.5 $^{(53)}$ , 6.7 $^{(69)}$	10.6 $^{(9)}$	—	a	
M 011.5+0.1	52.7	18076–1853	PN	—	—	—	D $^{(77)}$	c	
M 011.9+0.7	23.2	18060–1816	UCH II	25.1 $^{(48)}$	—	—	D $^{(1)}$	a	
M 011.9–0.6	36.4	18110–1854	UCH II	39.3 $^{(48)}$	38.5 $^{(67)}$ , 32.0 $^{(69)}$	38.4 $^{(9)}$ , 37.8 $^{(37)}$	D $^{(1,77)}$	a	
M 011.9–0.1	41.4	18094–1840	UCH II	—	40.5 $^{(12)}$ , 43.0 $^{(13)}$ , 42.6 $^{(69)}$	—	D $^{(1)}$	a	AX J1812.2–1842
M 012.0–0.2	57.9	18099–1841	—	—	60.2 $^{(53)}$	—	—	a	

\* Column (1): CO cloud name in  $l$  and  $b$ . Column (2): peak  $V_{\text{LSR}}$  of  $^{12}\text{CO}$  determined by a Gaussian fitting. Column (3): IRAS source name. Column (4): criteria of the IRAS source, ultra compact H II region (UCH II) or planetary nebula (PN). Column (5): peak  $V_{\text{LSR}}$  of the radio recombination line sources. Column (6):  $V_{\text{LSR}}$  of maser line sources. Column (7): peak  $V_{\text{LSR}}$  of other molecular line sources. Column (8): radio continuum sources. “D” stands for detected. Column (9): rank. Column (10): additional remarks.

$\dagger$  We classified molecular clouds according to the following criteria. Rank a: molecular clouds associated with objects having velocity information whose detection lies within 5 km s $^{-1}$  of CO peak velocity. Rank b: molecular clouds with associated objects whose velocity is separated by more than 5 km s $^{-1}$  from CO peak velocity. Rank c: molecular clouds with associated objects that are coincident in position only without velocity information.

$\ddagger$  The value is determined by  $^{13}\text{CO}$  spectrum.

$\S$  SNRs are from the Green SNR catalog (Green 2004).

$\parallel$  Object associated with TeV  $\gamma$ -ray source (e.g., Aharonian et al. 2008).

$\#$  Object associated with X-ray source.

#### Reference of table 1.

- 1 4.87 GHz radio continuum using Effelsberg 100-m telescope (Altenhoff et al. 1978).
- 2 4.87 GHz H110 $\alpha$ , H<sub>2</sub>CO absorption line using Green Bank Telescope (Araya et al. 2007).
- 3 110–147 GHz CH<sub>3</sub>CN using 15-m SEST (Araya et al. 2005).
- 4 1665 MHz, 1667 MHz OH maser and 8.4 GHz radio continuum using VLA (Argon et al. 2000).
- 5 1.4 GHz, 5 GHz radio continuum using VLA (Becker et al. 1994).
- 6 327 MHz radio continuum using GMRT (Bhatnagar 2002).
- 7 22.2 GHz H<sub>2</sub>O ( $6_{16}$ – $5_{23}$ ) using Medicina 32-m telescope (Brand et al. 1994).
- 8 330 MHz radio continuum using VLA (Brogan et al. 2006).
- 9 98 GHz CS (2–1) using 15-m SEST and 20-m OSO (Bronfman et al. 1996).
- 10 6.67 GHz methanol maser using ATCA (Caswell 1996).
- 11 6.67 GHz methanol maser using ATCA (Caswell 1997).
- 12 1665 MHz and 1667 MHz OH maser using ATCA (Caswell 1998).
- 13 13441 MHz OH maser using Parkes 64-m telescope (Caswell 2004).
- 14 1612 MHz OH maser using Parkes 64-m telescope (Caswell et al. 1981).
- 15 5 GHz H109 $\alpha$ , 4.9 GHz H110 $\alpha$ , 4.8 GHz H<sub>2</sub>CO using Parkes 64-m telescope (Caswell & Haynes 1987).
- 16 12 GHz methanol maser using Parkes 64-m telescope (Caswell et al. 1993).
- 17 6.67 GHz methanol using Parkes 64-m telescope (Caswell et al. 1995).
- 18 4.7 GHz OH maser using Parkes 64-m telescope (Cohen et al. 1995).
- 19 IRAS point source to classify YSO (Chan et al. 1996).
- 20 2.4 GHz and 1.4 GHz radio source (for Wolf–Rayet star) using ATCA (Chapman et al. 1999).
- 21 22.2 GHz H<sub>2</sub>O ( $6_{16}$ – $5_{12}$ ) using Max-Plank 100-m telescope (Churchwell et al. 1990).
- 22 1720 MHz OH maser using VLA (Claussen et al. 1997).
- 23 8.3 GHz H92 $\alpha$  using VLA (Cram et al. 1996).
- 24 23 GHz H52 $\alpha$  and H66 $\alpha$  using VLA (De Pree et al. 1996).
- 25 5 GHz H109 $\alpha$  using CSIRO 64-m and 42-m Green Band telescope (Dickel & Milne 1972).
- 26 112 GHz C<sup>17</sup>O (1–0) using 15-m SEST (Fontani et al. 2005).
- 27 1720 MHz OH maser using 43-m Green Bank telescope, 64-m Parkes telescope, VLA, and ATCA (Frail et al. 1996).

- 28 330 MHz, 1.4 GHz radio continuum using VLA (Frail et al. 1994b).  
 29 14.5 GHz H<sub>2</sub>CO (2<sub>11</sub>–2<sub>12</sub>) and 4.8 GHz H<sub>2</sub>CO (1<sub>10</sub>–1<sub>11</sub>) using Parks 64-m telescope (Gardner & Whiteoak 1984).  
 30 203.4 GHz H<sub>2</sub>O (3<sub>13</sub>–2<sub>20</sub>) using 30-m IRAM (Gensheimer et al. 1996).  
 31 843 MHz radio continuum using MOST (Gray 1994).  
 32 Radio source of SNR catalog (Green 2004).  
 33 1612 MHz OH line emission (OH/IR stars) using 100-m Effelsberg telescope and VLA (Habing et al. 1983).  
 34 10 GHz radio continuum using 45-m Nobeyama telescope (Handa et al. 1987).  
 35 22.2 GHz H<sub>2</sub>O (6<sub>16</sub>–5<sub>23</sub>) using VLA (Healy et al. 2004).  
 36 22.2 GHz H<sub>2</sub>O (6<sub>16</sub>–5<sub>23</sub>) using VLA (Hofner & Churchwell 1996).  
 37 112 GHz C<sup>17</sup>O (1–0) and 224 GHz C<sup>17</sup>O (2–1) using 30-m IRAM (Hofner et al. 2000).  
 38 110 GHz C<sup>18</sup>O (2–1) and 86 GHz SiO (2–1) using 15-m SEST (Hüttemeister et al. 1998).  
 39 NH<sub>3</sub> using NRAO 43-m telescope and 100-m telescope of the MPIfR (Hüttemeister et al. 1993).  
 40 330 MHz, 1.4 GHz, 5 GHz radio continuum using VLA (Kassim et al. 1991).  
 41 86.1–92.1 GHz (5 molecular emission lines) using 22-m Mopra telescope (Kim et al. 2002).  
 42 14.7 GHz H76α using VLA (Kim & Koo 2001).  
 43 21 cm line H I using VLA and 110 GHz <sup>13</sup>CO ( $J = 1$ –0) using 14-m telescope of Taeduk Radio Astronomy Observatory (Koo et al. 1996).  
 44 4.85 GHz radio continuum using published catalog (Kuchar & Clark 1997).  
 45 22.2 GHz H<sub>2</sub>O (6<sub>15</sub>–5<sub>12</sub>) using 100-m Effelsberg telescope (Kurtz & Hofner 2005).  
 46 330 MHz radio continuum using VLA (LaRosa et al. 2000).  
 47 1616.4 MHz radio continuum and H70α using VLA and 43-m Green Bank telescope (Liszt 1992).  
 48 10 GHz H85α, H87α, and H88α using 43-m Green Bank telescope (Lockman 1989).  
 49 5 GHz H109α, H111α, and 3.3 GHz H126α, H127α using 43-m Green Bank telescope (Lockman et al. 1996).  
 50 4.8 GHz and 8.6 GHz radio continuum using ATCA (Martín-Hernández et al. 2003).  
 51 86 GHz SiO (2–1), 128 GHz SiO (3–2) using 15-m SEST (Miettinen et al. 2006).
- 52 4.85 GHz radio continuum using VLA (Ojeda-May et al. 2002).  
 53 6.67 GHz methanol maser using last 6.67 GHz methanol catalog (Pestalozzi et al. 2005).  
 54 93.2 GHz N<sub>2</sub>H<sup>+</sup> (1–0) using 20-m OSO telescope and 15-m SEST (Pirogov et al. 2003).  
 55 4.87 GHz H110α and H138β using 100-m Effelsberg telescope (Planesas et al. 1991).  
 56 343 GHz CS (7–6) using 10.4-m Caltech Submillimeter telescope (Plume et al. 1992).  
 57 14.7 GHz H35α, H39α, and H41α using IRAM 30-m (Rodríguez-Fernández & Martín-Pintado 2005).  
 58 115 GHz CO (1–0) and 230 GHz CO (2–1) using 15-m SEST (Russeil & Castets 2004).  
 59 8.3 GHz H92α using VLA (Sewilo et al. 2004).  
 60 230 GHz CO (2–1) using NRAO 12-m telescope (Shaver et al. 1985b).  
 61 1.4 GHz radio continuum using VLA (Shaver et al. 1985a).  
 62 6.67 GHz methanol maser using 32-m Medicina radio telescope (Slysh et al. 1999).  
 63 4.79 GHz, 5.84 GHz radio continuum using ATCA (Stewart et al. 1994).  
 64 6.67 GHz methanol using 32-m Torun telescope (Szymczak et al. 2000).  
 65 22.2 GHz H<sub>2</sub>O maser using VLA (Taylor et al. 1993).  
 66 1612 MHz OH maser using published catalog (te Lintel Hekkert et al. 1989).  
 67 95 GHz methanol (8<sub>0</sub>–7<sub>1</sub> A<sup>+</sup>) maser using 22-m Mopra telescope (Val'tts et al. 2000).  
 68 6.67 GHz methanol maser using 26-m telescope at Hartebeesthoek (van der Walt et al. 1996).  
 69 6.67 GHz methanol maser using Parkes 64-m telescope (Walsh et al. 1998).  
 70 6.67 GHz methanol maser using ATCA (Walsh et al. 1997).  
 71 843 MHz radio continuum using MOST (Whiteoak & Green 1996).  
 72 14.7 GHz H76α using MPIfR 100-m telescope (Wink et al. 1983).  
 73 1720 MHz OH maser using VLA (Yusef-Zadeh et al. 1999).  
 74 1720 MHz OH maser using VLA (Yusef-Zadeh et al. 1995).  
 75 1720 MHz OH maser using VLA (Yusef-Zadeh et al. 2003).  
 76 220 GHz C<sup>18</sup>O (2–1) using 15-m SEST (Zinchenko et al. 2000).  
 77 5 GHz and 1.4 GHz radio continuum using VLA (Zoonematkermani et al. 1990).

sources, as seen for instance in M 011.5+0.1(see table 1). However, H II regions are also sources of thermal radio continuum, and it is difficult to distinguish between them and PNe.

Pottasch et al. (1988) compared the color flux density ratios of IRAS sources known to be PNe, H II regions, and external galaxies. They found that the largest differences occur for the  $F_{12}/F_{25}$  and  $F_{25}/F_{60}$  colors for all sources. As a result of their comparisons, they derived the following color criteria for PNe:

$$\log(F_{12}/F_{25}) \leq -0.52 \text{ and } \log(F_{25}/F_{60}) \geq -0.46. \quad (2)$$

Using this to classify our IRAS point sources associated with CO clouds, we identified 6 IRAS point sources that satisfy the criteria, and which are therefore probably PNe (figure 3).

### 3.1.3. IRAS detection limit

A large number of IRAS point sources are not detected in one or more of the IRAS bands. Such non-detections are given as upper limits in the catalog. In order to be able to apply the criteria of Wood and Churchwell,  $\log(F_{25}/F_{12}) \geq 0.57$ ,  $\log(F_{60}/F_{12}) \geq 1.30$ , we must introduce the following criteria in our selection of IRAS point sources: (1) If emission is not detected in either of the 25 μm or 60 μm bands, we exclude the IRAS point source, since using an upper limit in place of an absolute value may result in the point source being incorrectly

identified as an UCH II region. (2) If the source is detected at both 25 μm and 60 μm, but not at 12 μm, we include it, since using an upper limit for 12 μm emission can only act to shift a point source away from the UCH II region (see figure 3), and will never result in a false positive. (3) If both 25 μm and 12 μm or both 60 μm and 12 μm are given as upper limits, we exclude the source, since no absolute values exist. We exclude sources in the same way when applying the Pottasch et al.'s color criteria.

### 3.2. Radio Recombination Line Sources

Radio recombination lines are detected from H II regions and PNe. We employed radio recombination line sources observed at 2 cm in the H76α (Wink et al. 1983), at 3 cm in the H85α, H87α, and H88α (Lockman 1989), at 6 cm in the H109α and H111α (Caswell & Haynes 1987; Lockman et al. 1996), and at 9 cm in the H126α and H127α (Lockman et al. 1996). These previous studies provide a complete coverage of the present area.

### 3.3. Maser Sources

Masers are formed in shocked layers of warm molecular gas at the interfaces between the ionized gas of the UCH II regions and their surrounding molecular clouds. In particular,

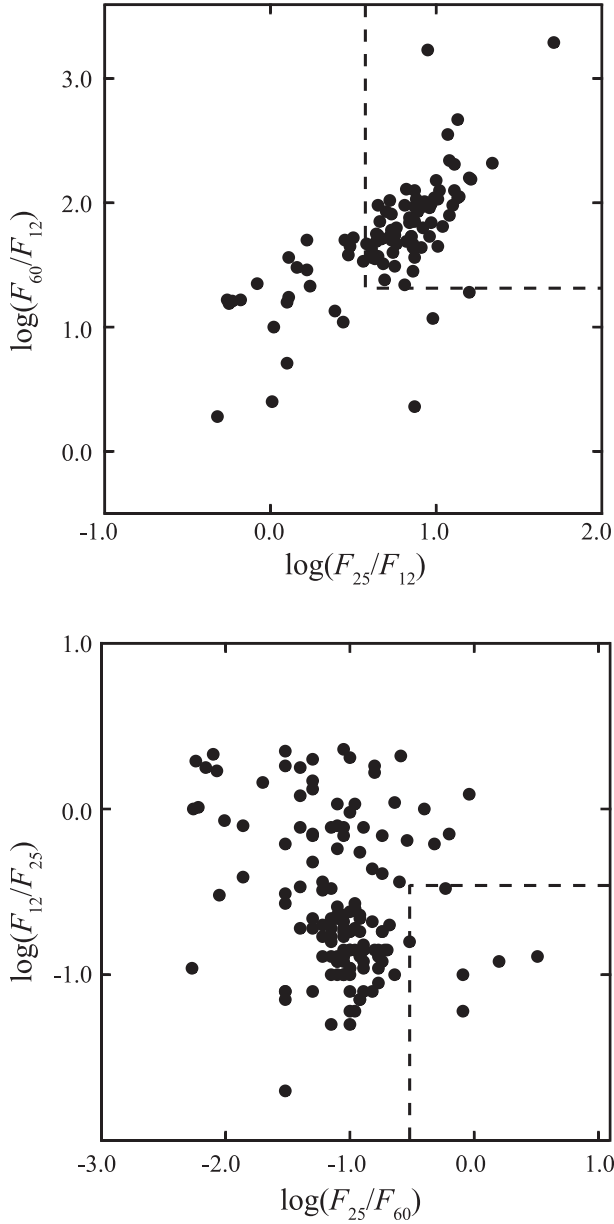


**Fig. 3.** Color-color diagrams of IRAS point sources associated with CO molecular clouds. Upper panel: the flux density ratios,  $F(60 \mu\text{m})/F(12 \mu\text{m})$  and  $F(25 \mu\text{m})/F(12 \mu\text{m})$ , are plotted. The dashed lines show the boundary of the region that satisfies the Wood and Churchwell's (1989) criteria for UCH II regions [ $\log(F_{25}/F_{12}) \geq 0.57$  and  $\log(F_{60}/F_{12}) \geq 1.30$ ]. Lower panel: the flux density ratios,  $F(12 \mu\text{m})/F(25 \mu\text{m})$  and  $F(25 \mu\text{m})/F(60 \mu\text{m})$ , are plotted. The dashed lines show the boundary of the region that satisfies the Pottasch et al.'s (1988) criteria for planetary nebulae [ $\log(F_{12}/F_{25}) \leq -0.52$  and  $\log(F_{25}/F_{60}) \geq -0.46$ ].

6.67 GHz methanol masers and 1665, 1667 MHz OH masers are known as tracers of compact H II regions in high-mass star-forming regions (Walsh et al. 1997, 1998; Koralesky et al. 1998; Slysh et al. 1999; Argon et al. 2000). In many studies, IRAS point sources that satisfy the color criteria of high-mass star-forming regions were selected, and 6.67 GHz observations were carried out toward them (Walsh et al. 1997, 1998; Slysh et al. 1999; Szymczak et al. 2000). In this way Walsh et al.

(1997) identified 215 UCH II regions associated with 6.67 GHz methanol masers. It is known that 1720 MHz OH masers are associated with SNRs interacting with molecular clouds (Frail et al. 1994a, 1996; Claussen et al. 1997; Wardle & Yusef-Zadeh 2002; Yusef-Zadeh et al. 2003). W 28, W 44, and IC 433 are prototypes for SNRs interacting with molecular clouds (Frail et al. 1996; Koralesky et al. 1998). Indeed, 41 1720 MHz OH maser line spots were detected at some positions in W 28 (Claussen et al. 1997), concentrated in a localized region of the SNR. We chose the objects in the present area from these previous studies.

### 3.4. Other Molecular Lines

We used the molecular data of CS ( $J = 2-1$ ) (Bronfman et al. 1996), CS ( $J = 7-6$ ) (Plume et al. 1992), and NH<sub>3</sub> (Hüttemeister et al. 1993), which generally cover several square degrees of the Galactic center region, or toward selected IRAS/maser sources. We used these observation data covering the present area, although these were not complete in coverage.

### 3.5. Radio Continuum Sources

Radio continuum emission from the Galactic plane is mainly divided into two types: synchrotron emission radiated by the interaction between relativistic electrons and the Galactic magnetic field, and thermal emission arising from the H II regions. We have used the sources observed at 1.4–5 GHz from Altenhoff et al. (1978), Zoonematkermani et al. (1990), and Becker et al. (1994). These previous studies provide almost complete coverage of the present area.

## 4. Comparison between the CO Emission and the Astronomical Objects

### 4.1. Velocity Channel Maps of the CO Emission

The <sup>12</sup>CO data were divided into 6 regions, each covering 4° in galactic longitude. These are generally subdivided into 5 km s<sup>-1</sup> velocity intervals, where the interval is chosen so as not to miss a significant spatial change of the CO emission. For extreme high and low velocities, we chose broader velocity intervals. These CO channel maps are shown in the 150 panels of figure 4, where only IRAS point sources are indicated by crosses. We picked up objects that lie within 2' in space and 10 km s<sup>-1</sup> of a localized <sup>12</sup>CO peak in each panel. We also employed optically thin <sup>13</sup>CO emission when the <sup>12</sup>CO peak was not clearly identified within the <sup>13</sup>CO coverage.

As a result, we found that 169 positions of the CO emission in total are associated with some of these objects. We list them in table 1 along with data of the associated objects. Thus-identified molecular peaks were classified into the three ranks according to the degree in the velocity coincidence:

“Rank a” = associated objects whose peak velocity agrees within 5 km s<sup>-1</sup> of a CO peak velocity, “rank b” = objects whose peak velocity differs by more than 5 km s<sup>-1</sup> from the CO peak velocity, where we note that the typical velocity dispersion among CO clouds in the Galaxy is 10 km s<sup>-1</sup> (Stark 1984), and “rank c” = objects without velocity information.

We found 107 CO positions as “rank a”, 7 as “rank b”, and 53 as “rank c”.

We examined the difference between the central velocities

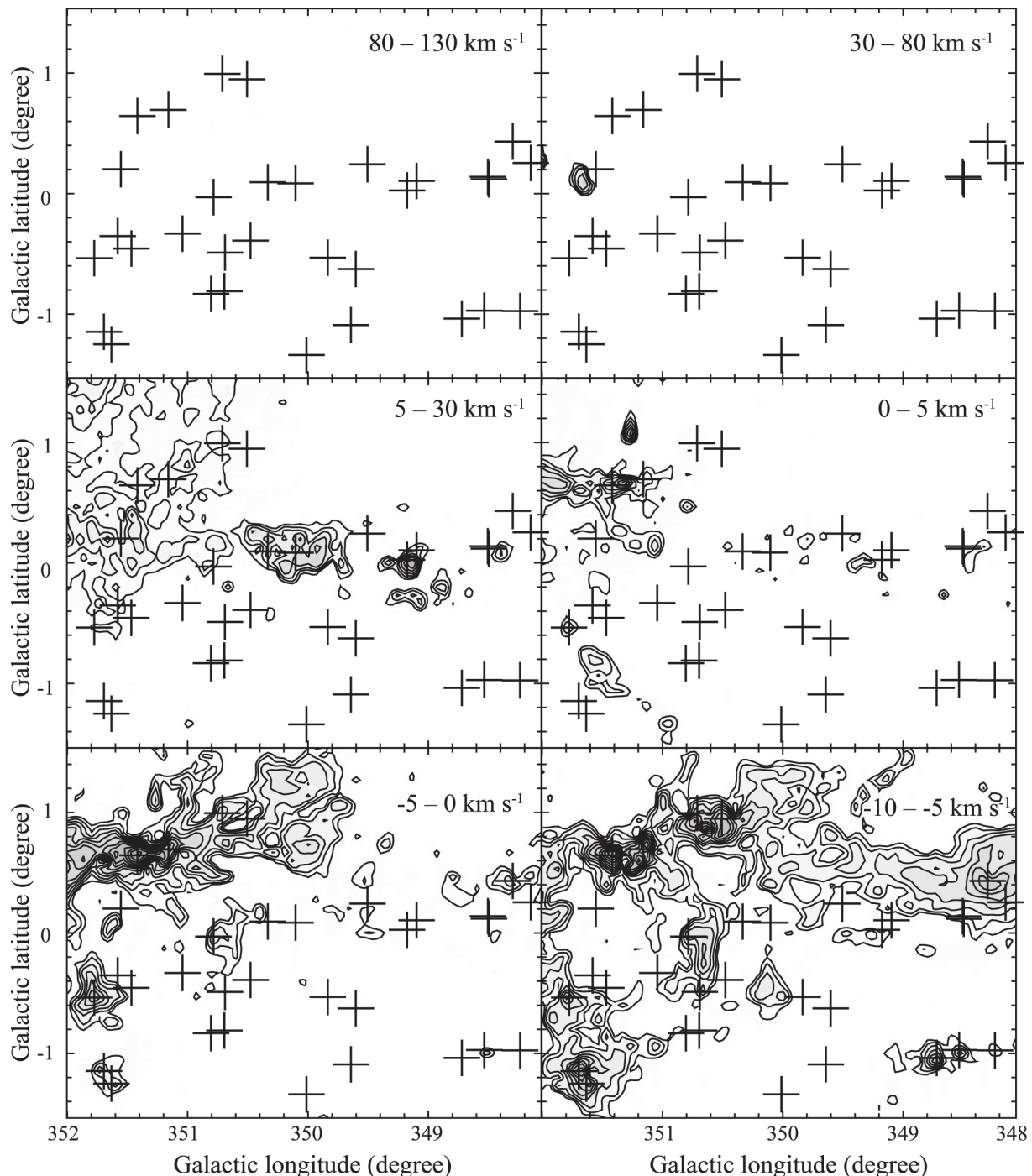


**Fig. 4.** (a) Velocity channel maps of  $^{12}\text{CO}$  ( $J = 1-0$ ) line emission in  $l = 348^\circ - 352^\circ$ . The integrated velocity range is given at the top right in each panel. The contours are 10, 16, 24, 37, 58, 89, 138, 214, 332, 515, and 800  $\text{K km s}^{-1}$  for a velocity range of 25 or 50  $\text{km s}^{-1}$ . The contours are 10, 15, 22, 31, 41, 53, 67, 84, 103, 125, 148, 173, and 201  $\text{K km s}^{-1}$  for a velocity range of 5  $\text{km s}^{-1}$ . The gray-scale flux range is 0–800  $\text{K km s}^{-1}$ . Crosses represent associated IRAS point sources in table 2.

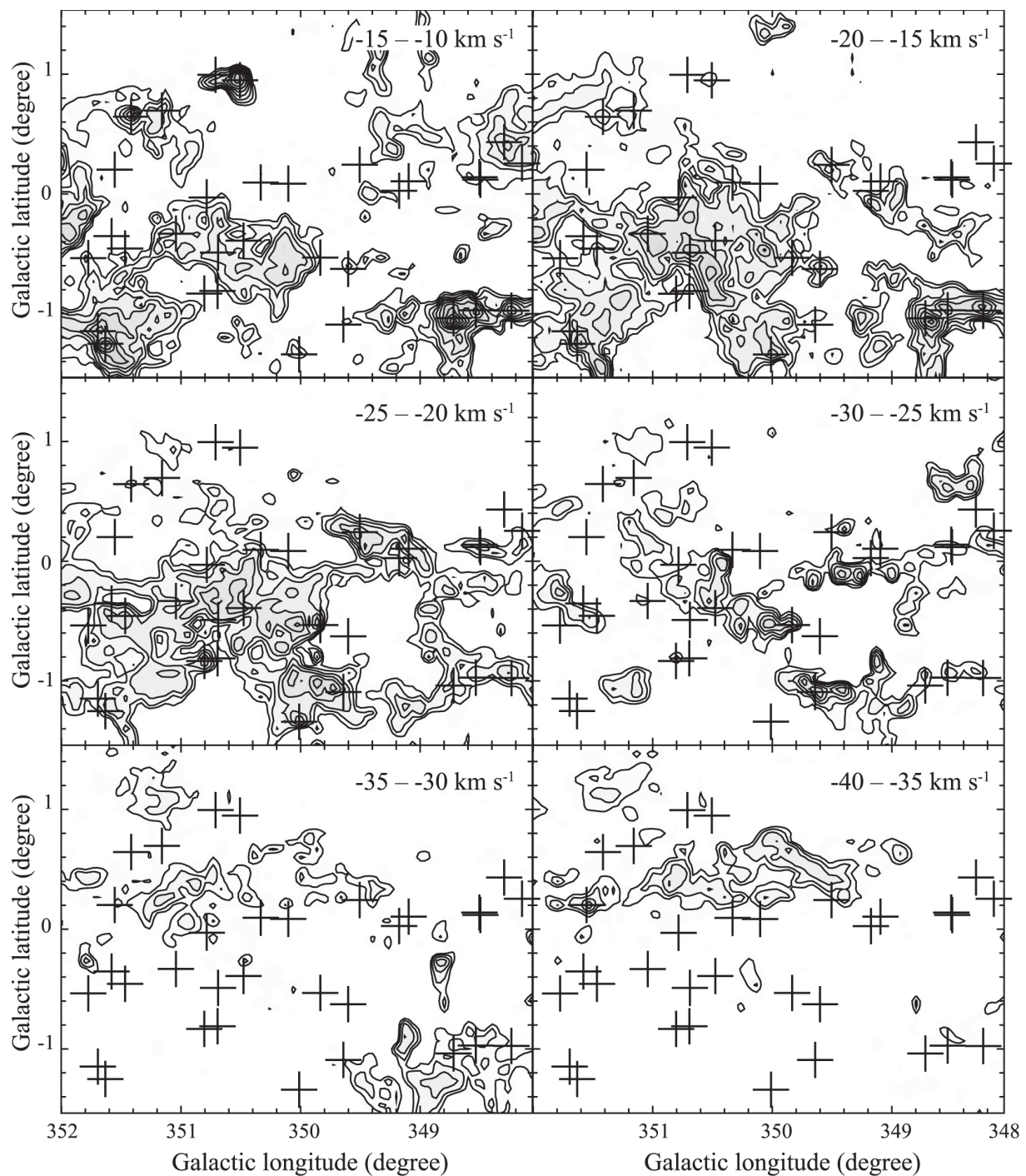
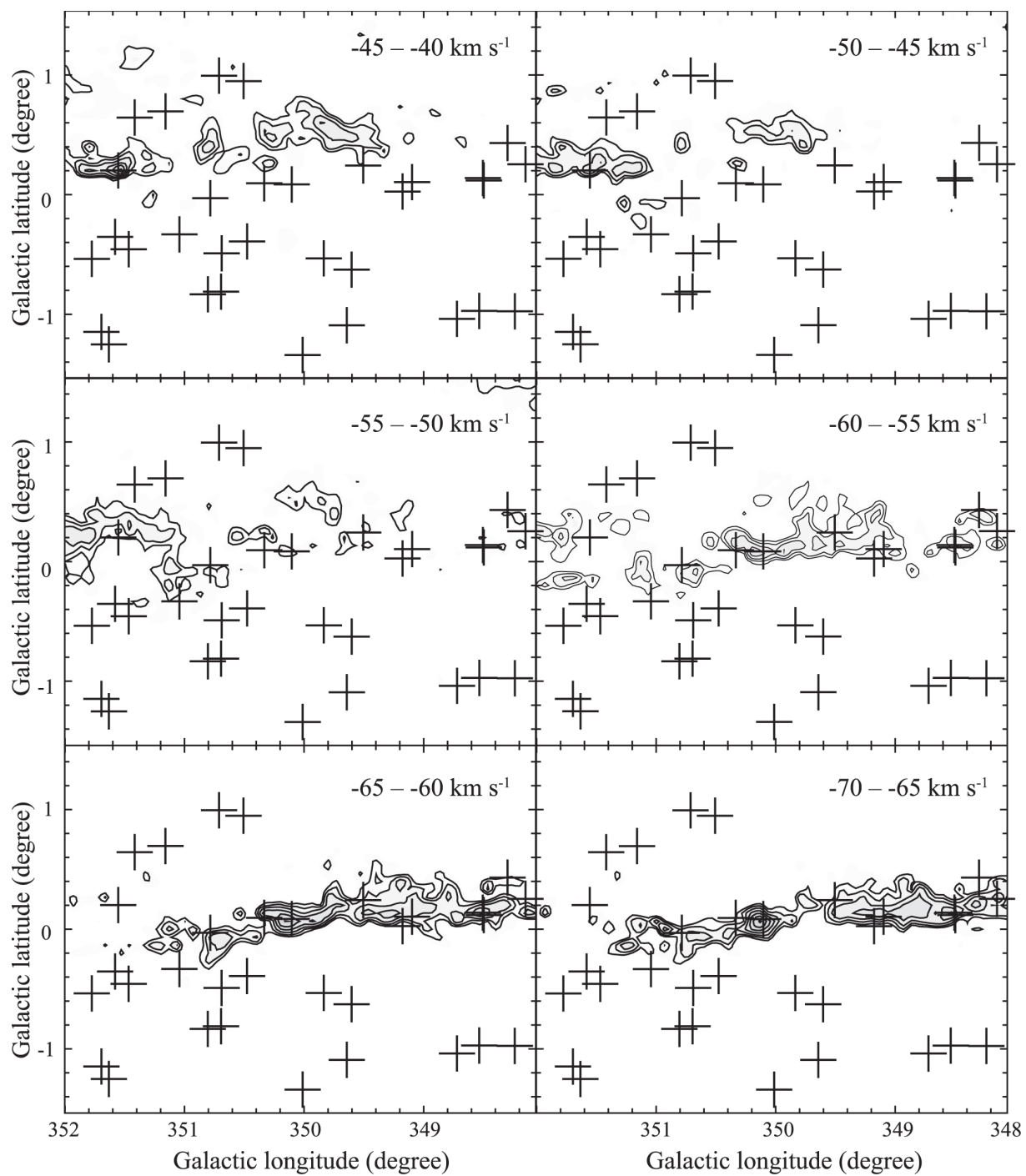


Fig. 4. (a) (Continued)

**Fig. 4.** (a) (Continued)

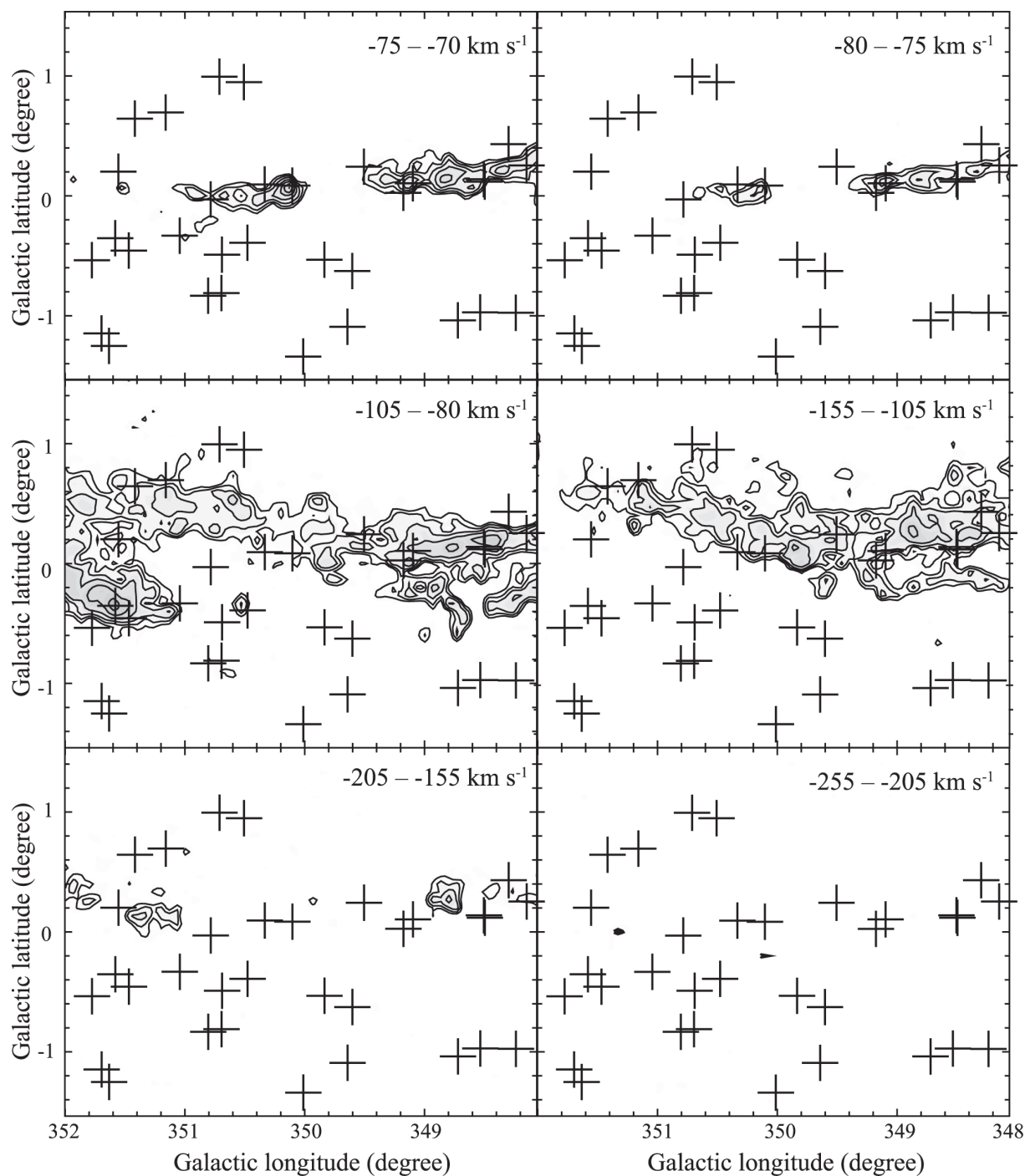
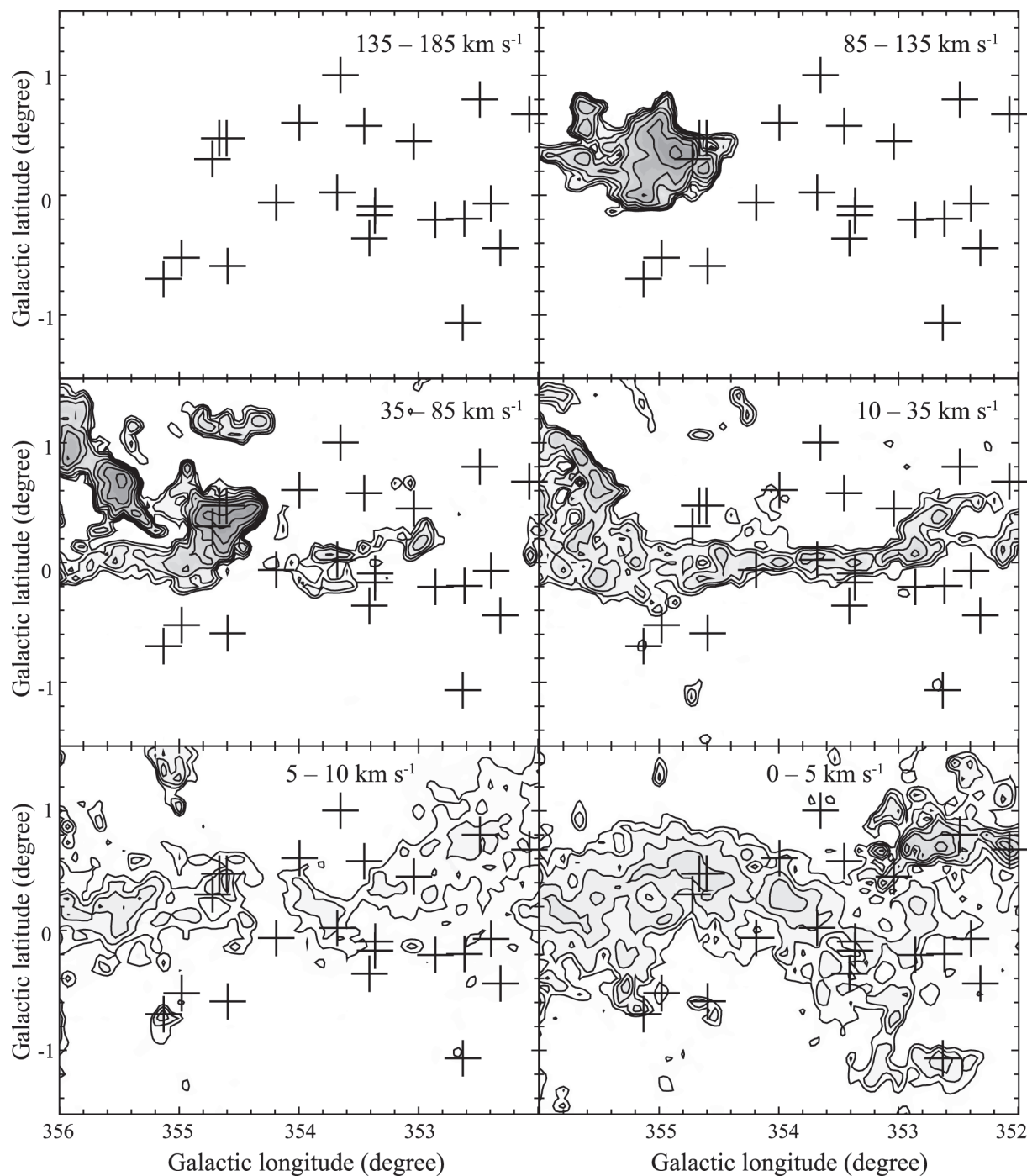


Fig. 4. (a) (Continued)



**Fig. 4.** (b) Same as figure 4(a) but in  $l = 352^\circ$ – $356^\circ$ .

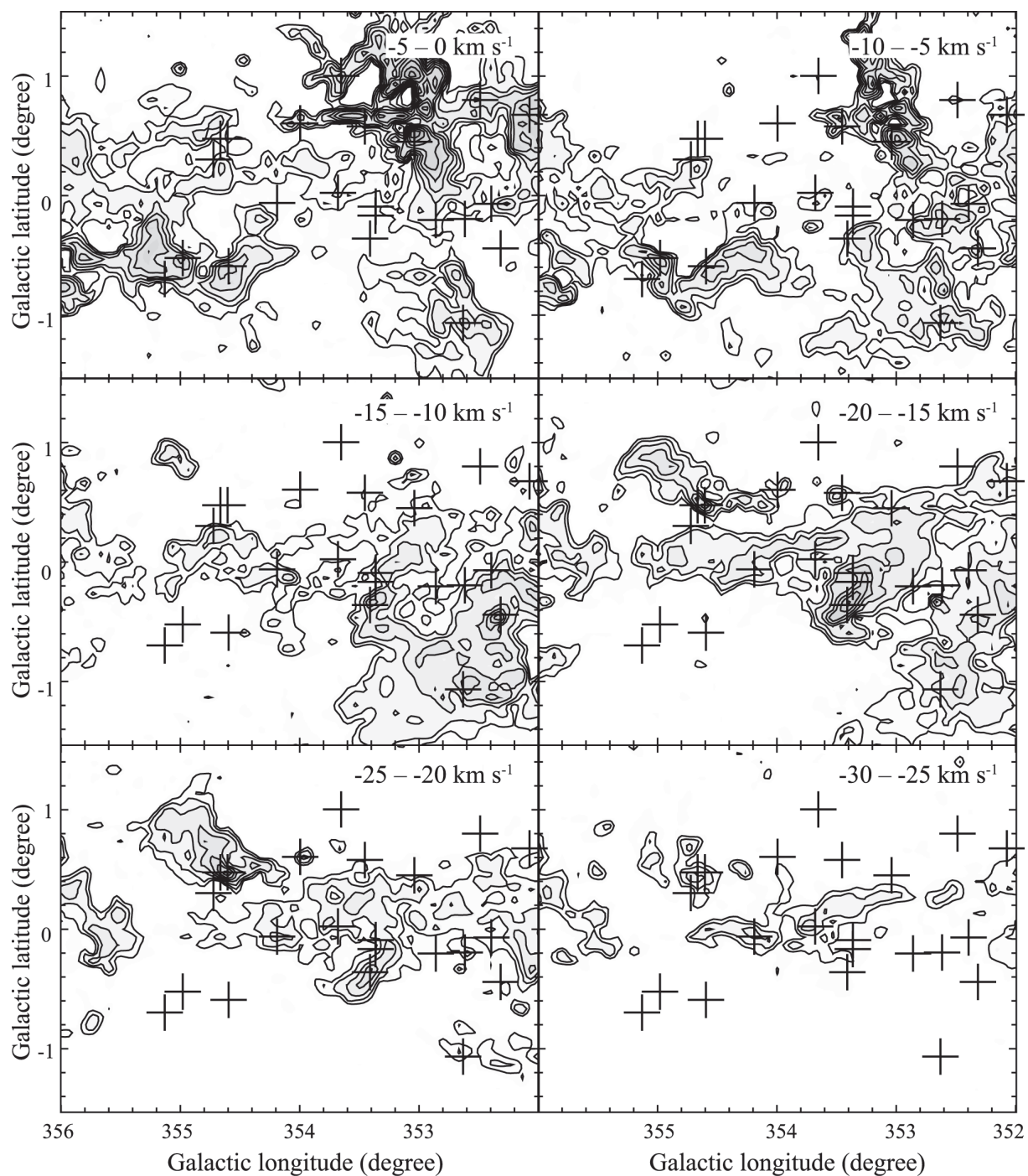


Fig. 4. (b) (Continued)

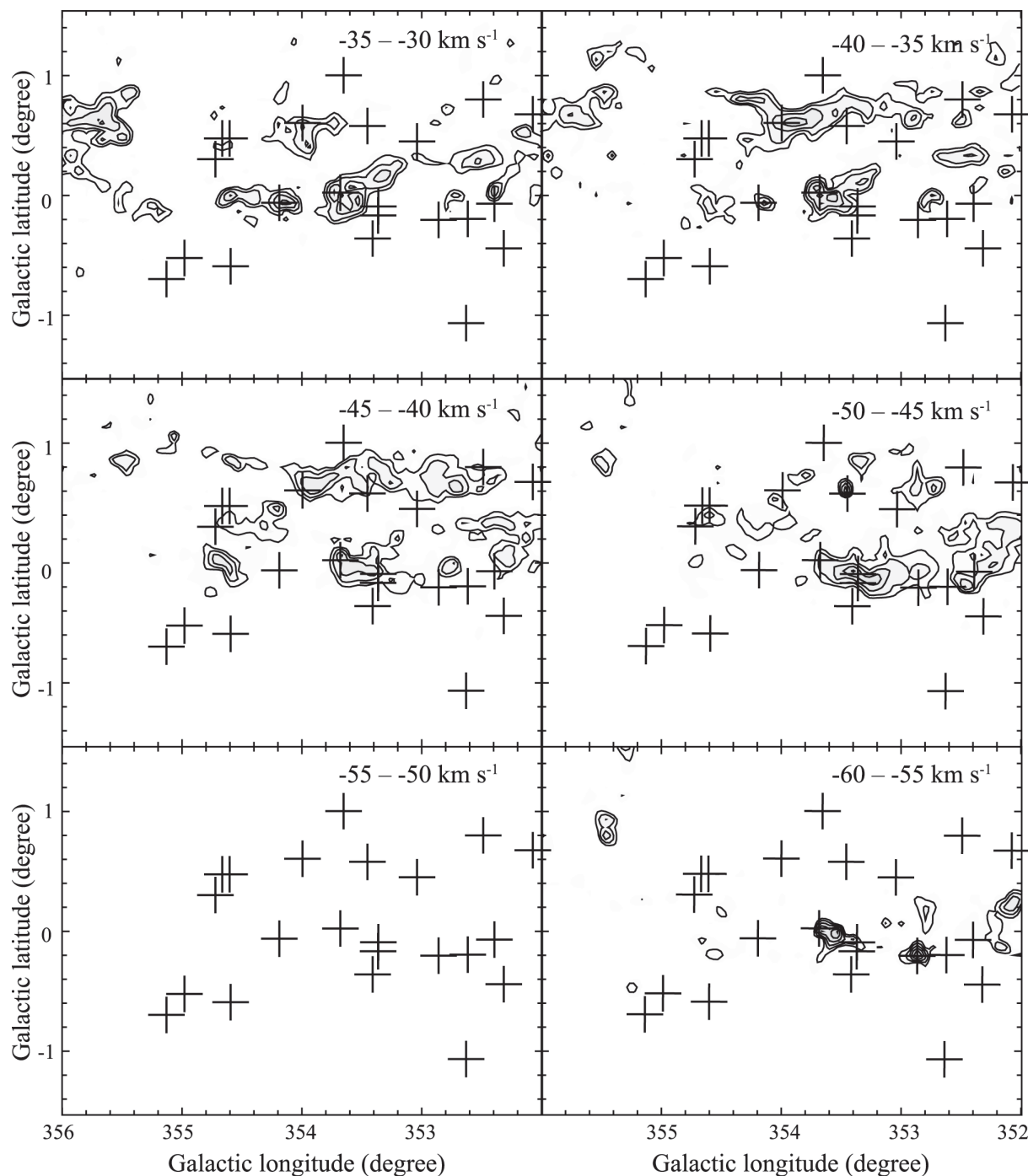


Fig. 4. (b) (Continued)

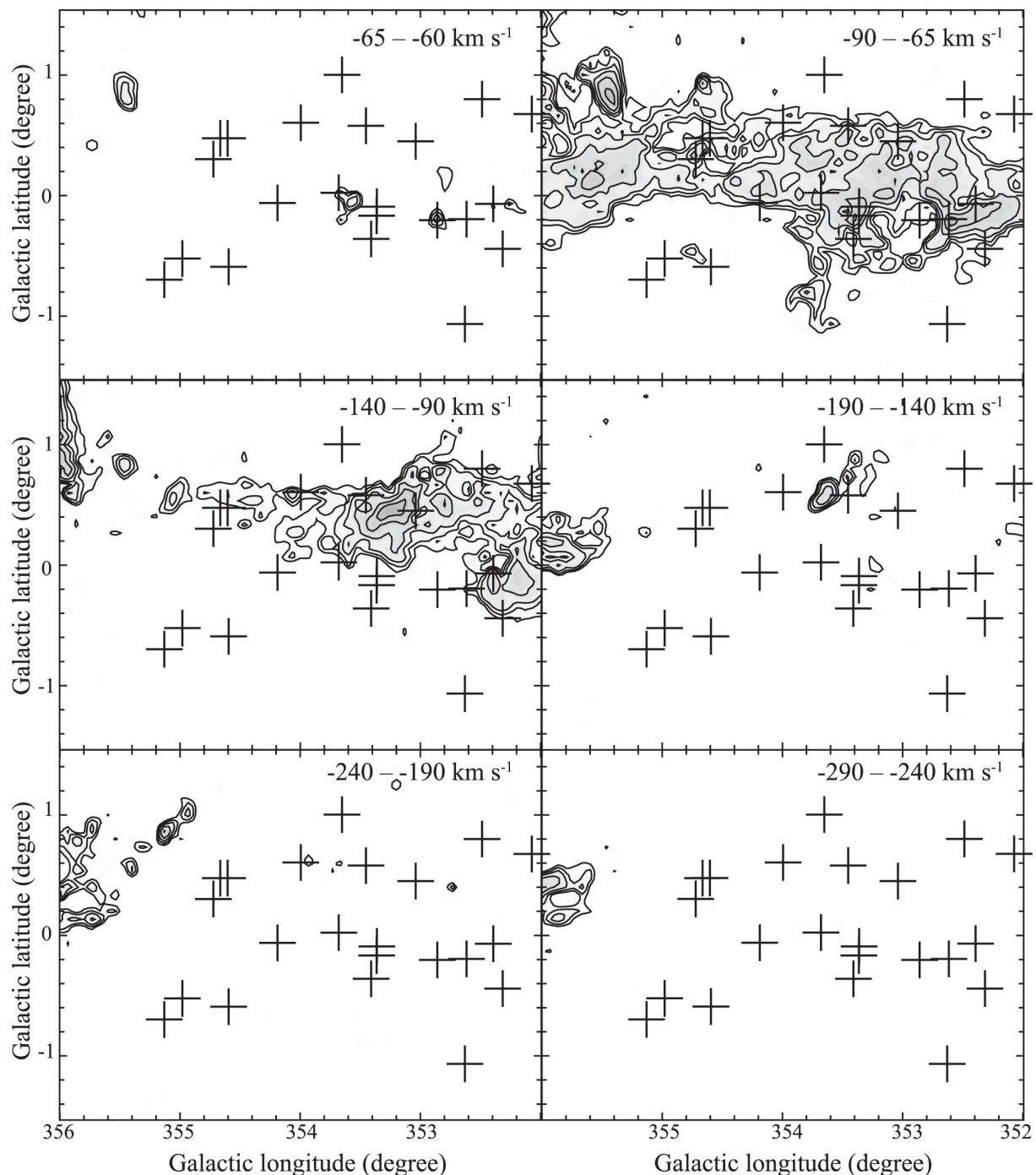
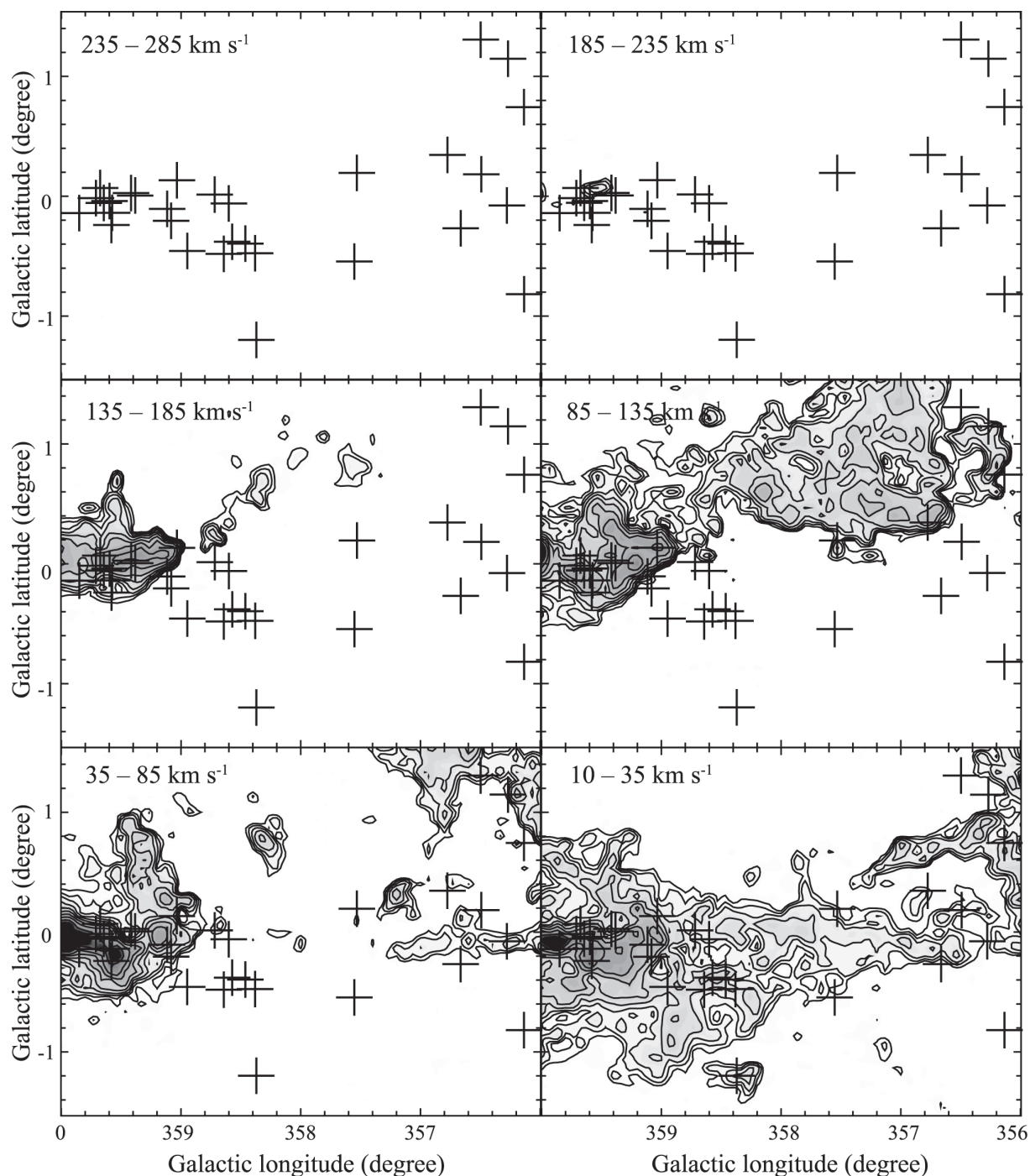


Fig. 4. (b) (Continued)



**Fig. 4.** (c) Same as figure 4(a) but in  $l = 356^\circ\text{--}360^\circ$ .

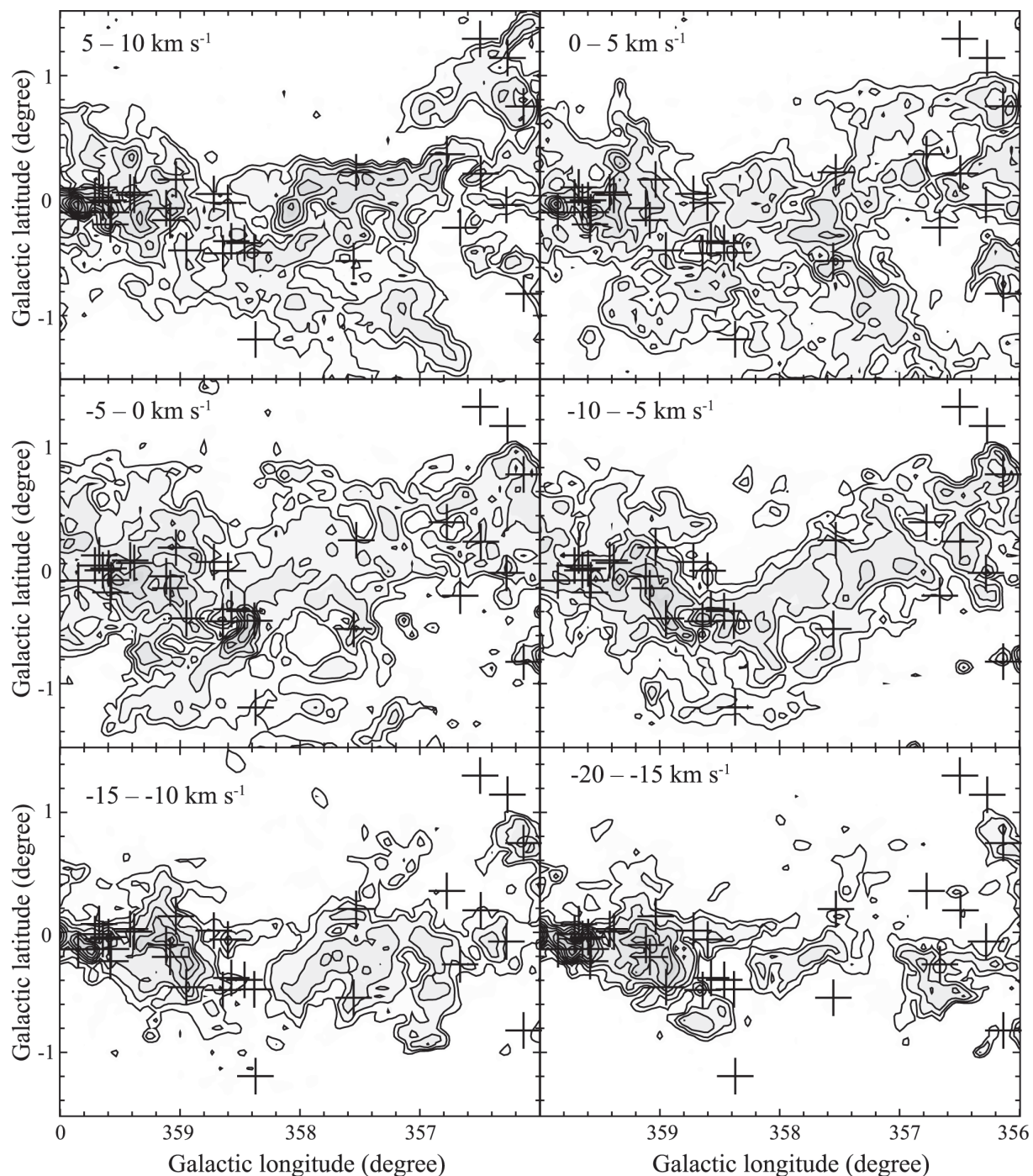
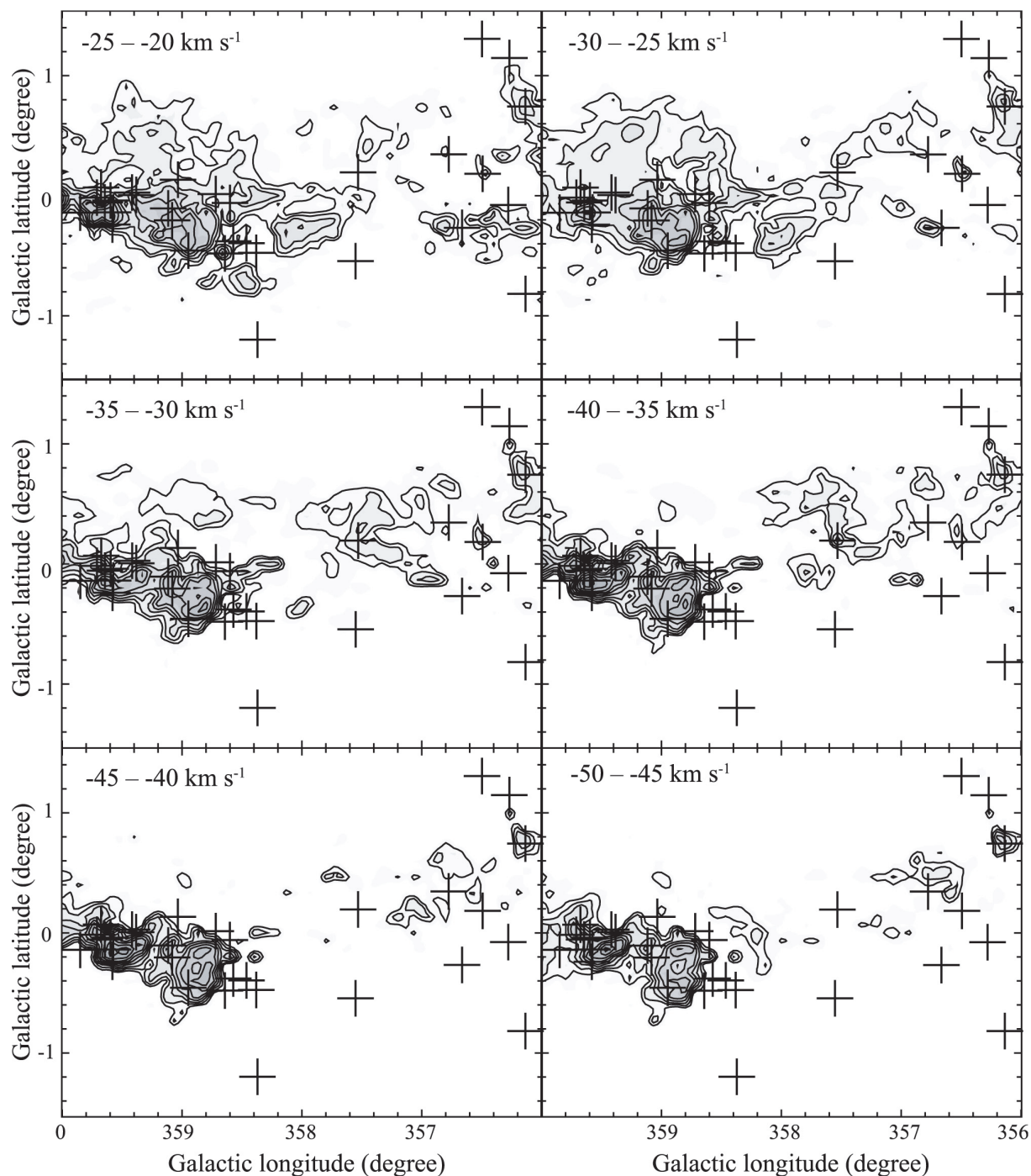


Fig. 4. (c) (Continued)

**Fig. 4.** (c) (Continued)

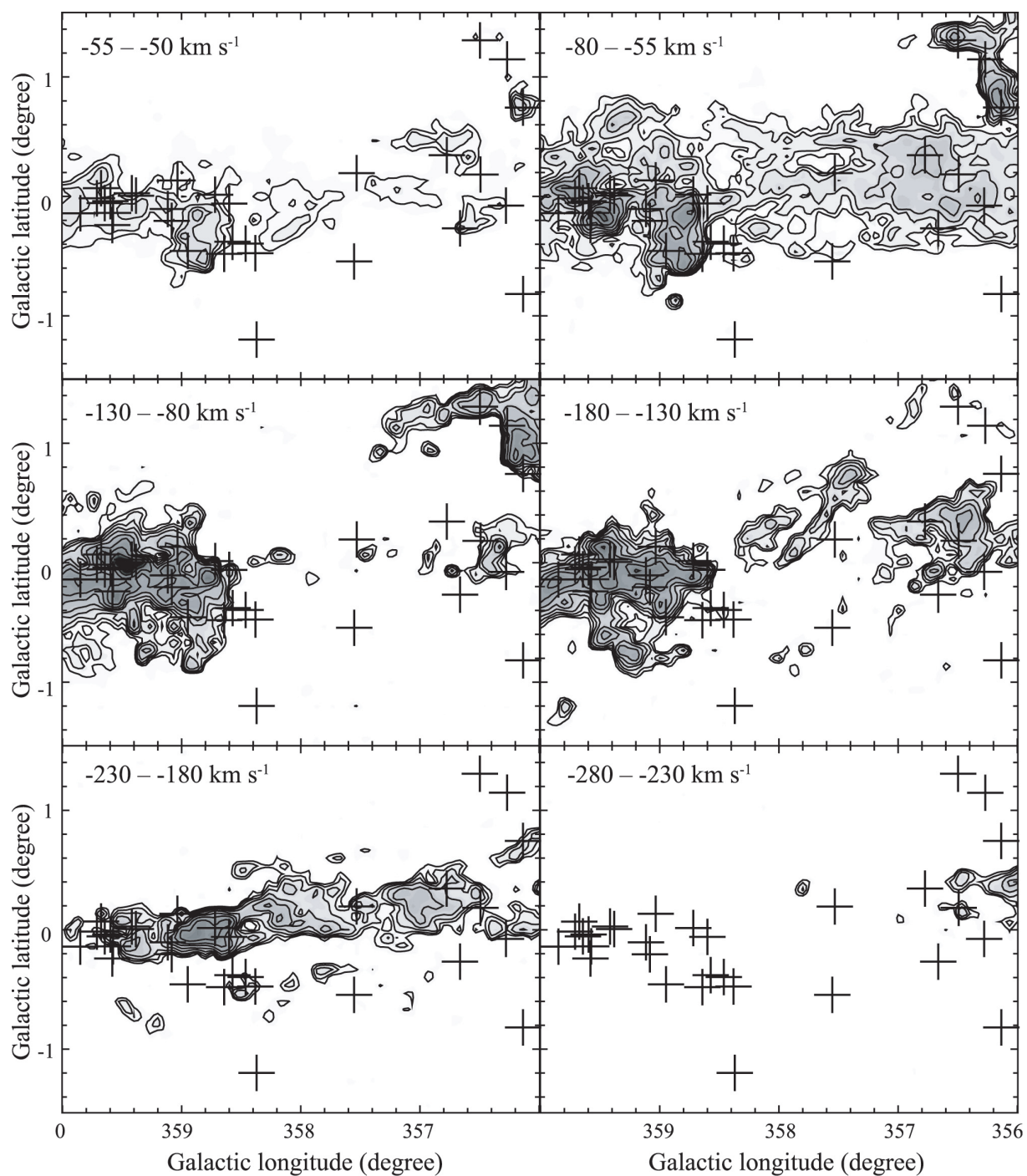
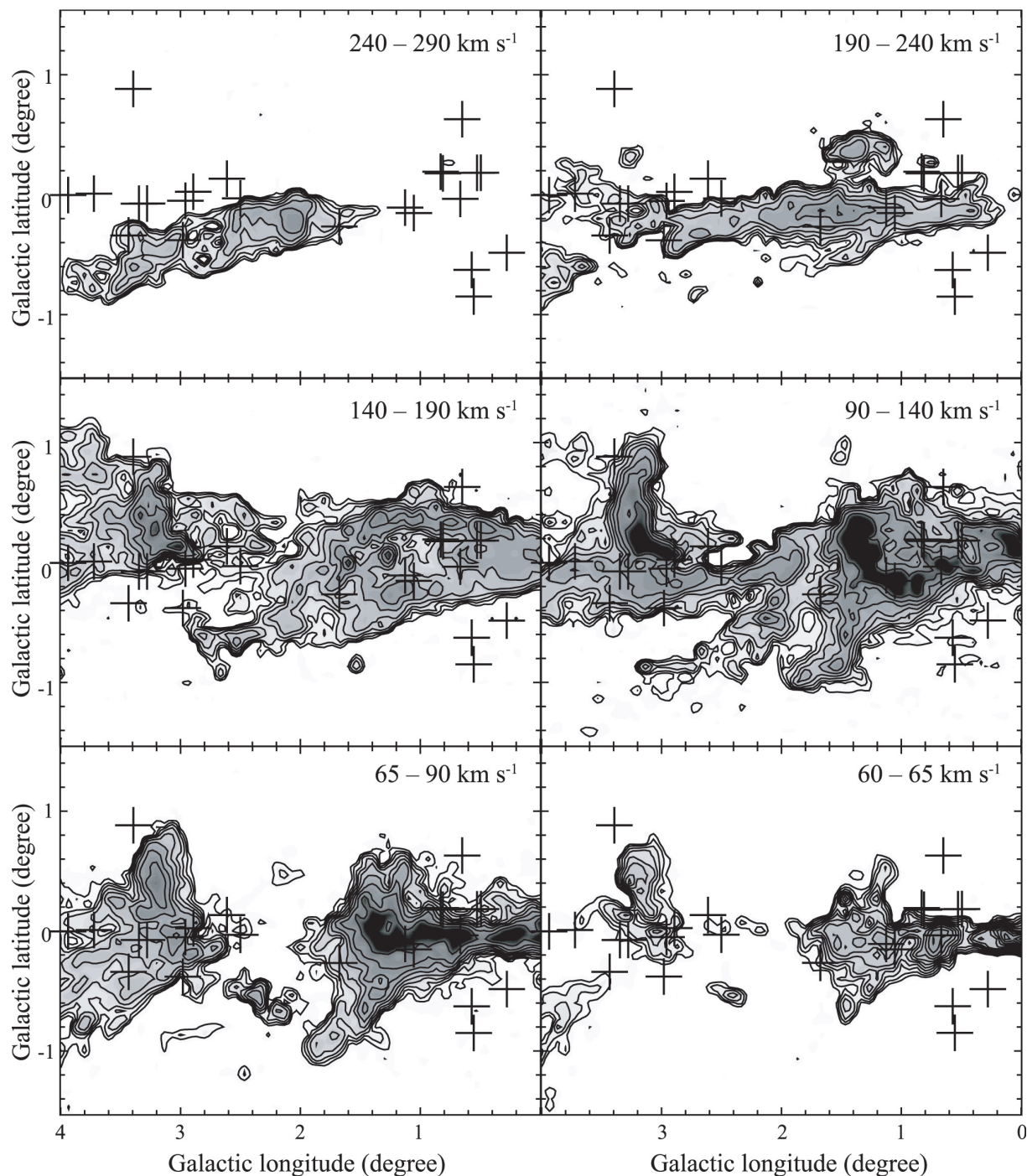


Fig. 4. (c) (Continued)



**Fig. 4.** (d) Same as figure 4(a) but in  $l = 0^\circ - 4^\circ$ .

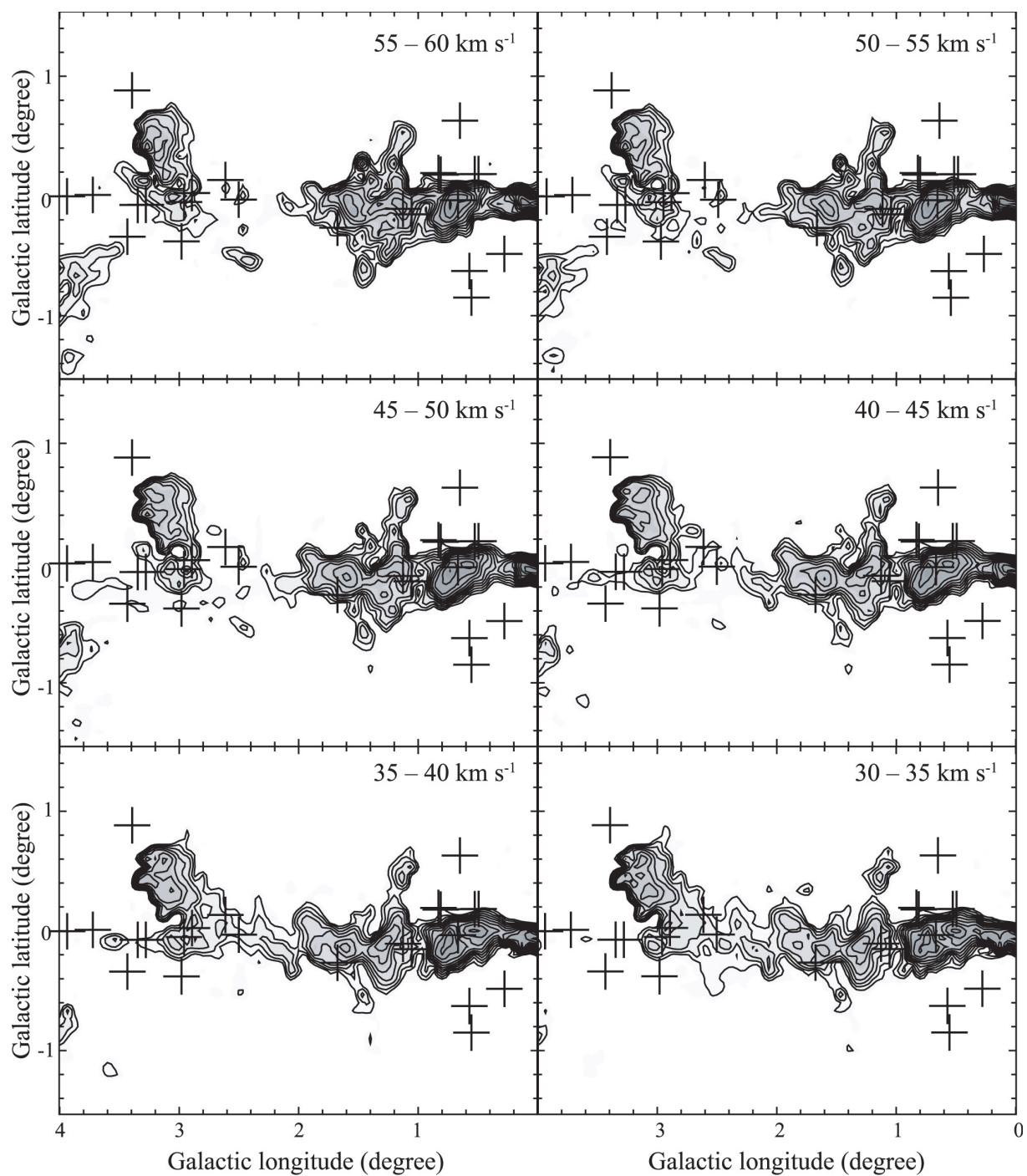


Fig. 4. (d) (Continued)

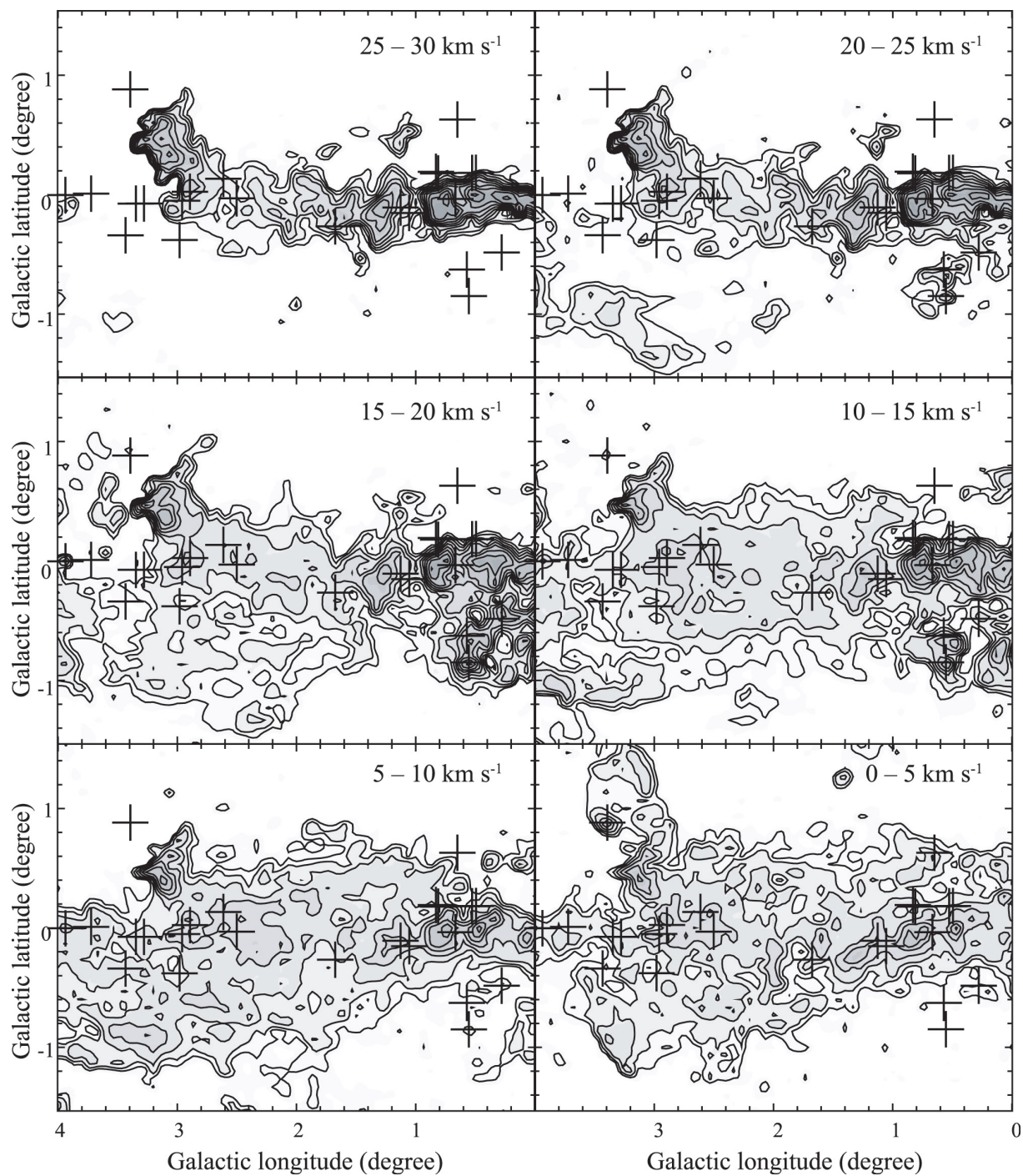


Fig. 4. (d) (Continued)

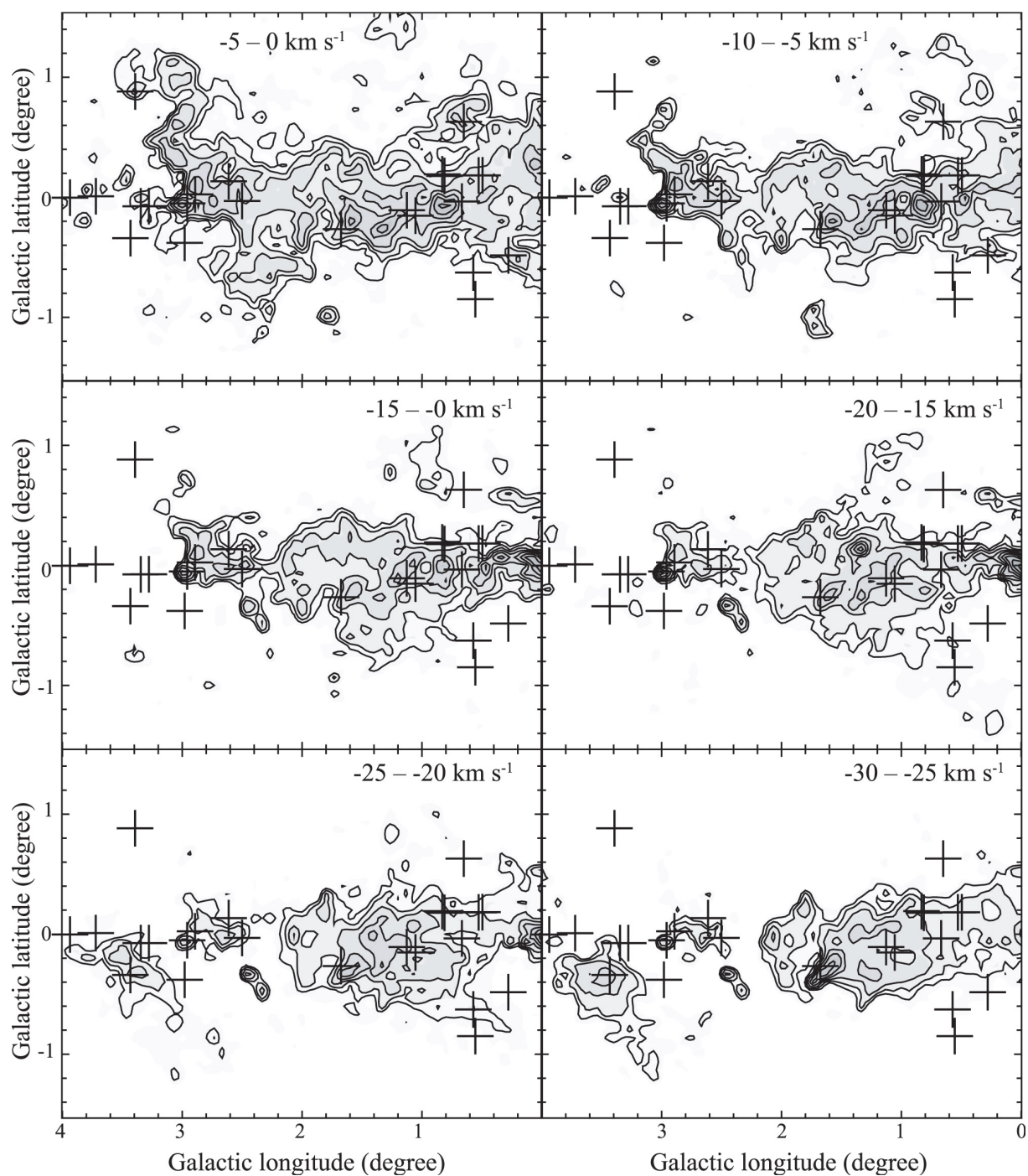
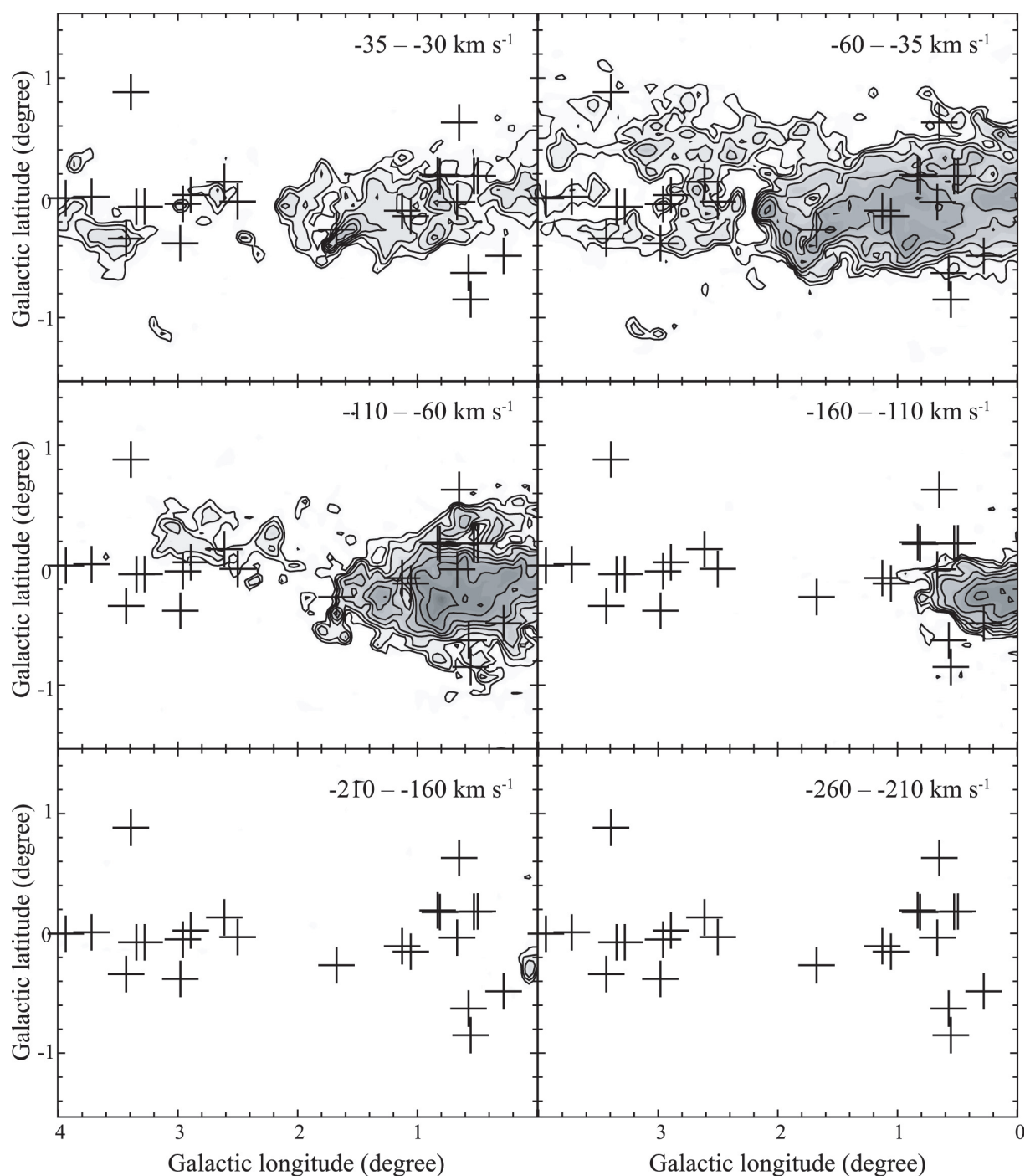
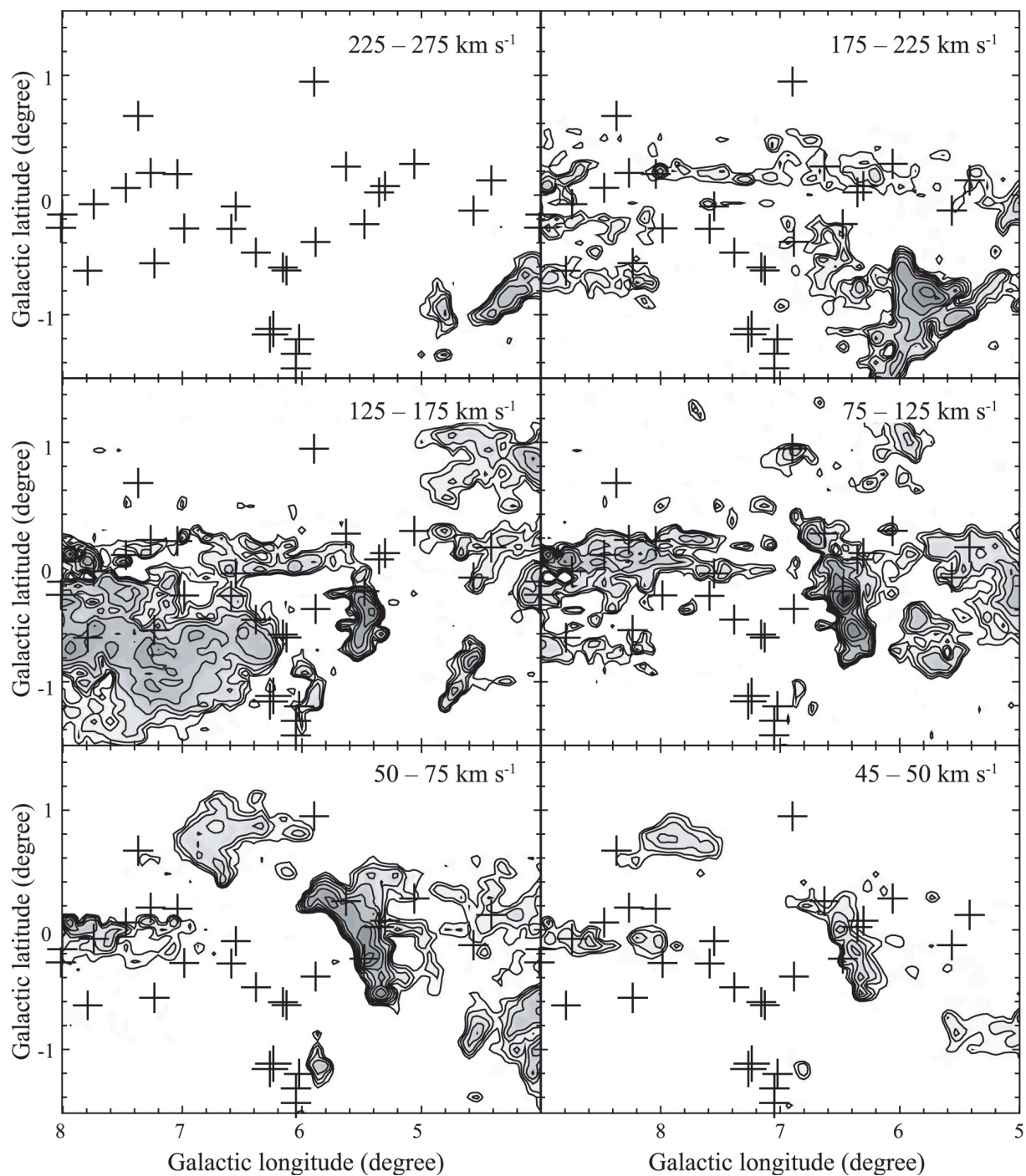


Fig. 4. (d) (Continued)

**Fig. 4.** (d) (Continued)



**Fig. 4.** (e) Same as figure 4(a) but in  $l = 4^{\circ} - 8^{\circ}$ .

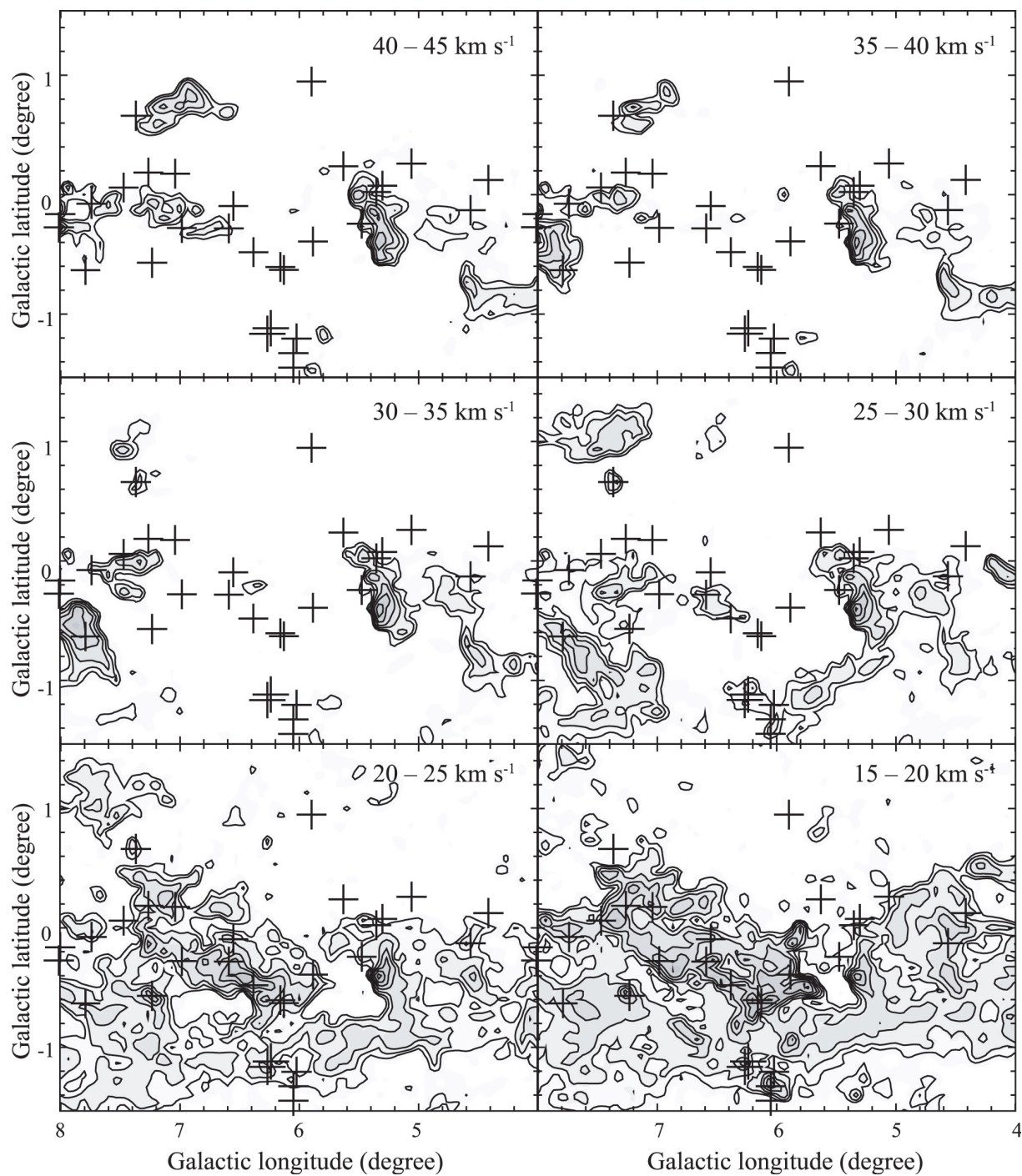


Fig. 4. (e) (Continued)

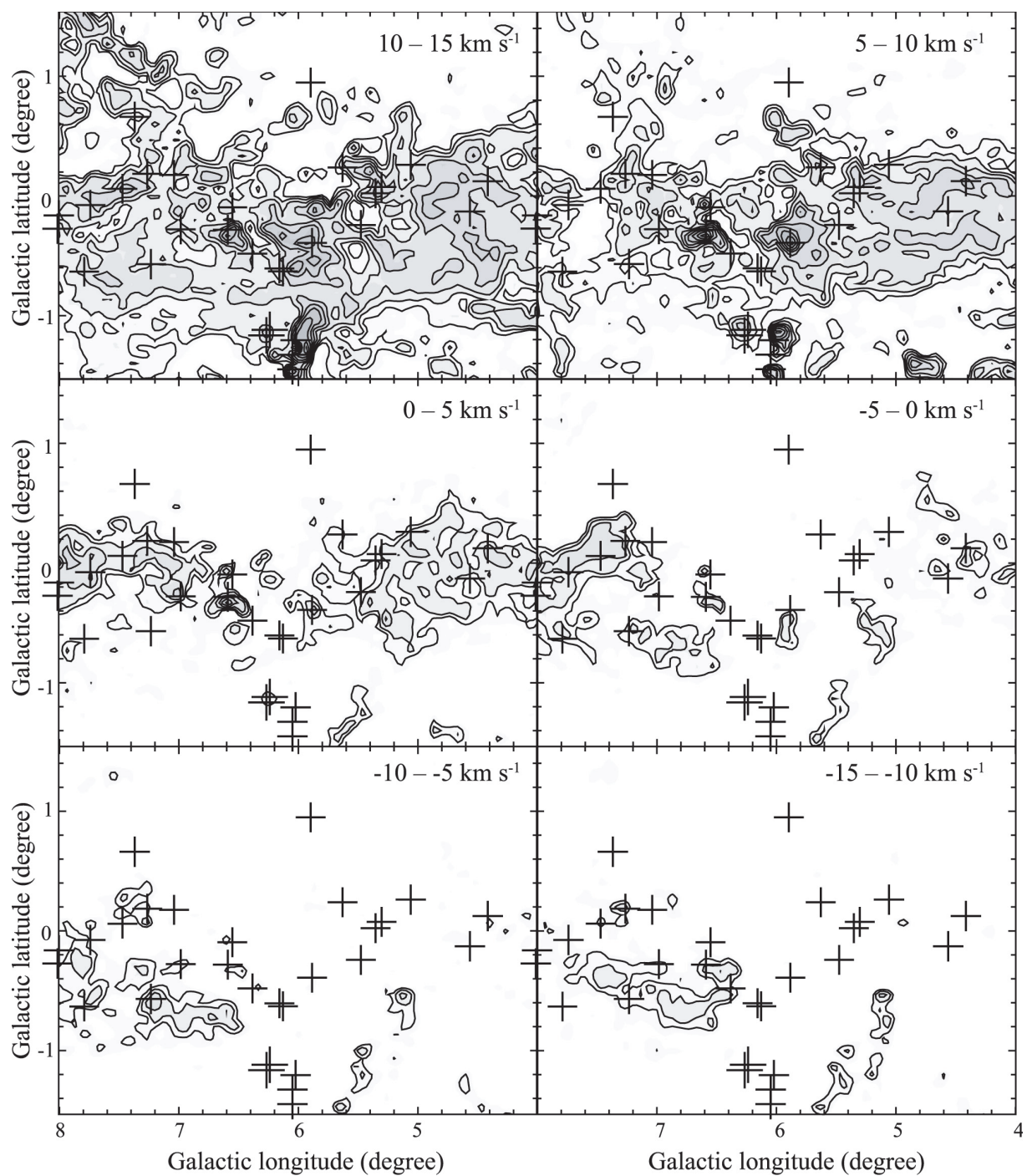


Fig. 4. (e) (Continued)

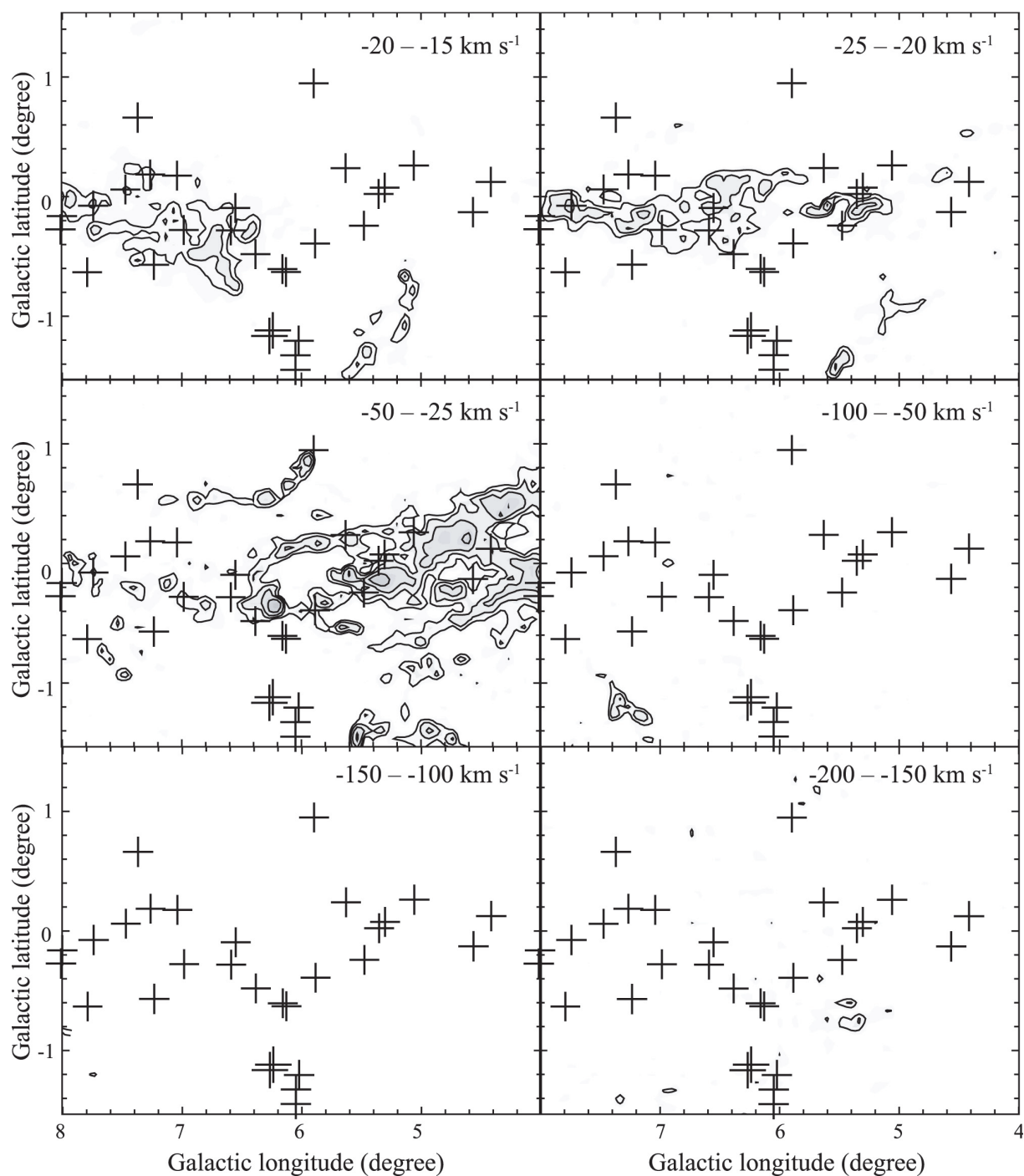


Fig. 4. (e) (Continued)

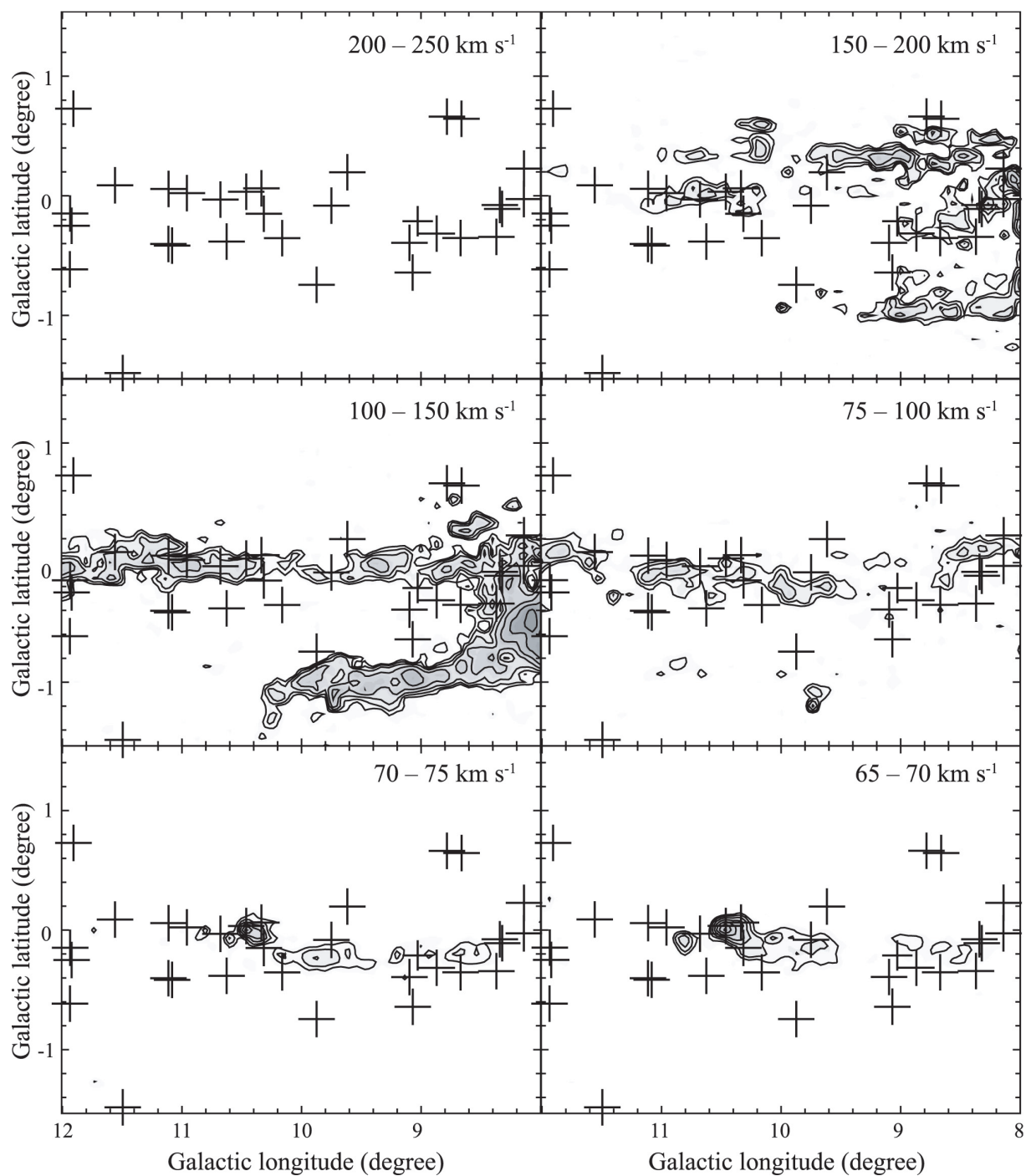
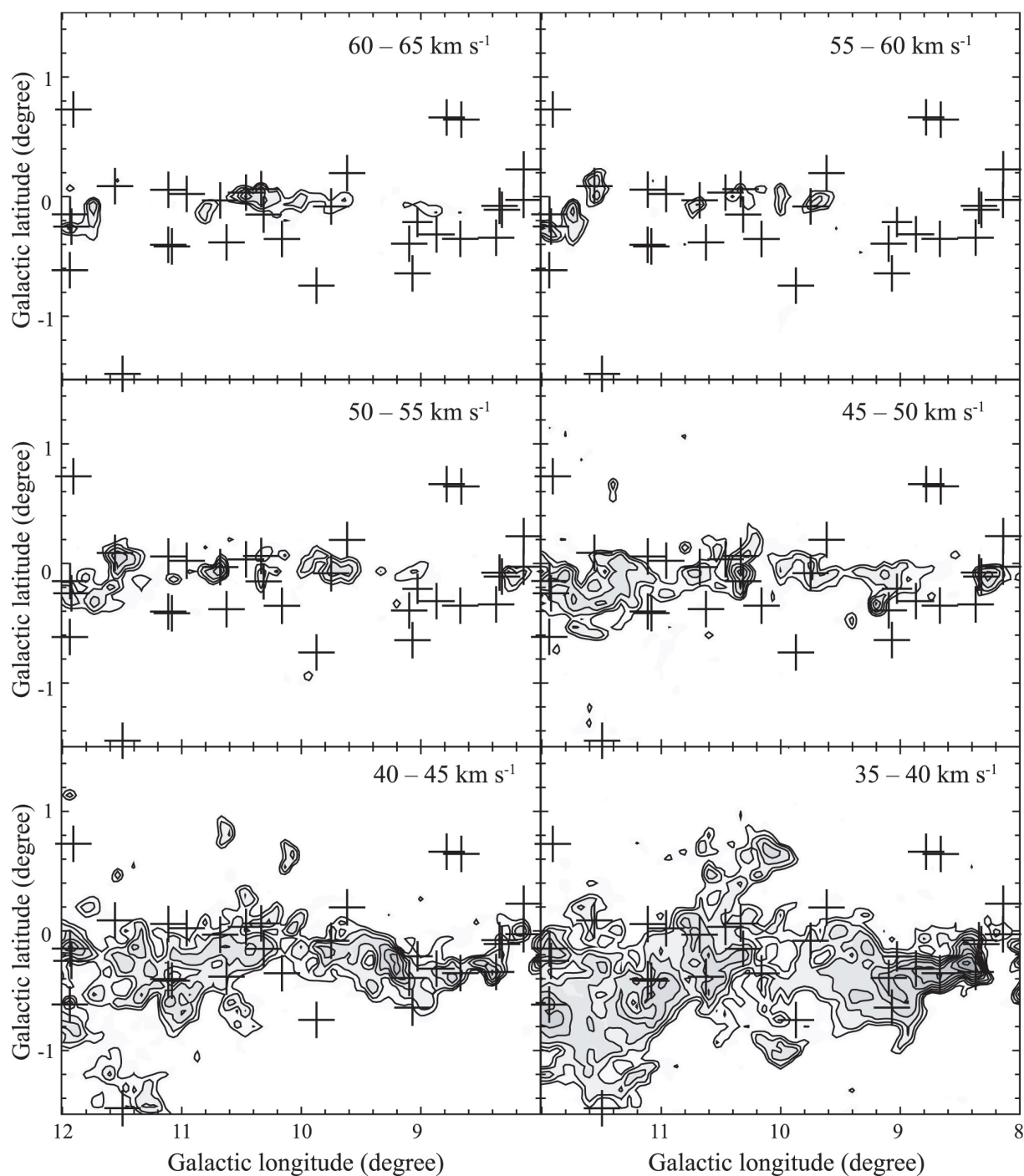


Fig. 4. (f) Same as figure 4(a) but in  $l = 8^\circ - 12^\circ$ .

**Fig. 4.** (f) (Continued)

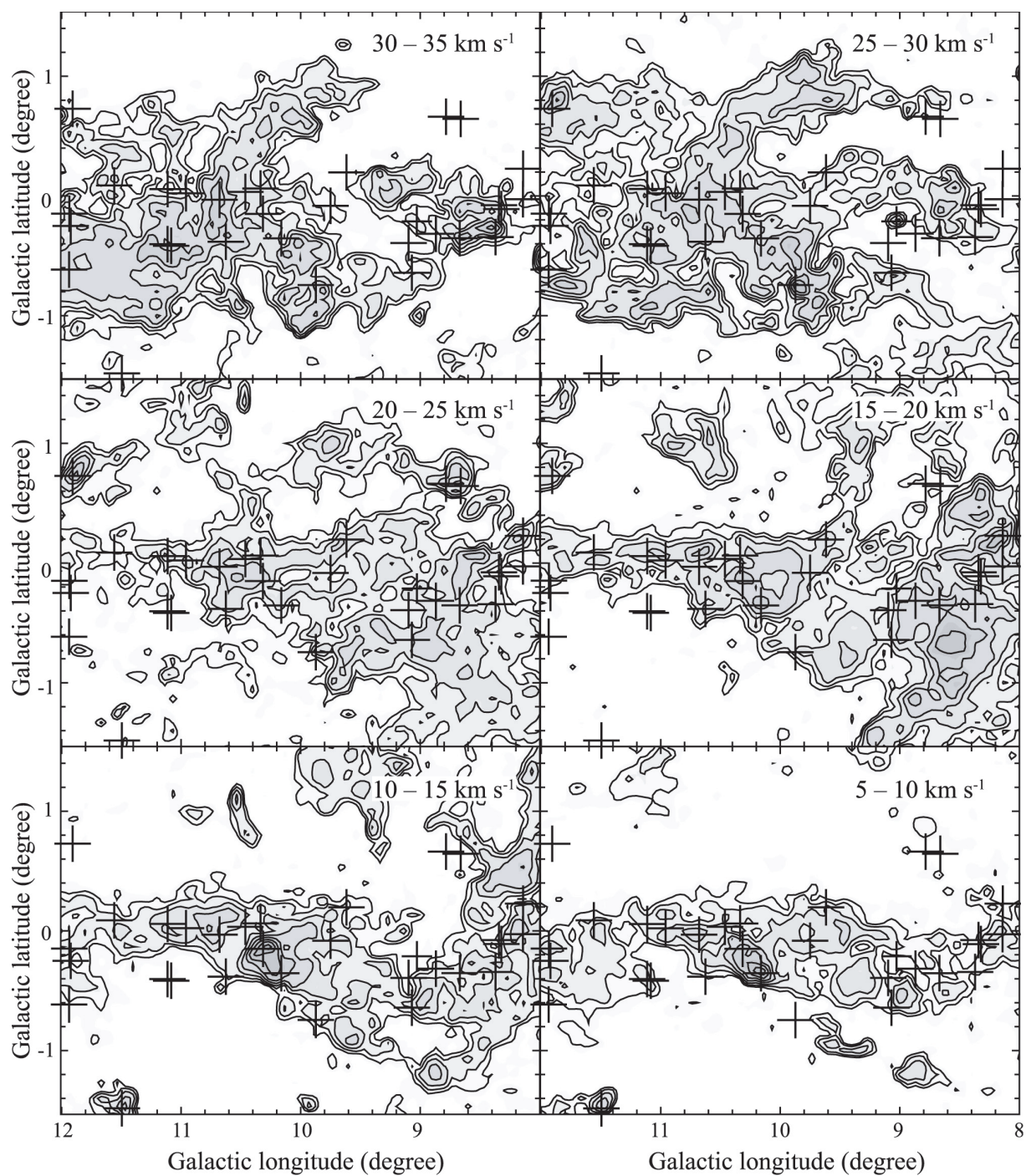


Fig. 4. (f) (Continued)

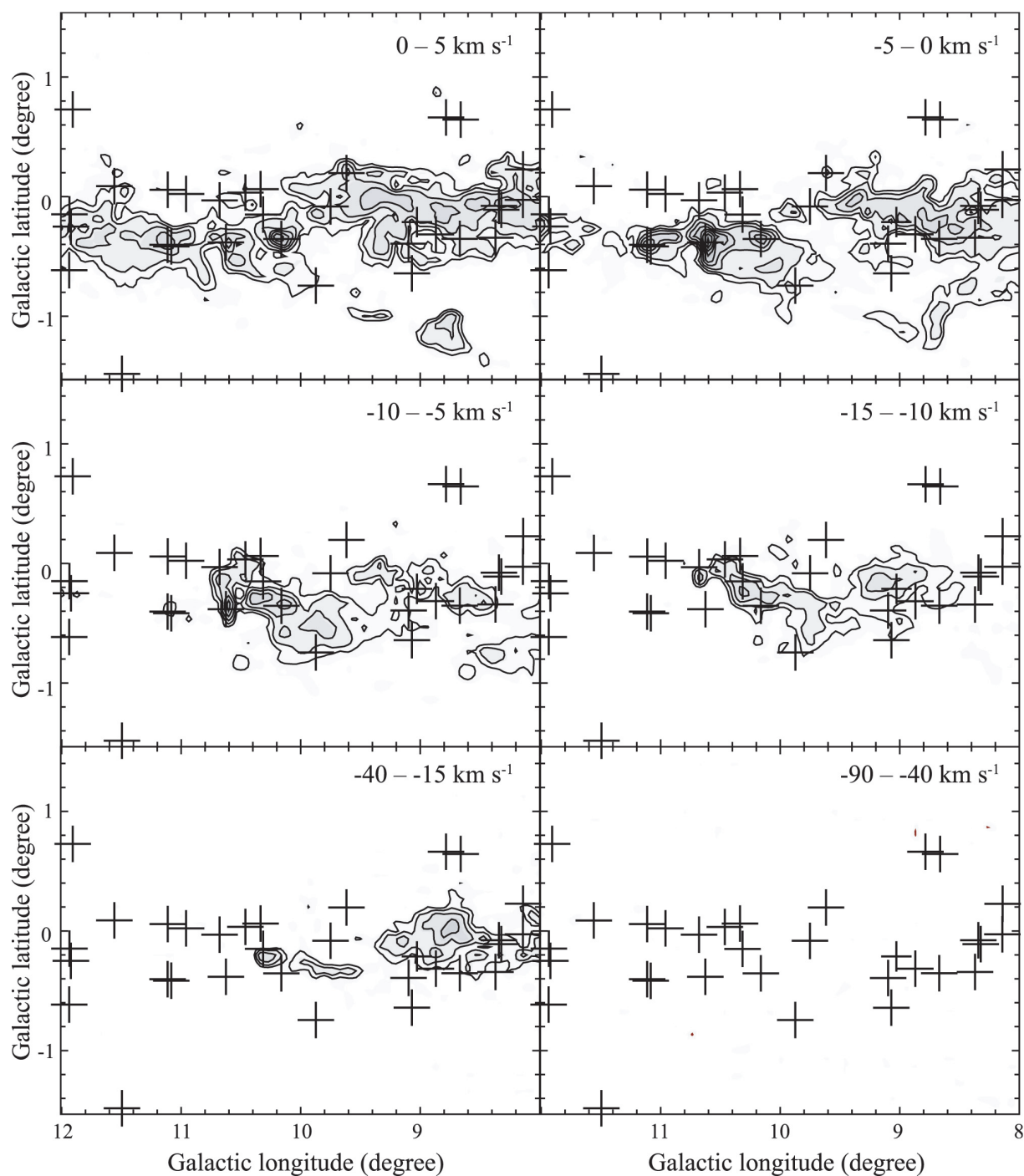
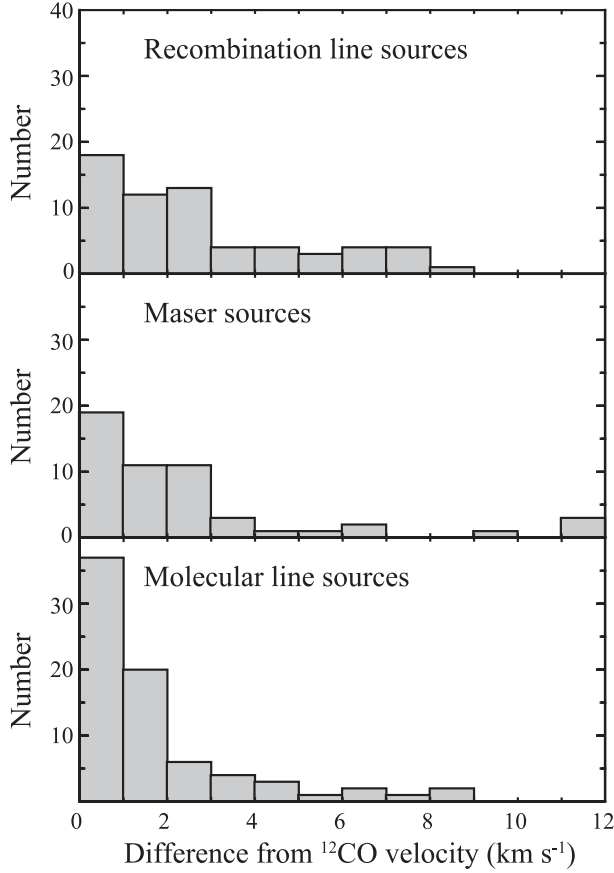


Fig. 4. (f) (Continued)



**Fig. 5.** Histograms of the velocity difference between  $^{12}\text{CO}$  and those of the associated sources. About 87% of the sources have velocity difference smaller than  $5\text{ km s}^{-1}$ .

of the CO molecular emission in this catalog and those of associated objects for  $^{12}\text{CO}$  in figure 5 and for  $^{13}\text{CO}$  in figure 6. These figures indicate that most of the velocity differences are within  $3\text{ km s}^{-1}$ , showing a good agreement. We in addition give observed parameters of the CO emission toward these 169 positions in table 2 and associated IRAS source parameters in table 3.

#### 4.2. Measurement Uncertainty in the Identification

We consider the detection limit as being one factor that may result in an apparent velocity difference of over  $5\text{ km s}^{-1}$ . We selected the objects lying more than  $5\text{ km s}^{-1}$  from a CO peak and plotted the distribution of the dispersion between their velocities and  $^{12}\text{CO}$  radial velocity (figure 7). The horizontal error bars correspond to the  $^{12}\text{CO}$  measurement errors, and the vertical error bars to those of the other objects. The error bars in  $^{12}\text{CO}$  arise from the line widths of the spectra. Most of the  $^{12}\text{CO}$  error bars in figure 7 are several  $10\text{ km s}^{-1}$ . The cause is either (1) a difficulty to disentangle emission from objects overlapping along the line of sight, or (2) intrinsically wide spectra originating from the Galactic center region (e.g., M 000.7–0.0). Radio recombination line data (Caswell & Haynes 1987; Lockman 1989; Lockman et al. 1996) that we used in the catalog show typical line widths of  $\sim 25\text{ km s}^{-1}$  (Lockman et al. 1996). On the other hand, maser sources

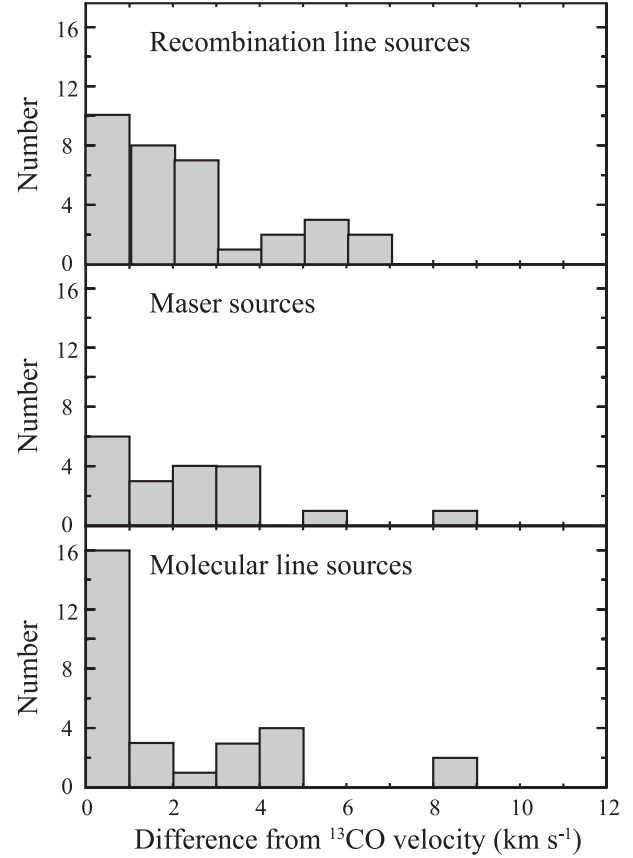


**Fig. 6.** Histograms of the velocity difference between  $^{13}\text{CO}$  and those of the associated sources. About 89% of the sources have separations smaller than  $5\text{ km s}^{-1}$ .

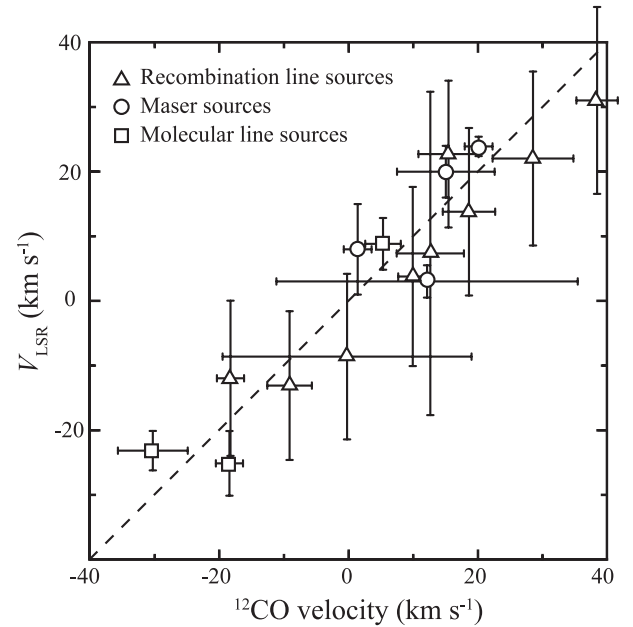


**Fig. 7.** Correlation in velocity between  $^{12}\text{CO}$  and the other astronomical objects for those which show velocity differences of more than  $5\text{ km s}^{-1}$  compared to  $^{12}\text{CO}$ . The dashed line represents  $V_{\text{LSR}}(\text{CO}) = V_{\text{LSR}}(\text{objects})$ .

**Table 2.** CO observational parameters.

Cloud ID	$^{12}\text{CO}$ ( $J = 1-0$ )					$^{13}\text{CO}$ ( $J = 1-0$ )				
	$l^*$ ( $^{\circ}$ )	$b^*$ ( $^{\circ}$ )	$T_{\text{R}}^*$ (K)	$V_{\text{LSR}}$ (km s $^{-1}$ )	$\Delta V$ (km s $^{-1}$ )	$l^*$ ( $^{\circ}$ )	$b^*$ ( $^{\circ}$ )	$T_{\text{R}}^*$ (K)	$V_{\text{LSR}}$ (km s $^{-1}$ )	$\Delta V$ (km s $^{-1}$ )
M 348.1+0.3	348.13	+0.27	6.9	-70.3	8.4	—	—	—	—	—
M 348.3-1.0	348.27	-1.00	11.0	-15.3	10.1	—	—	—	—	—
M 348.3+0.4	348.27	+0.40	15.8	-8.5	7.7	—	—	—	—	—
M 348.5+0.1	348.50	+0.13	7.8	-65.9	14.6	—	—	—	—	—
				4.7	-24.0	8.3	—	—	—	—
M 348.5-1.0	348.53	-1.00	13.1	-13.5	12.3	—	—	—	—	—
M 348.7-1.1	348.73	-1.07	26.2	-12.5	8.6	—	—	—	—	—
M 349.1+0.1	349.07	+0.13	6.7	-76.3	12.2	—	—	—	—	—
M 349.1+0.0	349.13	+0.00	3.0	-92.1	20.5	—	—	—	—	—
M 349.5+0.2	349.53	+0.20	11.0	-21.0	5.6	—	—	—	—	—
M 349.6-0.6	349.60	-0.60	8.3	-16.0	4.8	—	—	—	—	—
M 349.7-1.1	349.67	-1.07	12.0	-25.3	6.2	—	—	—	—	—
M 349.9-0.5	349.87	-0.53	8.5	-23.0	12.7	—	—	—	—	—
M 350.0-1.3	350.00	-1.33	10.1	-20.0	5.4	—	—	—	—	—
M 350.1+0.1	350.13	+0.07	12.4	-67.5	17.5	—	—	—	—	—
M 350.3+0.1	350.33	+0.13	8.1	-60.6	8.1	—	—	—	—	—
M 350.5-0.4	350.52	-0.40	8.0	-21.0	12.7	—	—	—	—	—
M 350.5+1.0	350.53	+0.98	25.6	-10.6	4.8	—	—	—	—	—
M 350.7-0.5	350.67	-0.47	12.3	-18.4	6.6	—	—	—	—	—
M 350.7+0.9	350.73	+0.93	18.0	-8.2	6.8	—	—	—	—	—
M 350.8+0.0	350.80	+0.00	12.4	-5.5	3.3	—	—	—	—	—
M 350.8-0.8	350.80	-0.82	6.8	-22.6	8.1	—	—	—	—	—
M 351.1-0.3	351.07	-0.33	8.8	-17.9	10.2	—	—	—	—	—
M 351.2+0.7	351.20	+0.67	24.9	-4.5	6.5	—	—	—	—	—
M 351.4+0.7	351.40	+0.67	35.7	-5.0	10.0	—	—	—	—	—
M 351.5+0.2	351.53	+0.20	10.0	-41.8	11.5	—	—	—	—	—
M 351.5-0.5	351.53	-0.47	6.5	-23.9	7.9	—	—	—	—	—
M 351.6-1.3	351.60	-1.27	17.2	-11.8	12.3	—	—	—	—	—
M 351.6-0.3	351.60	-0.33	8.5	-92.6	12.8	—	—	—	—	—
M 351.7-1.1	351.67	-1.13	23.4	-9.1	6.9	—	—	—	—	—
M 351.8-0.5	351.80	-0.53	13.3	-4.7	9.3	—	—	—	—	—
M 352.1+0.7	352.07	+0.67	13.0	0.1	8.9	—	—	—	—	—
M 352.3-0.5	352.33	-0.47	14.7	-12.4	7.8	—	—	—	—	—
M 352.4-0.1	352.40	-0.07	9.0	-89.8	8.3	—	—	—	—	—
M 352.5+0.8	352.53	+0.80	9.7	-3.6	3.3	—	—	—	—	—
M 352.6-1.1	352.60	-1.07	7.1	-0.3	6.4	—	—	—	—	—
M 352.6-0.2	352.60	-0.20	13.2	-84.6	8.2	—	—	—	—	—
M 352.9-0.2	352.87	-0.20	9.3	-58.2	9.5	—	—	—	—	—
M 353.0+0.5	353.00	+0.47	19.3	-4.6	7.4	—	—	—	—	—
M 353.3-0.2	353.33	-0.19	3.9	-82.6	10.3	—	—	—	—	—
M 353.4-0.3	353.40	-0.33	15.5	-17.2	9.7	—	—	—	—	—
M 353.4-0.1	353.40	-0.07	7.8	-49.0	16.7	—	—	—	—	—
M 353.5+0.6	353.45	+0.58	8.1	-46.4	5.7	—	—	—	—	—
M 353.5+1.0	353.66	+1.00	16.0	-2.9	3.0	—	—	—	—	—
M 353.7+0.0	353.67	+0.00	7.5	-55.6	8.4	—	—	—	—	—
M 354.0+0.6	354.00	+0.60	6.8	-20.7	4.0	—	—	—	—	—
M 354.1-0.1	354.13	-0.07	7.1	-34.3	6.3	354.13	-0.07	2.6	-33.3	7.8
M 354.6-0.6	354.60	-0.60	9.1	-3.4	8.8	354.60	-0.60	4.3	-2.5	4.9
M 354.6+0.5	354.60	+0.47	17.0	-21.2	6.9	354.60	+0.47	5.9	-21.2	4.6
M 354.7+0.3	354.73	+0.33	9.4	82.2	31.1	354.73	+0.33	1.6	90.4	36.2
M 355.0-0.5	355.00	-0.53	14.3	-4.5	6.6	355.00	-0.53	1.7	0.1	4.1
M 355.1-0.7	355.13	-0.73	8.3	9.0	2.2	355.13	-0.73	2.3	9.2	2.1
M 356.1-0.8	356.13	-0.80	5.5	-5.4	5.7	356.13	-0.80	1.0	-6.5	4.8

Table 2. (Continued)

Cloud ID	$^{12}\text{CO}$ ( $J = 1-0$ )					$^{13}\text{CO}$ ( $J = 1-0$ )				
	$l^*$ ( $^{\circ}$ )	$b^*$ ( $^{\circ}$ )	$T_{\text{R}}^*$ (K)	$V_{\text{LSR}}$ ( $\text{km s}^{-1}$ )	$\Delta V$ ( $\text{km s}^{-1}$ )	$l^*$ ( $^{\circ}$ )	$b^*$ ( $^{\circ}$ )	$T_{\text{R}}^*$ (K)	$V_{\text{LSR}}$ ( $\text{km s}^{-1}$ )	$\Delta V$ ( $\text{km s}^{-1}$ )
M 356.1+0.7	356.13	+0.73	5.0	-62.8	35.6	356.17	+0.70	0.7	-57.7	26.6
M 356.3+1.1	356.27	+1.13	4.4	-99.9	26.6	—	—	—	—	—
M 356.3-0.1	356.27	-0.07	10.3	-5.5	2.1	356.27	-0.07	3.1	-5.0	4.1
M 356.5+0.2	356.47	+0.20	1.3	-55.0	6.1	N	—	—	—	—
M 356.5+1.3	356.53	+1.33	4.1	-72.6	38.1	—	—	—	—	—
M 356.7-0.3	356.67	-0.27	5.0	-52.9	7.9	356.67	-0.27	2.3	-52.6	4.0
M 356.8+0.3	356.80	+0.33	4.1	103.0	22.5	356.80	+0.33	1.3	106.7	8.7
M 357.5+0.2	357.53	+0.20	8.9	-36.5	4.8	357.53	+0.20	3.9	-36.6	3.4
M 357.5-0.5	357.53	-0.53	8.7	0.8	6.4	357.53	-0.57	5.9	0.8	4.1
M 357.6-0.1	357.60	-0.07 <sup>†</sup>	7.8	5.4	5.5	357.60	-0.07	2.2	4.5	7.0
			4.3	-13.6	—	N	—	—	—	—
M 358.4-1.2	358.40	-1.20	4.5	16.6	7.0	N	—	—	—	—
M 358.4-0.5	358.40	-0.47	13.4	-3.9	7.0	358.40	-0.47	6.9	-4.0	4.3
M 358.5-0.4	358.47	-0.40	9.2	-3.2	11.5	358.47	-0.36	6.3	-3.8	4.2
M 358.5-0.4	358.53	-0.40	10.5	16.3	4.5	358.53	-0.40	4.3	16.2	3.5
M 358.6-0.1	358.60	-0.07	6.0	-211.6	12.3	358.60	-0.07	1.2	-211.0	7.5
			3.1	-138.9	48.9	N	—	—	—	—
M 358.7-0.5	358.67	-0.47	9.5	-20.9	6.4	358.67	-0.47	3.3	-20.6	4.1
			9.1	-6.6	9.7	—	2.8	-6.2	5.8	—
M 358.7+0.0	358.73	+0.00	11.5	-208.9	19.4	358.73	+0.00	3.1	-210.2	14.9
M 358.9-0.5	358.93	-0.47	11.1	-7.5	6.5	358.93	-0.50	1.2	-9.3	11.3
M 359.1+0.1	359.07	+0.13	10.2	132.4	34.6	359.03	+0.13	1.2	130.0	17.5
M 359.1-0.2	359.07	-0.20	8.6	-128.3	26.9	359.07	-0.17	2.0	-130.8	18.6
			11.5	-21.2	—	359.07	-0.17 <sup>†</sup>	1.3	-21.8	—
M 359.1-0.1	359.13	-0.13	10.1	-35.0	36.4	359.13	-0.13 <sup>†</sup>	1.0	-37.5	—
M 359.4+0.0	359.40	+0.00	13.8	-120.5	47.5	359.40	+0.00	3.1	-122.4	30.6
M 359.4+0.1	359.40	+0.07	10.3	1.5	4.3	359.40	+0.07	3.6	1.2	4.9
M 359.6-0.1	359.60	-0.13 <sup>†</sup>	13.2	-23.5	—	359.60	-0.13 <sup>†</sup>	2.6	-22.6	—
M 359.6-0.1	359.60	-0.07 <sup>†</sup>	5.8	-170.3	—	359.60	-0.07 <sup>†</sup>	0.8	-169.3	—
M 359.6-0.3	359.60	-0.27	5.7	-93.7	82.0	N	—	—	—	—
			21.2	18.5	—	359.60	-0.23	8.3	18.5	5.2
M 359.7-0.1	359.67	-0.07	10.0	-41.3	6.4	359.67	-0.07	1.9	-42.6	2.2
			12.8	15.1	16.7	—	1.8	13.0	20.6	—
M 359.7+0.1	359.67	+0.07 <sup>†</sup>	11.0	-84.3	—	359.67	+0.07	0.8	-81.2	39.0
M 359.7-0.0	359.73	-0.00 <sup>†</sup>	9.4	-65.8	—	359.73	-0.00	2.8	-60.8	17.9
			13.4	-39.9	—	—	2.6	-39.8	26.8	—
M 359.9-0.1	359.87	-0.13	9.4	-131.7	45.8	359.87	-0.13	1.3	-135.8	34.9
M 000.3-0.5	0.27	-0.47	13.3	17.4	6.7	0.27	-0.43	7.3	17.1	4.2
M 000.5-0.7	0.47	-0.67	13.4	14.8	7.0	N	—	—	—	—
M 000.5+0.1	N	—	—	—	—	0.50	+0.13	2.6	3.3	6.1
M 000.5+0.2	N	—	—	—	—	0.50	+0.17	2.8	-1.0	14.1
M 000.5-0.7	0.53	-0.67	13.4	16.5	9.7	N	—	—	—	—
M 000.6-0.9	0.53	-0.87	19.6	16.4	8.4	0.57	-0.87	9.3	16.8	5.4
M 000.7+0.6	0.66	+0.60	4.9	-0.8	11.3	0.63	+0.60	4.1	-1.4	3.8
M 000.7-0.0	0.66	+0.00	19.5	57.5	98.3	0.66	-0.03	7.6	62.6	34.2
M 000.8+0.2	—	—	—	—	—	0.83	+0.23	2.0	5.7	7.3
M 001.1-0.1	1.07	-0.13	15.9	123.7	16.9	1.03	-0.13	1.9	124.0	17.8
M 001.1-0.1	N	—	—	—	—	1.13	-0.10	3.8	-17.5	6.3
M 001.3+0.1	1.33	+0.13	16.4	-18.2	4.2	1.33	+0.13	5.8	-17.0	3.5
M 001.7-0.3	1.67	-0.33 <sup>†</sup>	11.3	-28.0	—	1.70	-0.40	1.6	-38.2	26.6
M 002.5-0.0	2.47	-0.00	6.9	-0.2	38.5	2.53	-0.03	1.6	5.9	24.4
M 002.6+0.1	2.60	+0.13	5.0	12.2	46.6	2.63	+0.13	2.3	11.8	12.0
			3.8	95.3	7.9	—	1.9	96.0	5.4	—

Table 2. (Continued)

Cloud ID	$^{12}\text{CO}$ ( $J = 1-0$ )					$^{13}\text{CO}$ ( $J = 1-0$ )				
	$l^*$ (°)	$b^*$ (°)	$T_{\text{R}}^*$ (K)	$V_{\text{LSR}}$ (km s $^{-1}$ )	$\Delta V$ (km s $^{-1}$ )	$l^*$ (°)	$b^*$ (°)	$T_{\text{R}}^*$ (K)	$V_{\text{LSR}}$ (km s $^{-1}$ )	$\Delta V$ (km s $^{-1}$ )
M 002.9+0.0	2.93	-0.00 <sup>†</sup>	—	—	—	2.90	+0.03	2.9	-2.2	4.8
M 003.0-0.1	3.00	-0.07	11.3	-15.8	7.1	3.00	-0.07	1.4	-3.3	38.2
M 003.3-0.4	N	—	—	—	—	3.30	-0.37	3.2	6.1	5.5
M 003.3-0.1	3.27	-0.13	5.5	6.1	17.6	3.30	-0.10	2.2	5.2	9.1
M 003.3-0.1	N	—	—	—	—	3.33	-0.10	2.1	7.9	11.6
M 003.4+0.9	3.40	+0.87	14.7	1.0	3.9	3.40	+0.87	6.3	1.1	2.2
M 003.5-0.3	3.53	-0.33	6.1	-30.2	10.8	3.43	-0.30	2.6	-26.3	5.9
M 003.7-0.1	N	—	—	—	—	3.66	-0.10	3.3	6.5	5.9
M 003.8+0.0	N	—	—	—	—	3.77	+0.03	2.7	7.9	7.1
M 003.9+0.0	3.93	+0.00	10.4	16.5	2.4	3.97	+0.00	4.1	16.7	2.2
M 004.0+0.3	4.00	+0.33	10.3	12.6	5.3	4.00	+0.33	4.5	12.6	3.3
M 004.4+0.1	4.40	+0.13	7.4	8.1	15.8	4.37	+0.07	4.0	8.1	10.4
M 004.6-0.1	4.60	-0.13	4.2	25.3	8.2	4.57	-0.10	2.7	13.6	10.8
M 005.0+0.2	N	—	—	—	—	5.03	+0.23	1.2	10.6	4.5
M 005.3+0.1	5.33	+0.07	11.6	12.1	3.9	5.33	+0.07	4.6	11.9	2.9
M 005.5-0.2	5.47	-0.20	4.9	22.3	7.0	5.47	-0.27	2.5	22.6	9.1
M 005.7+0.3	5.67	+0.27	6.1	7.5	7.7	5.63	+0.23	4.0	8.8	6.0
M 005.8-0.1	5.83	-0.13	14.3	6.4	2.0	5.80	-0.17	5.5	5.9	1.9
			7.4	11.9	16.2			2.9	10.9	5.9
M 005.9-0.4	5.87	-0.40	20.7	8.4	7.5	5.90	-0.40	10.2	9.1	4.1
M 005.9+0.9	5.87	+0.93	5.3	80.6	9.5	N	—	—	—	—
M 006.0-1.1	6.00	-1.13	23.8	9.9	4.5	—	—	—	—	—
M 006.0-1.3	6.00	-1.33	15.1	13.7	6.4	—	—	—	—	—
M 006.1-1.5	6.07	-1.47	24.2	10.9	2.9	—	—	—	—	—
M 006.1-0.6	6.07	-0.60	13.6	15.5	9.3	6.13	-0.63	5.8	16.4	5.0
M 006.2-0.6	6.20	-0.60	13.4	17.9	7.3	6.23	-0.60	7.4	17.9	4.4
M 006.2-0.1	N	—	—	—	—	6.23	-0.13	4.3	11.6	8.4
M 006.3-1.1	6.27	-1.13 <sup>†</sup>	9.6	14.4	—	—	—	—	—	—
M 006.4-0.5	6.40	-0.47	8.8	19.2	12.7	6.40	-0.50	3.2	20.4	4.4
M 006.6-0.1	N	—	—	—	—	6.57	-0.10	2.4	15.1	11.5
M 006.6-0.3	6.60	-0.33	25.9	7.7	10.5	6.63	-0.33	5.8	6.5	4.5
			10.5	21.5	9.8			1.6	19.9	12.4
M 006.6-0.1	6.60	-0.07 <sup>†</sup>	10.3	6.7	—	6.63	-0.10	2.7	5.3	1.7
M 007.0-0.3	7.00	-0.27	12.6	18.7	8.1	6.90	-0.23	4.0	19.3	6.8
M 007.1+0.2	7.07	+0.20	7.6	17.7	9.3	7.00	+0.13	3.8	18.5	4.2
M 007.2-0.5	7.20	-0.53	11.5	19.3	9.1	7.27	-0.53	6.3	19.2	3.5
M 007.2+0.2	N	—	—	—	—	7.23	+0.17 <sup>†</sup>	1.4	15.9	—
M 007.3-0.1	7.27	-0.13	8.5	22.2	6.9	7.27	-0.13	1.8	21.2	9.4
M 007.3+0.7	7.33	+0.67	4.0	28.6	12.5	7.37	+0.67	2.7	24.5	5.1
M 007.5+0.1	7.47	+0.07 <sup>†</sup>	1.7	-20.4	—	N	—	—	—	—
			9.5	14.0	8.5	7.47	+0.07	4.0	15.3	3.0
M 007.6-0.1	7.60	-0.13	4.0	13.9	5.5	7.73	-0.07	1.9	14.8	3.8
M 007.7-0.7	7.73	-0.67	8.3	30.8	7.2	7.83	-0.60	3.6	32.4	5.8
M 008.0-0.3	8.00	-0.27	11.0	40.9	5.5	8.00	-0.27	3.6	40.5	3.7
M 008.0-0.1	8.00	-0.13	11.2	40.0	3.7	8.00	-0.17	3.2	40.2	3.0
M 008.1-0.0	8.13	-0.00	7.6	41.6	4.1	—	—	—	—	—
M 008.2+0.2	8.20	+0.20	16.1	19.0	6.5	—	—	—	—	—
M 008.3-0.1	8.27	-0.07	6.7	49.2	7.3	—	—	—	—	—
M 008.4-0.3	8.40	-0.33	21.5	38.1	7.6	—	—	—	—	—
M 008.6-0.3	8.60	-0.33	12.8	35.8	8.3	—	—	—	—	—
M 008.7+0.7	8.67	+0.67	4.6	23.3	3.9	—	—	—	—	—
M 008.8+0.7	8.80	+0.67	8.3	22.6	5.9	—	—	—	—	—
M 008.9-0.3	8.87	-0.33	16.0	38.5	6.4	—	—	—	—	—

**Table 2.** (Continued)

Cloud ID	$^{12}\text{CO}$ ( $J = 1-0$ )					$^{13}\text{CO}$ ( $J = 1-0$ )				
	$l^*$ ( $^{\circ}$ )	$b^*$ ( $^{\circ}$ )	$T_{\text{R}}^*$ (K)	$V_{\text{LSR}}$ ( $\text{km s}^{-1}$ )	$\Delta V$ ( $\text{km s}^{-1}$ )	$l^*$ ( $^{\circ}$ )	$b^*$ ( $^{\circ}$ )	$T_{\text{R}}^*$ (K)	$V_{\text{LSR}}$ ( $\text{km s}^{-1}$ )	$\Delta V$ ( $\text{km s}^{-1}$ )
M009.0–0.2	9.00	−0.20	10.0	26.0	3.1	—	—	—	—	—
M009.1–0.7	9.07	−0.67	3.7	23.2	8.0	—	—	—	—	—
M009.1–0.4	9.13	−0.40	9.5	40.0	9.8	—	—	—	—	—
M009.6+0.2	9.60	+0.20	6.3	3.2	10.7	—	—	—	—	—
M009.7–0.1	9.73	−0.07	6.7	55.0	4.8	—	—	—	—	—
M009.9–0.7	9.87	−0.73	11.5	27.8	10.4	—	—	—	—	—
M010.1–0.3	10.13	−0.33 <sup>†</sup>	9.1	16.4	—	—	—	—	—	—
M010.3–0.1	10.27	−0.13	14.9	13.2	12.2	—	—	—	—	—
M010.3+0.1	10.33	+0.07	6.3	66.0	10.9	—	—	—	—	—
M010.5+0.0	10.47	+0.00	16.6	68.2	12.2	—	—	—	—	—
M010.6–0.3	10.60	−0.33	20.3	−3.2	6.7	—	—	—	—	—
M010.7–0.1	10.67	−0.07	9.1	52.6	4.9	—	—	—	—	—
M010.9+0.0	10.93	+0.00	6.2	20.2	4.3	—	—	—	—	—
M011.1–0.4	11.13	−0.40	11.5	−0.1	10.8	—	—	—	—	—
M011.1+0.1	11.13	+0.07	8.0	12.7	10.4	—	—	—	—	—
M011.2–1.0	11.20	−1.00	8.7	30.6	9.8	—	—	—	—	—
M011.5–1.5	11.47	−1.47	14.4	10.3	4.4	—	—	—	—	—
M011.5+0.1	11.53	+0.07	7.3	52.7	8.8	—	—	—	—	—
M011.9+0.7	11.87	+0.73	9.9	23.2	10.4	—	—	—	—	—
M011.9–0.6	11.93	−0.60	11.6	36.4	13.0	—	—	—	—	—
M011.9–0.1	11.93	−0.13	12.0	41.4	14.3	—	—	—	—	—
M012.0–0.2	12.00	−0.27	8.0	57.9	9.0	—	—	—	—	—

\* N stands for “Non-Detection”.

<sup>†</sup> It is impossible to fit Gaussian distribution because of asymmetry and/or overlapping in the spectrum line. Values given are temperature and peak velocity.

have narrow line widths of less than 2–3  $\text{km s}^{-1}$  (Walsh et al. 1997, 1998; Argon et al. 2000). Therefore, the errors here generally arise from the line widths of the radio recombination line and CO.

#### 4.3. Mass–Luminosity Ratio in the Galactic Center Region

In this subsection, we consider the ratio between the total-mass of molecular clouds in the Galactic-center region and the total infrared-luminosity of IRAS point sources associated with the clouds. The ratio is an indicator of the star-formation activity. The cloud mass is estimated by adopting a distance of 8.5 kpc and an empirical relationship between the molecular-hydrogen column-density and the  $^{12}\text{CO}$  intensity,  $N(\text{H}_2)/W(^{12}\text{CO}) = 7.0 \times 10^{19} \text{ cm}^{-2} (\text{K km s}^{-1})^{-1}$ , in the Galactic center (Torii et al. 2009). Here, we exclude foreground and background disk components and their candidates located within  $\sim 20 \text{ km s}^{-1}$  from the 3-kpc arm and  $V_{\text{LSR}} = 0 \text{ km s}^{-1}$ , as shown in figure 2. We find the total infrared-luminosity,  $8.8 \times 10^6 L_{\odot}$ , and the total molecular mass,  $1.2 \times 10^8 M_{\odot}$ , resulting from the far infrared-luminosity to molecular mass ratio,  $7.5 \times 10^{-2} L_{\odot} M_{\odot}^{-1}$ , in the central kpc. The typical infrared-luminosity to the molecular-mass ratio in nearby giant molecular clouds is  $\sim 0.1 L_{\odot} M_{\odot}^{-1}$  (e.g., Dobashi et al. 2001). We therefore confirm that the star formation in the Galactic center is not particularly active compared with typical giant molecular clouds, as suggested by Morris and Serabyn (1996) and Güsten and Philipp (2004).

#### 5. Results and Discussion on Three Regions W 28, W 30, and W 31

We have chosen three regions (W 28, W 30, and W 31) for a detailed discussion from the present dataset. These are outstanding complexes consisting of massive molecular clouds and bright infrared sources. In the following we give individual descriptions with an emphasis on comparisons with TeV  $\gamma$ -ray sources. TeV  $\gamma$ -ray sources have been detected by the HESS Cherenkov telescope in W 28 and W 30, but no source has been detected in W 31 (Aharonian et al. 2006).

##### 5.1. W 28

The W 28 region along with IC 443 and W 44 is an intriguing example of an SNR associated with a high-mass star-forming region. W 28 is a very bright radio continuum source of more than 300 Jy at 1 GHz, and is composed of several bright SNRs (Green 2004; Brogan et al. 2006). W 28 is located at a relatively small distance of a few kpc, and is one of only several known examples of SNRs interacting with molecular clouds. It is therefore an ideal object to examine how SNRs affect their surrounding molecular gas.

In our analysis, molecular clouds extending by  $1.3 \times 0.3$  in  $l$  and  $b$ , with  $V_{\text{LSR}} \sim 20 \text{ km s}^{-1}$ , seem to delineate the radio boundary of W 28 along its eastern and southern sides (figure 8). Six radio recombination line sources, shown by filled triangles in figure 8, are associated with the molecular

**Table 3.** List of IRAS point source parameters.

CO cloud	IRAS	$F_{12}$ (Jy)	$F_{25}$ (Jy)	$F_{60}$ (Jy)	$F_{100}$ (Jy)	Criteria
M 348.1+0.3	17095–3837	5.48	24.0	306.8	749.2	UCH II
M 348.3–1.0	17149–3916	208.7	987.7	6765	9155	UCH II
M 348.3+0.4	17092–3823	4.7	8.4	<73.1	<3915	
M 348.5+0.1	17111–3824	<4.2	<4.0	60.3	<323.3	
	17110–3823	2.4	<3.2	<60.3	<323.3	
M 348.5–1.0	17158–3901	19.5	98.3	1666	4353	UCH II
M 348.7–1.1	17167–3854	328.4	1818	<9904	35840	
M 349.1+0.1	17130–3756	13.2	49.3	<1558	7109	
M 349.1+0.0	17135–3755	<1.6	16.0	<187.3	<380.2	
M 349.5+0.2	17136–3731	7.6	3.7	<14.3	<351.5	
M 349.6–0.6	17175–3757	<15.8	7.1	<279.3	<631.3	
M 349.7–1.1	17195–3811	<2.9	12.0	123.6	334.8	UCH II
M 349.9–0.5	17178–3742	58.3	329.0	3191	<6880	UCH II
M 350.0–1.3	17216–3801	148.3	410.2	1643	2817	
M 350.1+0.1	17160–3707	45.1	335.5	4246	10440	UCH II
M 350.3+0.1	17166–3656	7.6	78.5	954.1	2083	UCH II
M 350.5–0.4	17190–3705	<3.5	3.25	<42.1	<641.6	
M 350.5+1.0	17136–3617	247.0	2505	10930	13620	UCH II
M 350.7–0.5	17200–3658	5.2	22.9	257.7	533.1	UCH II
M 350.7+0.9	17141–3606	6.5	8.4	235.2	625.4	
M 350.8+0.0	17184–3638	22.2	200.9	1191	1725	UCH II
M 350.8–0.8	17218–3704	<8.4	13.9	419.9	986.8	
M 351.1–0.3	17204–3636	4.9	25.5	508.8	1490	UCH II
M 351.2+0.7	17165–3554	<3.7	805.5	<10510	19830	
M 351.4+0.7	17175–3544	103.5	1400	11360	22050	UCH II
M 351.5+0.2	17197–3552	90.7	519.9	<7204	<11940	
M 351.5–0.5	17221–3619	42.4	244.8	2644	4669	UCH II
M 351.6–1.3	17258–3637	134.3	1688	12750	22320	UCH II
M 351.6–0.3	17220–3609	3.6	41.8	1273	6196	UCH II
M 351.7–1.1	17256–3631	108.5	397.3	3647	10700	UCH II
M 351.8–0.5	17233–3606	4.5	228.8	8787	20400	UCH II
M 352.1+0.7	17192–3510	<1.1	3.6	<125	<527.9	
M 352.3–0.5	17244–3536	7.7	123.3	1232	2637	UCH II
M 352.4–0.1	17231–3520	<19.8	90.6	1386	3067	UCH II
M 352.5+0.8	17199–3446	13.6	127.5	1311	2548	UCH II
M 352.6–1.1	17278–3541	12.2	169.3	1373	2946	UCH II
M 352.6–0.2	17242–3513	48.6	198.5	1767	3630	UCH II
M 352.9–0.2	17249–3501	22.0	118	1095	2620	UCH II
M 353.0+0.5	17228–3430	4.7	19.1	175.4	7396	UCH II
M 353.3–0.2	17262–3435	11.0	142.3	1391	<3377	UCH II
M 353.4–0.3	17271–3439	69.0	589.7	7040	12170	UCH II
M 353.4–0.1	17258–3432	7.4	19.0	<1391	<3377	
M 353.5+0.6	17234–3405	1.8	17.4	196	<432.6	UCH II
M 353.5+0.7	17223–3341	5.6	5.13	<22.44	<324.7	
M 353.7+0.0	17262–3413	2.0	6.1	89.7	<289.5	
M 354.0+0.6	17248–3338	7.4	<9.8	189.8	624.5	
M 354.1–0.1	17279–3350	25.2	166.6	1237	3899	UCH II
M 354.6–0.6	17312–3347	2.2	<4.9	<26.2	<410.9	
M 354.6+0.5	17269–3312	19.2	137.4	1030	1964	UCH II
	17271–3309	43.8	215.2	1048	<1770	UCH II
M 354.7+0.3	17279–3311	8.1	83.3	867	1746	UCH II
M 355.0–0.5	17319–3326	<4.1	21.8	243.1	736.5	UCH II
M 355.1–0.7	17331–3324	4.6	<1.7	<12.2	<201.1	
M 356.1–0.8	17361–3237	1.8	2.11	<28.7	<215.7	
M 356.1+0.7	17299–3146	1.4	<2.8	<22.1	<100.8	
M 356.3+1.1	17286–3126	2.2	2.2	<22.8	<400.7	

**Table 3.** (Continued)

CO cloud	IRAS	$F_{12}$ (Jy)	$F_{25}$ (Jy)	$F_{60}$ (Jy)	$F_{100}$ (Jy)	Criteria
M 356.3–0.1	17335–3206	4.4	24.5	176.2	285.6	UCH II
M 356.5+0.2	17330–3147	3.0	<1.8	<16.9	<227.6	
M 356.5+1.3	17286–3109	<2.6	2.6	<21.6	<424.2	
M 356.7–0.3	17352–3153	<2.4	51.0	491.9	750	UCH II
M 356.8+0.3	17331–3127	4.0	2.3	<16.1	<326.6	
M 357.5+0.2	17356–3054	2.2	<3.6	62.2	427.7	
M 357.5–0.5	17385–3116	9.9	51.6	531.7	1164	UCH II
M 358.4–1.2	17432–3055	1.5	<13.7	<17.2	<390.5	
M 358.4–0.5	17403–3032	7.5	95.2	1530	3526	UCH II
M 358.5–0.4	17402–3025	<6.9	3.5	<131.9	<605.2	
M 358.5–0.4	17404–3019	1.9	<4.4	<131.9	<273.3	
M 358.6–0.1	17392–3008	51.0	368.1	1423	1868	UCH II
M 358.7–0.5	17410–3019	6.7	19.9	255.7	479.1	
M 358.7+0.0	17392–2959	18.3	137.2	662.1	<1512	UCH II
M 358.9–0.5	17416–3003	13.9	9.6	<82.7	<584.1	
M 359.1+0.1	17395–2939	<7.9	<5.5	46.5	<420.6	
M 359.1–0.2	17410–2948	3.9	2.6	<64.0	<2238	
M 359.1–0.1	17408–2942	2.8	3.5	<722.9	<1694	
M 359.4+0.0	17409–2926	11.7	24.5	<712.3	<536.7	
M 359.4+0.1	17409–2923	<7.2	<40.7	712.3	<3589	
M 359.6–0.1	17419–2921	5.2	<44.1	<1233	<5612	
M 359.6–0.1	17416–2916	<112.9	42.9	<11481	<14848	
M 359.6–0.3	17423–2924	4.7	15.9	<362.1	504	
M 359.7–0.1	17418–2914	20.8	153.5	1481	<1378	UCH II
M 359.7+0.1	17413–2909	6.5	<52.4	<606.2	1835	
M 359.7–0.0	17418–2910	11.7	<81.6	681.6	<272	
M 359.9–0.1	17426–2907	<7.9	9.9	<680.2	<715.4	
M 000.3–0.5	17449–2853	7.7	123.3	1232	2637	UCH II
M 000.5+0.1	17429–2832	4.6	<29.4	<592.3	2687	
M 000.5+0.2	17430–2822	8.6	59.5	592.3	2610	UCH II
M 000.5–0.7	17462–2845	4.1	<58.5	<607.2	<1665	
M 000.6–0.9	17470–2853	<42.4	<281.4	5476	13130	
M 000.7+0.6	17415–2801	<9.9	14.3	<150.9	<717.9	
M 000.7–0.0	17441–2822	7.7	68.7	12950	66650	UCH II
M 000.8+0.2	17436–2806	3.0	30.2	450.9	<1031	UCH II
	17436–2807	4.6	<30.2	<450.9	<1255	
M 001.1–0.1	17455–2805	2.9	24.5	270.8	<5393	UCH II
M 001.1–0.1	17455–2800	82.8	468.6	2543	5393	UCH II
M 001.7–0.3	17474–2738	4.3	12.9	<21.86	<775.2	PN
M 002.5–0.0	17484–2647	<4.4	<3.5	151.3	587.6	
M 002.6+0.1	17480–2636	6.2	56.6	565.6	1336	UCH II
M 002.9+0.0	17491–2625	1.9	10.3	154.6	881.4	UCH II
M 003.0–0.1	17495–2624	1.8	8.3	175.4	519.5	UCH II
M 003.3–0.4	17516–2618	1.9	<3.3	<22.9	<263.6	
M 003.3–0.1	17504–2609	<4.0	32.7	<20.5	<1546	PN
M 003.3–0.1	17505–2605	12.8	100.3	1095	<1576	UCH II
M 003.4+0.9	17470–2533	2.3	2.9	36.17	136.2	
M 003.5–0.3	17517–2609	<4.2	29.2	319.3	1063	
M 003.8+0.0	17510–2543	1.6	6.2	75	<522.9	
M 003.9+0.0	17516–2532	4.3	<9.9	<16.7	602.9	
M 004.4+0.1	17522–2504	16.0	132.7	1007	2745	UCH II
M 004.6–0.1	17535–2504	4.7	<8.9	<175.6	<905.7	
M 005.0+0.2	17531–2426	1.7	12.0	72.1	<192.3	UCH II
M 005.3+0.1	17543–2419	<2.9	4.2	<23.6	<192.3	
	17546–2418	2.3	5.3	<35.1	<223	
M 005.5–0.2	17559–2420	24.0	194.3	1051	2170	UCH II

**Table 3.** (Continued)

CO cloud	IRAS	$F_{12}$ (Jy)	$F_{25}$ (Jy)	$F_{60}$ (Jy)	$F_{100}$ (Jy)	Criteria
M 005.7+0.3	17545–2357	11.5	106.6	793.9	1667	UCH II
M 005.9–0.4	17574–2403	198.5	2190	12790	26780	UCH II
M 005.9+0.9	17524–2321	0.8	5.4	<28.4	<112.2	
M 006.0–1.1	18008–2421	<21.4	32.9	<7755	<9036	
M 006.0–1.3	18013–2423	6.9	51.6	<429.6	<1184	
M 006.1–1.5	18018–2426	118.6	288.8	<1611	<2783	
M 006.1–0.6	17588–2358	17.9	50.4	907.1	2324	
M 006.2–0.6	17588–2356	4.7	94.4	<907.1	<2324	
M 006.3–1.1	18009–2007	<49.6	64.6	<513.5	<1307	
	18012–2007	<49.6	<64.6	513.5	1307	
M 006.4–0.5	17588–2340	3.4	53.7	65.2	<304.2	PN
M 006.6–0.1	17577–2320	26.5	149.1	1446	2904	
M 006.6–0.3	17585–2323	2.6	3.3	45.1	<307.7	UCH II
M 007.0–0.3	17594–2303	<4.9	7.7	<26.3	<1242	
M 007.1+0.2	17578–2246	<4.9	15.6	261.4	683.4	
M 007.2–0.5	18010–2259	4.2	5.9	<9.5	<302	
M 007.2+0.2	17582–2234	<4.7	8.2	100.3	<239.5	
M 007.3–0.1	17572–2234	<4.9	<6.1	22.8	<793.8	
M 007.3+0.7	17567–2215	<5.0	<3.9	<294.7	<1203	
M 007.5+0.1	17591–2228	10.0	63.7	962.4	1624	UCH II
M 007.6–0.1	18002–2218	2.3	3.3	<63.9	<189.4	
M 007.7–0.7	18024–2231	6.6	5.5	148.5	380.2	
M 008.0–0.3	18016–2209	2.8	<4.7	<94.3	633.8	
M 008.0–0.1	18011–2206	<4.0	23.2	415.1	1106	
M 008.1–0.0	18009–2155	2.8	11.7	96.7	537.5	UCH II
M 008.2+0.2	17599–2148	59.5	416.8	3325	6969	UCH II
M 008.3–0.1	18016–2148	21.5	17.3	<18.8	<1086	
	18015–2146	3.4	<17.3	<23.4	<302.4	
M 008.4–0.3	18026–2153	25.6	119.2	1296	2311	UCH II
M 008.6–0.3	18032–2137	8.6	153.8	1913	5221	UCH II
M 008.7+0.7	17595–2108	4.2	3.9	<36.5	<559.8	
M 008.8+0.7	17597–2101	1.2	<4.2	<22.7	<588.1	
M 008.9–0.3	18035–2126	8.8	39.3	481.7	1049	UCH II
M 009.0–0.2	18035–2114	6.0	9.6	<20.1	<152.2	
M 009.1–0.7	18052–2125	5.9	3.2	<19.6	<234.9	
M 009.1–0.4	18043–2116	<6.6	6.7	16.6	<236.9	
M 009.6+0.2	18032–2032	38.6	292.4	4106	7844	UCH II
M 009.7–0.1	18045–2033	2.0	<4.0	<19.0	<203.2	
M 009.9–0.7	18073–2046	14.4	82.3	674	2380	UCH II
M 010.1–0.3	18064–2020	404.8	2610	8797	27340	UCH II, PN
M 010.3–0.1	18060–2005	140.4	1042	6027	12010	UCH II
M 010.3+0.07	18052–1958	5.0	3.0	<18.4	<359.4	
M 010.5+0.0	18056–1952	7.9	106.4	3704	10160	UCH II
M 010.6–0.3	18075–1956	<23.5	<148.4	9479	21370	
M 010.7–0.1	18063–1943	<4.5	2.1	<267.9	<580.6	
M 010.9+0.0	18067–1927	7.1	53.4	903.1	1292	UCH II
M 011.1–0.4	18085–1931	10.7	128.7	852.6	2088	UCH II
	18085–1933	2.2	<4.6	<852.6	<656.9	
M 011.1+0.1	18068–1917A	<4.2	5.4	<63.1	<378.1	
M 011.5–1.5	18134–1942	10.3	74.6	767.8	1548	UCH II
M 011.5+0.1	18076–1853	<13.8	132.1	163.7	<89.7	PN
M 011.9+0.7	18060–1816	5.9	42.9	275	1904	UCH II
M 011.9–0.6	18110–1854	13.6	222.1	2082	4930	UCH II
M 011.9–0.1	18094–1840	3.4	14.9	124.3	445.8	UCH II
M 012.0–0.2	18099–1841	2.1	<10.4	158.6	1051	

\* Column (7): UCH II stands for ultra compact H II region and PN for planetary nebula.

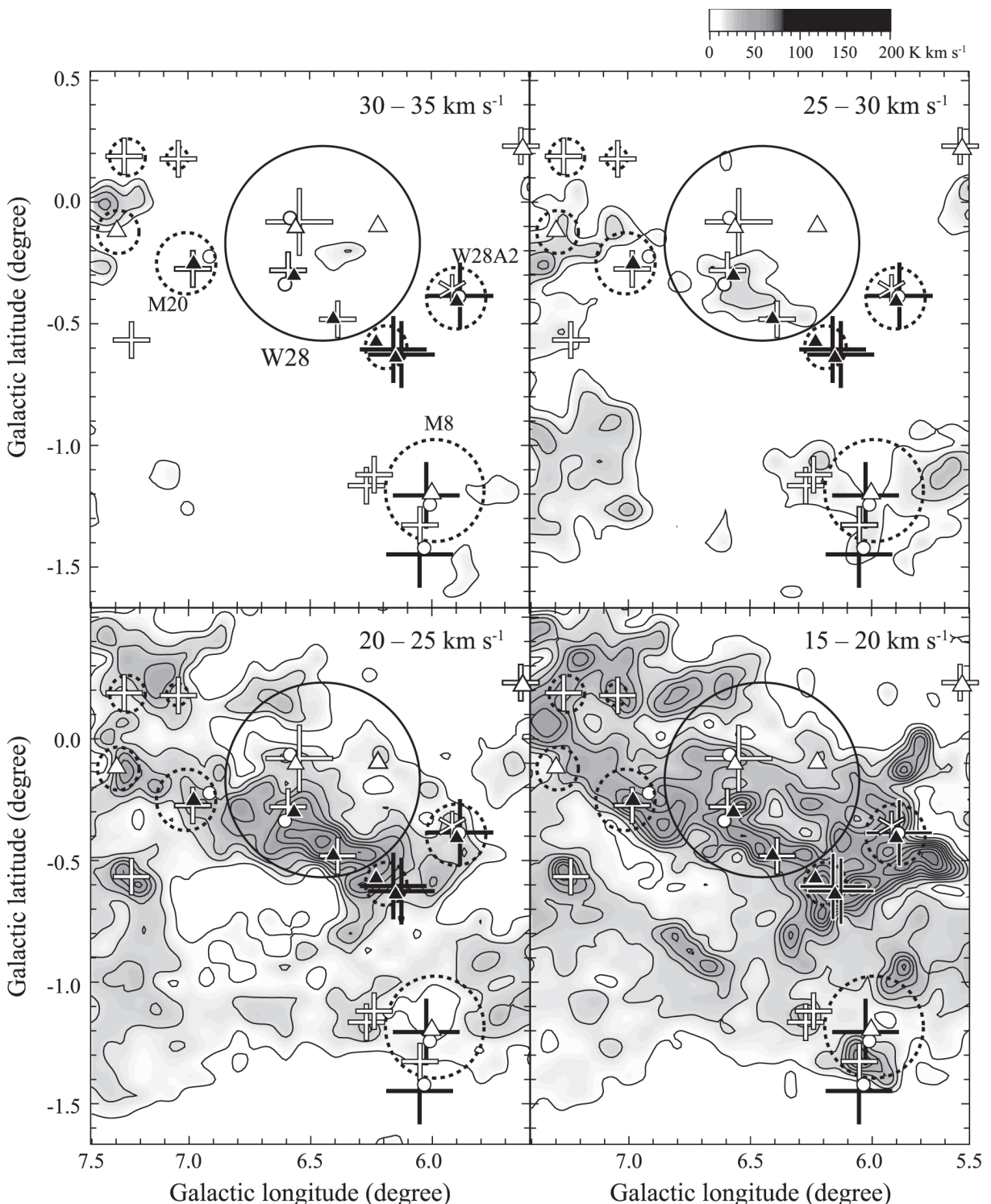


**Fig. 8.** Integrated intensity distributions of  $^{12}\text{CO}$  toward the W 28 region. The integration range is given at the top-right corner in each panel. The contour levels are every  $7\text{ K km s}^{-1}$ , starting from  $10\text{ K km s}^{-1}$ . The thick solid line circle depicts the approximate radio boundary of the SNR W 28 guided by non-thermal radio emission (Brogan et al. 2006). Crosses show IRAS point sources and triangles show atomic hydrogen recombination line sources. Asterisks show maser line sources associated with IRAS point sources. The dashed circles depict the approximate boundaries of thermal radio continuum sources (Altenhoff et al. 1978; Handa et al. 1987). Large crosses are IRAS point sources with  $> 2.0 \times 10^3\text{ Jy}$  in the  $100\mu\text{m}$  band.

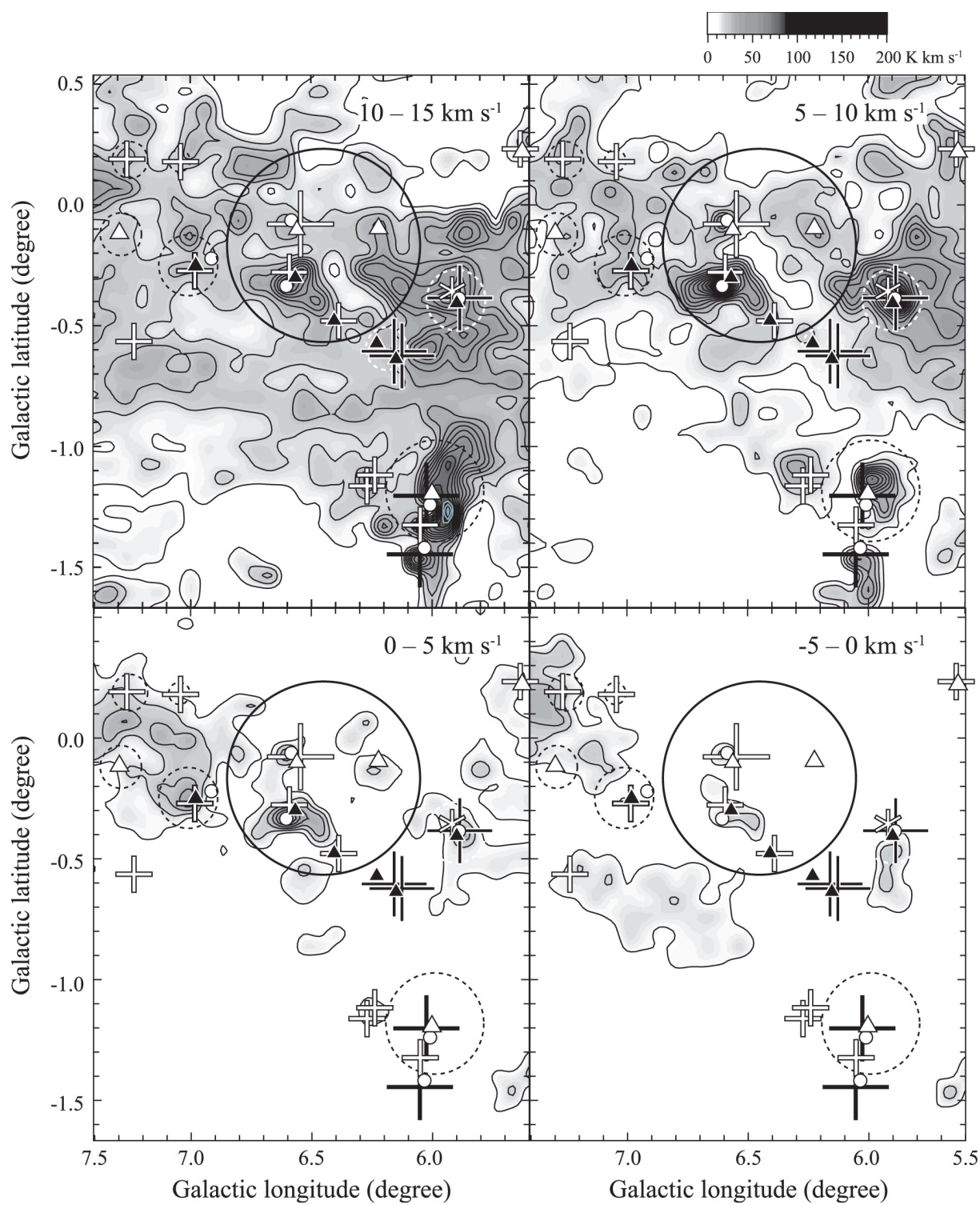
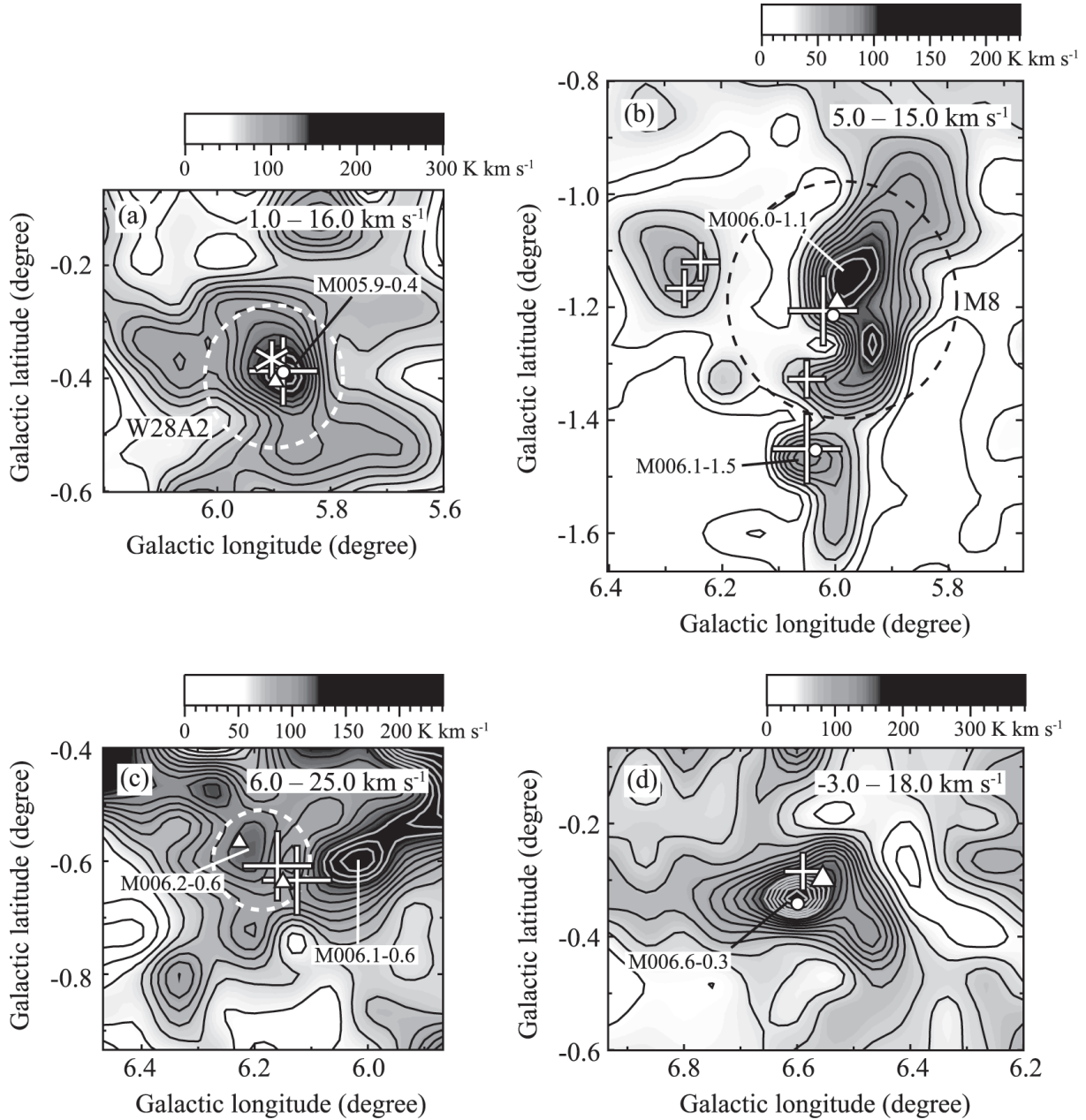


Fig. 8. (Continued)



**Fig. 9.** Integrated intensity distributions of  $^{12}\text{CO}$  toward four selected areas in the W 28 region. The integrated range is given at the upper-right corner in each panel. The contour levels are every  $10\text{ K km s}^{-1}$ , starting from  $30\text{ K km s}^{-1}$  in panel (a). The contour levels are every  $10\text{ K km s}^{-1}$ , starting from  $15\text{ K km s}^{-1}$  in panel (b). The contour levels are every  $8\text{ K km s}^{-1}$ , starting from  $40\text{ K km s}^{-1}$  in panel (c). The contour levels are every  $12\text{ K km s}^{-1}$ , starting from  $25\text{ K km s}^{-1}$  in panel (d). Crosses show IRAS point sources and triangles show atomic hydrogen recombination line sources. Asterisks show maser line sources associated with IRAS point sources. The dashed circles depict the approximate boundaries of thermal radio continuum emission sources (Altenhoff et al. 1978; Handa et al. 1987). Large crosses are IRAS point sources with  $> 2.3 \times 10^3\text{ Jy}$  in the  $100\mu\text{m}$  band.

clouds. Molecular clouds with five associated IRAS point sources with flux densities of over  $2.0 \times 10^3$  Jy in the  $100\mu\text{m}$  band (large black crosses in figure 8) also exist to the east and southeast of W 28. Two of these sources, associated with molecular clouds M 005.9–0.4 (W 28 A2) and M 006.1–1.1 (M 8), respectively, have flux densities of  $2.7 \times 10^4$  Jy and  $9.0 \times 10^3$  Jy in the  $100\mu\text{m}$  band, and it is considered that high-mass star formation is taking place in these molecular clouds. Figure 9 shows four regions [M 005.9–0.4 (a), M 006.0–1.1 and M 006.1–1.5 (b), M 006.1–0.6 and M 006.2–0.6 (c), and M 006.6–0.3 (d)] that present good correlations between CO and IRAS sources. Each panel shows the intensity integrated over the velocity range of the associated  $^{12}\text{CO}$  emission.

A variety of distance estimates have been made by several authors toward W 28 and nearby objects, including the open cluster NGC 6530 (M 8), the Trifid nebula H II region (M 20), and the UCH II region W 28 A2. Sung, Chun, and Bessell (2000) performed UBVRI and H $\alpha$  CCD photometry on the open cluster NGC 6530, and determined the distance modulus of the cluster as being  $m - M = 11.25$  mag ( $\pm 0.1$ ) corresponding to 1.7–1.9 kpc. Lynds, Canzian, and O’Neil (1985) examined the optical depth of the dust toward the Trifid nebula using the H $\beta$  line at 4693Å, and found the distance of the nebula to be 1.7 kpc. Acord, Churchwell, and Wood (1998) noted that the ionized shell in the UCH II region W 28 A2 is expanding. They estimated its expansion velocity and a source distance of 1.6–2.7 kpc. Goudis (1976) derived a distance of 1.6 kpc to the W 28 SNR according to the surface brightness–linear diameter relation (Milne 1970) at 1 GHz. Considering these observational results, we adopt a distance of 2.0 kpc to W 28.

For the mass estimation, we used the above distance and a conversion factor of  $2.0 \times 10^{20} \text{ cm}^{-2} (\text{K km s}^{-1})^{-1}$  in the Galactic disk (Bertsch et al. 1993). The range of mass of each of the  $^{12}\text{CO}$  clouds is  $0.2\text{--}0.6 \times 10^5 M_\odot$  in W 28.

Feedback in the form of supernovae (SNe) and stellar winds, as well as UV photons, plays an important role in star formation. Regions of high mass star formation located to the east of W 28 emit strongly in X-rays (e.g., M 20), bipolar outflow is located to the west of the UCH II region W 28 A2, and broad molecular line emission originating from the SNR shock is detected (e.g., Arikawa et al. 1999).

Through an extensive comparison between HESS TeV  $\gamma$ -ray and NANTEX CO dataset, Aharonian et al. (2008) have discovered that four TeV  $\gamma$ -ray sources in W 28 are well correlated with the molecular clouds. The TeV  $\gamma$ -rays are produced either by the inverse Compton effects of cosmic-ray electrons or protonic collisions followed by neutral pion decay. The  $\gamma$ -ray features are noted as A to D, and their  $^{13}\text{CO}$  distributions are shown in figure 10. This strongly suggests that highly energetic events, like powerful stellar winds or SNe, are taking place in or around the molecular clouds, leading to the acceleration of high-energy cosmic rays.

We show the  $^{13}\text{CO}$  distribution in figure 10, and a  $^{13}\text{CO}$  longitude–velocity diagram in figure 11. Since the  $^{13}\text{CO}$  emission has a smaller optical depth than  $^{12}\text{CO}$ , these figures indicate more clearly than  $^{12}\text{CO}$  the distribution of the molecular column density. Figure 12 shows close-ups of the four regions, A–D. These detailed comparisons of  $^{13}\text{CO}$  and  $\gamma$ -rays

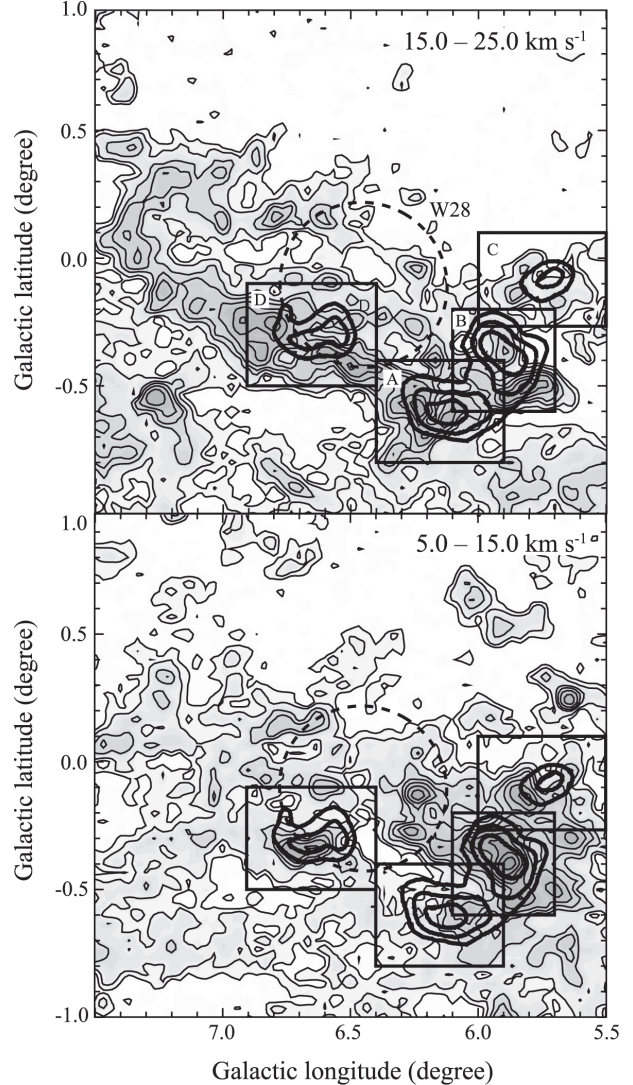


**Fig. 10.**  $^{13}\text{CO}$  distributions of the W 28 region (thin contours) overlaid with HESS TeV  $\gamma$ -ray emission (thick contours), showing the close relationship between the low (molecular) and high ( $\gamma$ -ray) energy environments. The dashed line illustrates the extent of the SNR.

are interesting because of an even tighter correlation:  $\gamma$ -ray sources A and C appear to be located toward “holes” in the molecular gas, while B and D have peaks coincident with the molecular peaks. We note that these correlations are the most striking in the entirety of the datasets, which covers an extensive region along the Galactic plane, from  $l = -40^\circ$  to  $+40^\circ$  and  $b = -1^\circ$  to  $+1^\circ$ .

## 5.2. W 30

W 30 is an extended radio source with an angular size of about 50', and is identified as an SNR by Odegard (1986) at 57 MHz. Kassim and Weiler (1990) decomposed the radio continuum emission into non-thermal and thermal components by using VLA 20 cm and 90 cm wavelength data. Lockman (1989) also carried out observations toward the sources, and detected recombination line sources at 8 positions. W 30 is thus a complex of an SNR and H II regions.

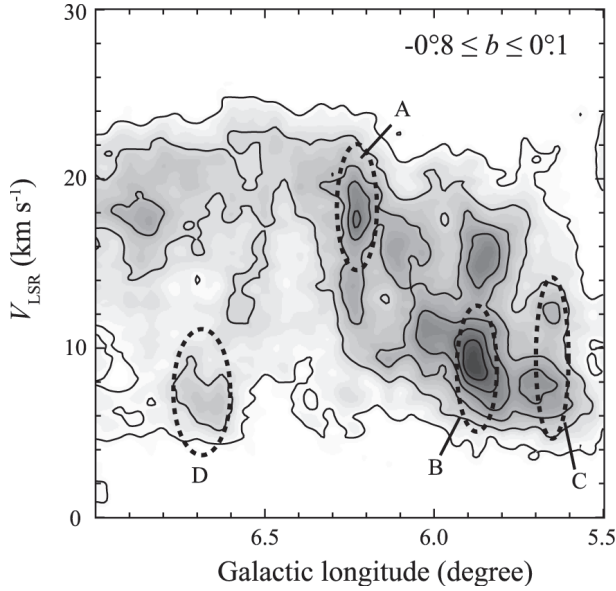


**Fig. 11.** Position–velocity diagram in galactic longitude of the  $^{13}\text{CO}$  emission across the  $\gamma$ -ray emitting region in W 28, illustrating the broad line width of more than  $10 \text{ km s}^{-1}$ . Labels A, B, C, and D refer to the four boxes shown in figure 10. Contours are every  $0.35 \text{ K degree}$ .

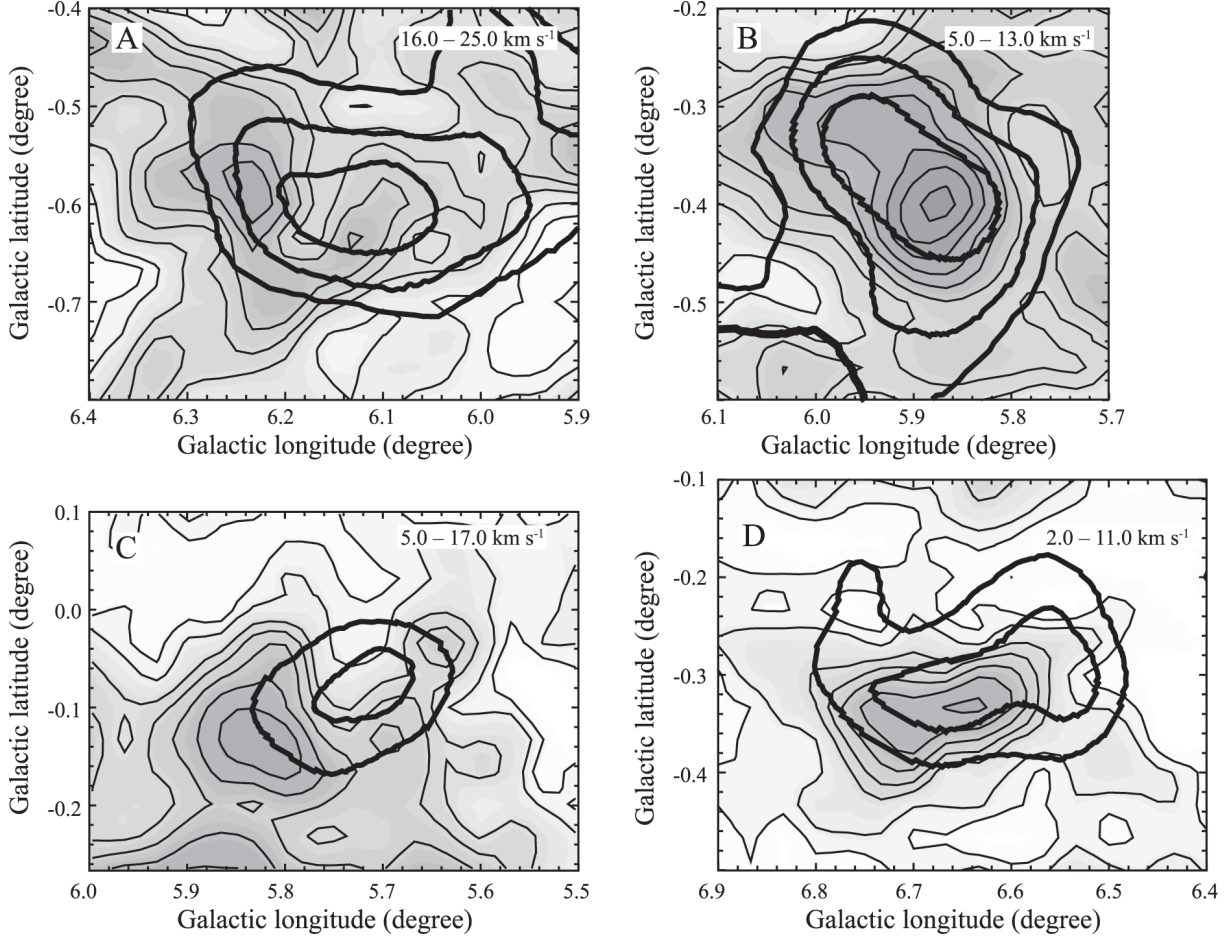


**Fig. 12.** Enlargements of the four boxes in figure 10 that show the  $\gamma$ -ray distribution overlaid on the  $^{13}\text{CO}$  distribution. Note that at positions A and C the  $\gamma$ -ray peak is located at holes of the molecular distribution, whereas at positions B and D the peaks are coincident.

We show velocity channel maps every  $5 \text{ km s}^{-1}$  in figure 13. The molecular clouds may be decomposed roughly into two velocity components with a velocity range from 30 to  $45 \text{ km s}^{-1}$  (hereafter the  $38 \text{ km s}^{-1}$  clouds) and from 12 to  $25 \text{ km s}^{-1}$  (hereafter the  $19 \text{ km s}^{-1}$  clouds). In particular, the  $38 \text{ km s}^{-1}$  clouds have an elongated structure, with an angular size of  $\sim 1^\circ \times 0.4^\circ$  (figure 14). These distributions show good correlations with H II regions, as shown in figure 15, where the MSX infrared data are superposed.

As a result of our analysis, it is found that eight IRAS point sources (shown by black crosses in figure 13) are associated with the molecular clouds. Indeed, IRAS 18026–2153, 18032–2137, and 18035–2126, which satisfy the color criteria of Wood and Churchwell (1989) show a good correlation with the  $38 \text{ km s}^{-1}$  molecular cloud. IRAS 18032–2137 has a large flux density of more than  $5 \times 10^3 \text{ Jy}$  in the  $100 \mu\text{m}$  band, and is associated with a number of maser sources. The IRAS 17599–2148 point source of more than  $7 \times 10^3 \text{ Jy}$  in the  $100 \mu\text{m}$  band is associated with the  $19 \text{ km s}^{-1}$  clouds. This also satisfies the color criteria of Wood and Churchwell (1989). These observations indicate that active star formation is occurring in W 30. Broad CO line emission, which suggests interactions between the molecular clouds and the SNR, is not detected in either the  $19 \text{ km s}^{-1}$  or the  $38 \text{ km s}^{-1}$  molecular

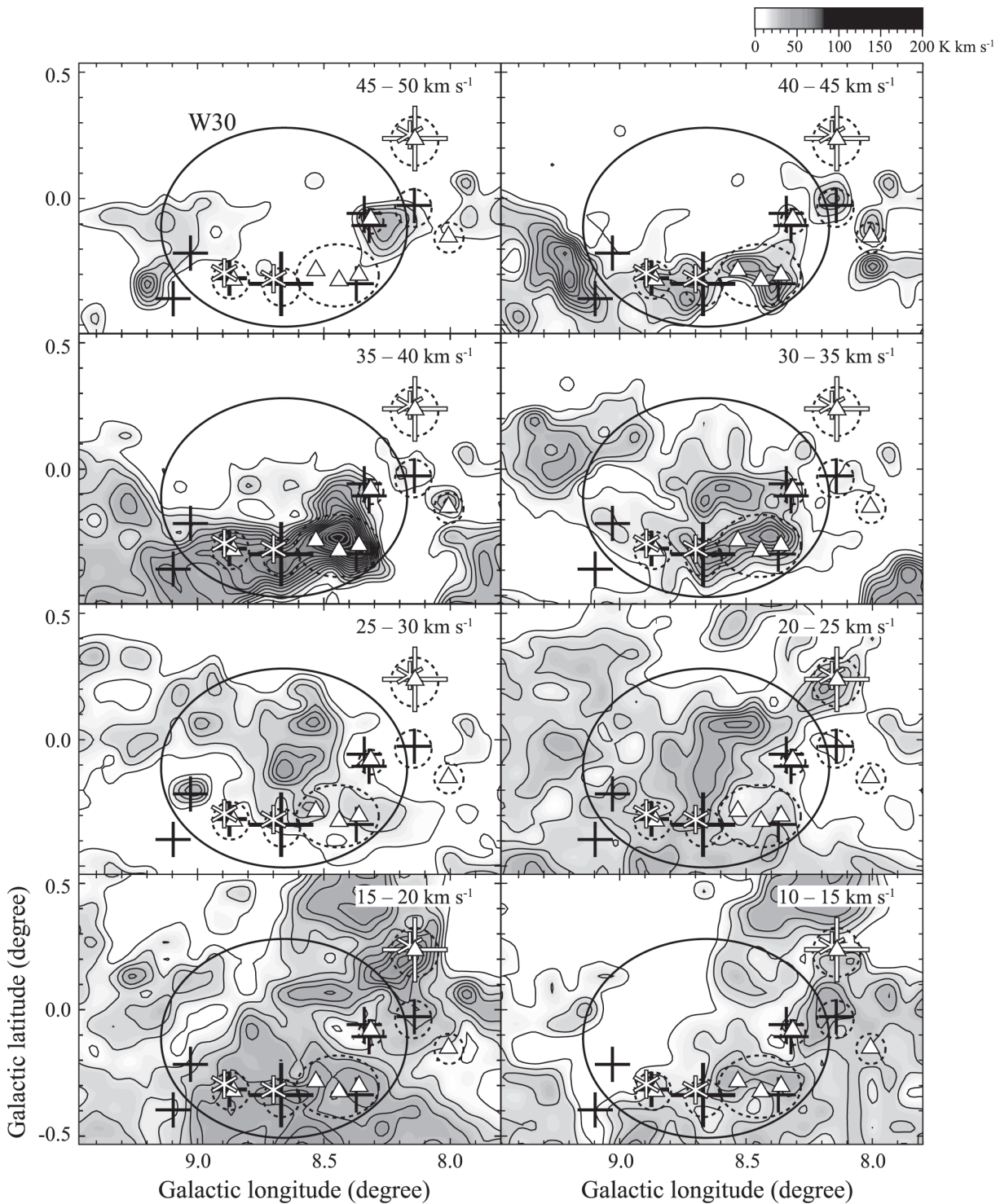


**Fig. 13.** Integrated intensity distributions of  $^{12}\text{CO}$  toward the W 30 region. The integrated velocity range is given at the upper-right corner in each panel. The contour levels are every  $6 \text{ K km s}^{-1}$ , starting from  $10 \text{ K km s}^{-1}$ . The thick solid circles depict the approximate radio boundary of the SNR W 30 guided predominantly by the non-thermal emission (Brogan et al. 2006). Crosses show IRAS point sources and triangles show atomic hydrogen recombination line sources. Asterisks show maser line sources associated with IRAS point sources. The dashed circles depict the approximate boundaries of thermal radio continuum emission sources (Altenhoff et al. 1978; Handa et al. 1987). Large crosses are IRAS point sources with  $\geq 5 \times 10^3 \text{ Jy}$  in the  $100 \mu\text{m}$  band.

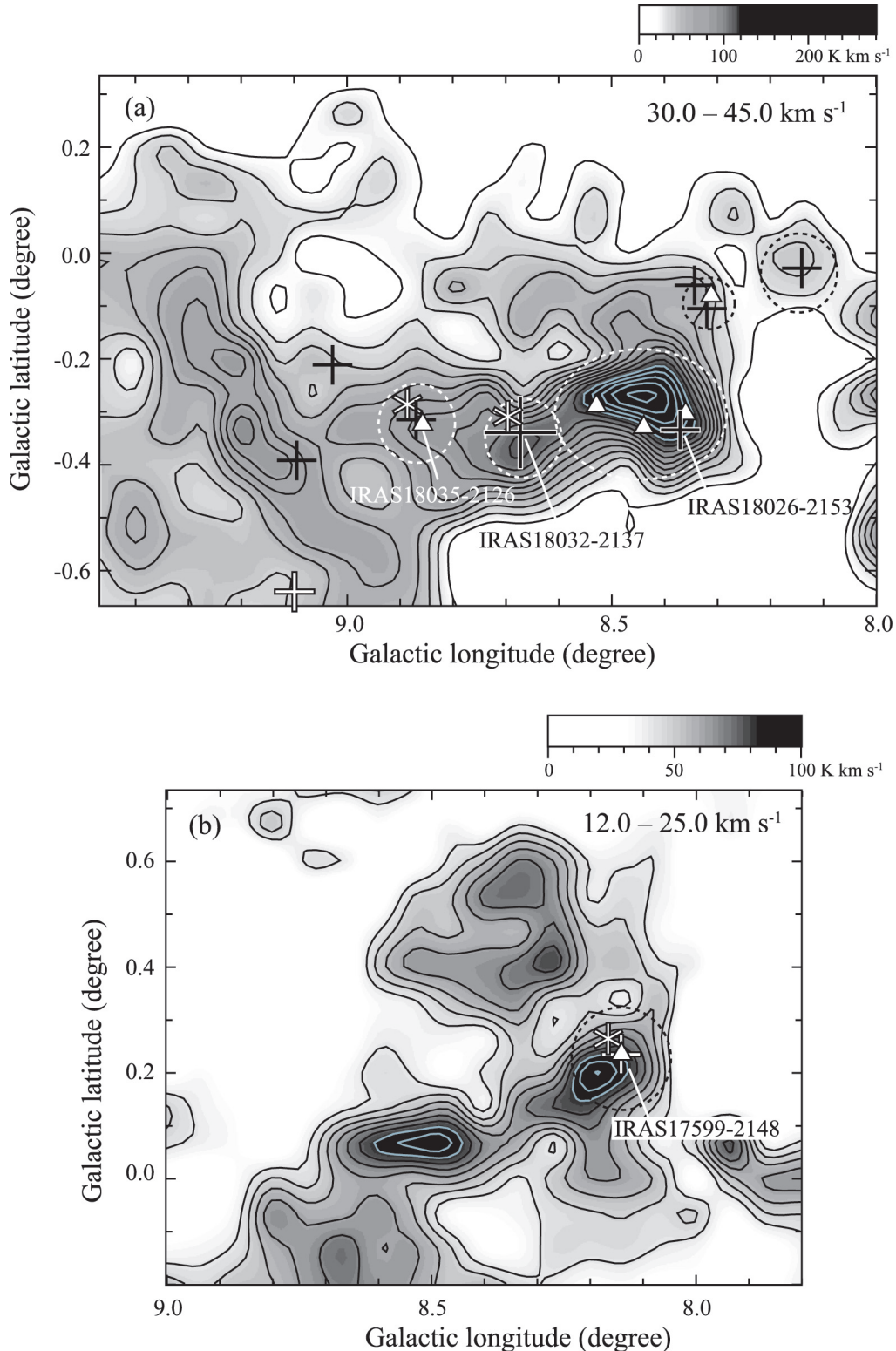


**Fig. 14.** Integrated intensity distributions of  $^{12}\text{CO}$  toward the W 30 region. The integrated range is given at the upper-right corner in each panel. The contour levels are every 10  $\text{K km s}^{-1}$ , starting from 20  $\text{K km s}^{-1}$  in the upper panel. The contour levels are every 7  $\text{K km s}^{-1}$ , starting from 30  $\text{K km s}^{-1}$  in the lower panel. Crosses show IRAS point sources and triangles show atomic hydrogen recombination line sources. Asterisks show maser line sources associated with IRAS point sources. The dashed circles depict the approximate boundaries of thermal radio continuum emission sources (Altenhoff et al. 1978; Handa et al. 1987). Large crosses are IRAS point sources with  $\geq 5 \times 10^3 \text{ Jy}$  in the  $100 \mu\text{m}$  band.

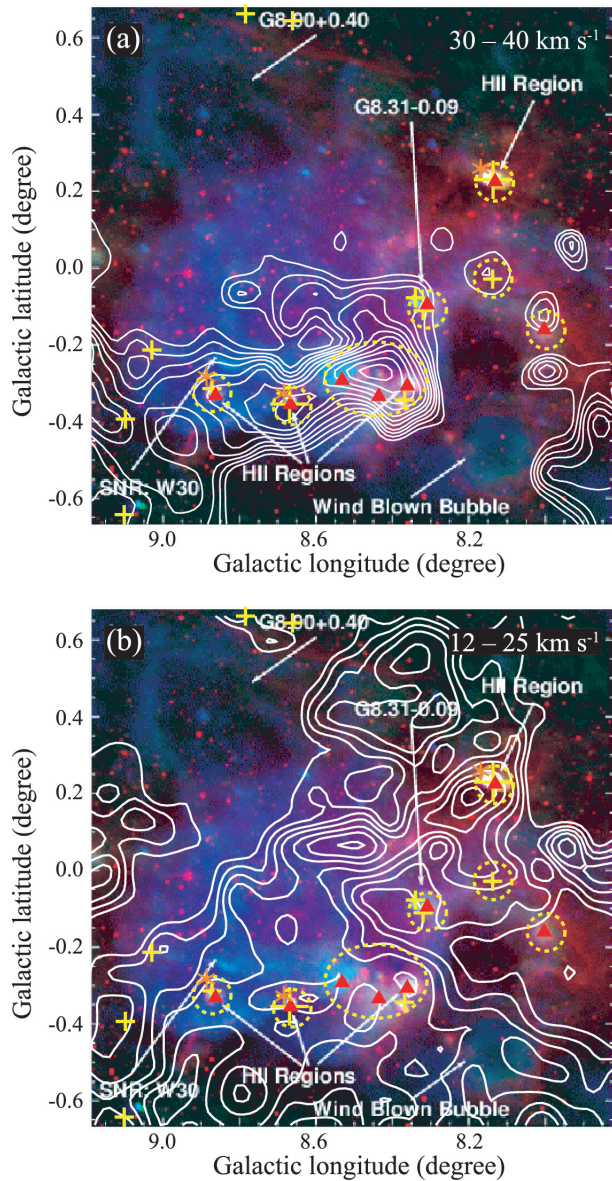


**Fig. 15.**  $^{12}\text{CO}$  distributions of the W 30 region (thick contours) overlaid on three-color images of VLA 90 cm (blue), MSX 8  $\mu\text{m}$  (red), and SGPS + VLA 20 cm (green) data (Brogan et al. 2006). The contour levels are 35, 43, 51, 59, 70, 80, 91, 107, 121, 139, and 155 K  $\text{km s}^{-1}$ . The integrated velocity range is given at the top-right corner in each panel. Crosses show IRAS point sources and triangles show atomic hydrogen recombination line sources. Asterisks show maser line sources associated with IRAS point sources. The dashed circles depict the approximate boundaries of thermal radio continuum emission sources (Altenhoff et al. 1978; Handa et al. 1987). Large crosses are IRAS point sources with  $\geq 5 \times 10^3$  Jy in the 100  $\mu\text{m}$  band.

clouds. The SNR may be in the same direction by chance.

Downes et al. (1980) derived a kinematic distance of 5.1 kpc for the W 30 complex by using the hydrogen recombination line H110 $\alpha$  combined with complementary H<sub>2</sub>CO absorption line observations. The CO radial velocity of the W 30 complex is around 38  $\text{km s}^{-1}$ . Using this velocity, the kinematic distance is estimated to be 4.9 kpc by assuming a flat rotation curve (Brand & Blitz 1993). We shall adopt a distance of 5.0 kpc

for W 30. We estimate the total molecular mass to be 2.1–3.1  $\times 10^5 M_{\odot}$  in W 30 for the same X factor with that used in W 28.

W 30 shows ROSAT soft-X ray emission in its western part SNR G8.7–0.1, and a pulsar PSR J1803–2137 is detected in the central region (Finley & Ögelman 1994). The TeV  $\gamma$ -ray source (figure 16), with a size of approximately 20', is the largest of the emission regions of the inner Galactic Plane Scan datasets (Aharonian et al. 2005, 2006). Towards this region we have found that the CO emission shows good correlation with the peak of the TeV  $\gamma$ -ray source, as shown in the two channel maps in figure 16; the TeV  $\gamma$ -ray source shows an upside-down ‘L’-shape, consisting of the peak elongated in the east–west direction and a ridge extending toward the south at  $l \sim 8^{\circ}4$ . The former component appears to agree with the 19.0  $\text{km s}^{-1}$  CO peak, and the latter with part of the 38.0  $\text{km s}^{-1}$  CO emission. We suggest that the complicated shape of the TeV  $\gamma$ -ray emission does not necessarily require a single molecular cloud. This is a second region showing such a good correlation subsequent to W 28. It is particularly interesting that the young Vela-like pulsar PSR J1803–2137 with a spin-down age of 16000 yr (Kassim & Weiler 1990) is located near the molecular gas, suggesting a possible interaction between the pulsar wind and the molecular gas. In fact,  $\gtrsim 30\%$  of the HESS sources are identified as pulsar wind nebulae (Aharonian et al. 2006). The distance of the pulsar is determined from dispersion measures to be 3.84 kpc (Brisken et al. 2006) and 5.3 kpc (Clifton & Lyne 1986). Given the overall uncertainties involved, we suggest that the pulsar may be associated with at least the northern part of the molecular gas closer to the pulsar. At such a distance, the spin-down luminosity corresponds to  $\sim 3\%$  of the observed  $\gamma$ -ray emission, as noted by Aharonian et al. (2006). The present finding concerning the molecular gas offers a viable alternative to the previous suggestion by Aharonian et al. (2006), that SNR G8.7–0.1 may be responsible for  $\gamma$ -ray production.

### 5.3. W 31

W 31 mainly consists of three HII-molecular cloud complexes [G10.2–0.3, G10.3–0.1, and G10.6–0.4 (Shaver & Goss 1970)], and is located in the Galactic plane at  $l \sim 10^{\circ}$  and  $b \sim 0^{\circ}$ , with an angular size of 25'  $\times$  30' in  $l$  and  $b$  in figure 17. The distribution of the  $^{12}\text{CO}$  emission of the corresponding velocity range is shown in the five panels of figure 18: a, M 010.1–0.3 and M 010.3–0.1; b, M 010.5+0.0; c, M 010.6–0.3; d, M 011.1–0.4; and e, M 010.7–0.1. The three complexes correspond to M 010.1–0.3, M 010.3–0.1, M 010.6–0.3, respectively (figures 18a and 18c). The molecular distribution is rather clumpy, consisting of several distinct molecular features. Past observations of H I absorption toward W 31 suggest that it is probably located in the inner expanding arm (Wilson 1974; Kalberla et al. 1982; Corbel et al. 1997; Corbel & Eikenberry 2004).

Ghosh et al. (1989) suggested the possibility that a bipolar outflow exists toward G10.2–0.3, based on the detection of a red- and blue-shifted velocity in the CO line (Whiteoak et al. 1982). Kim and Koo (2002) also discussed the existence of bipolar outflows for both G10.2–0.3 and G10.3–0.1, noting that the extended envelope of G10.3–0.1 has a bipolar morphology. In addition, Blum, Damineli, and Conti (2001)

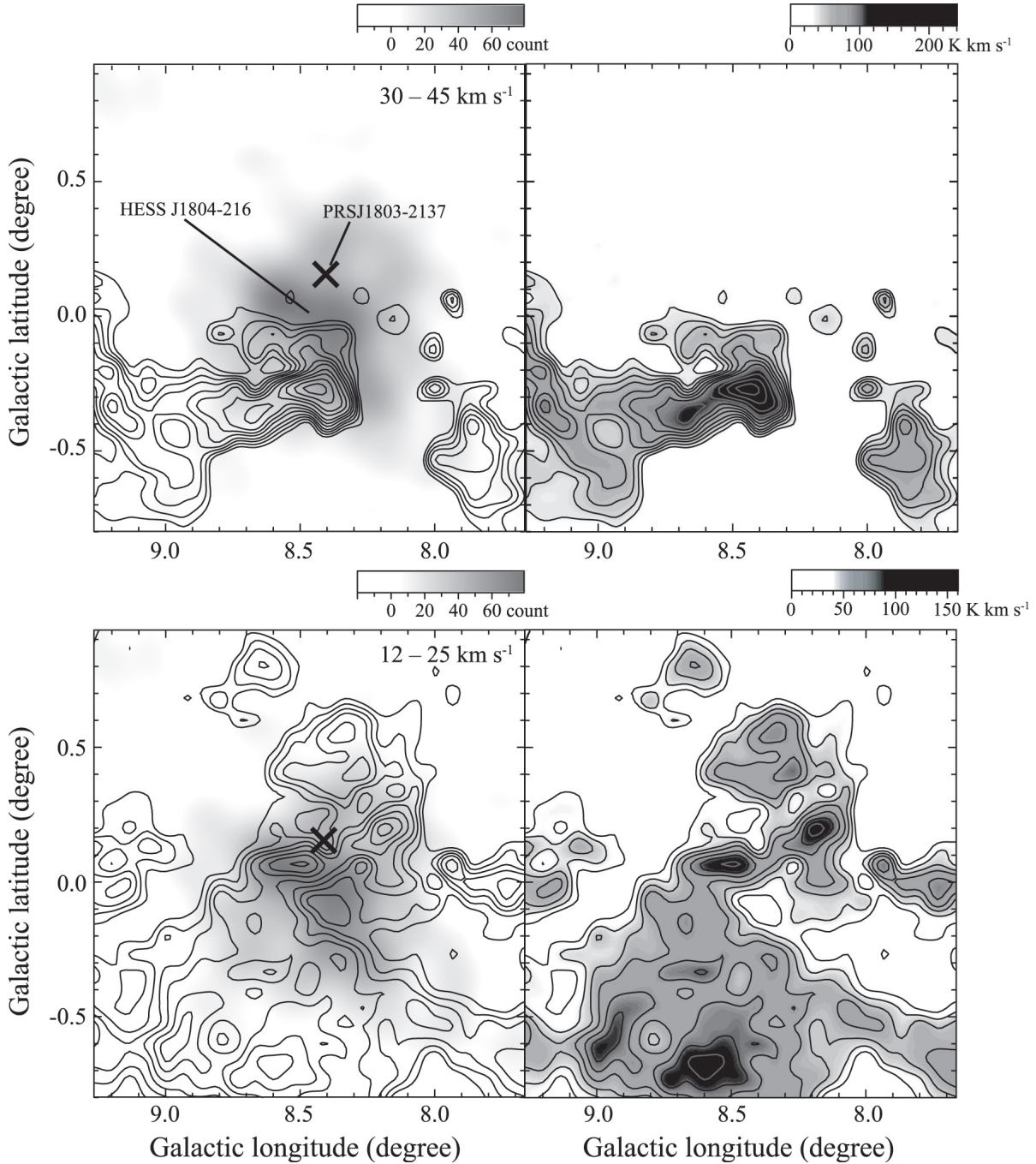


**Fig. 16.** (Upper left):  $^{12}\text{CO}$  distribution in a velocity range  $30.0 - 45.0 \text{ km s}^{-1}$  of the W 30 region (contours) overlaid on the HESS TeV  $\gamma$ -ray distribution (grayscale image: Aharonian et al. 2005, 2006), showing close correlation between the molecular gas and the lower part of the  $\gamma$ -ray distribution. (Upper right): Integrated intensity distribution of  $^{12}\text{CO}$  in the same velocity range (gray scale). The contour levels are 35, 43, 51, 59, 70, 80, 91, 107, 121, 139 and 155  $\text{K km s}^{-1}$ . (Lower left):  $^{12}\text{CO}$  distribution in a velocity range  $12.5 - 25.0 \text{ km s}^{-1}$  of the W 30 region (contours) overlaid on the HESS TeV  $\gamma$ -ray distribution (grayscale image: Aharonian et al. 2005, 2006), showing close correlation between the molecular gas and the upper part of the  $\gamma$ -ray distribution. (Lower right): Integrated intensity distribution of  $^{12}\text{CO}$  in the same velocity range (gray scale). Contour levels are the same with upper right.

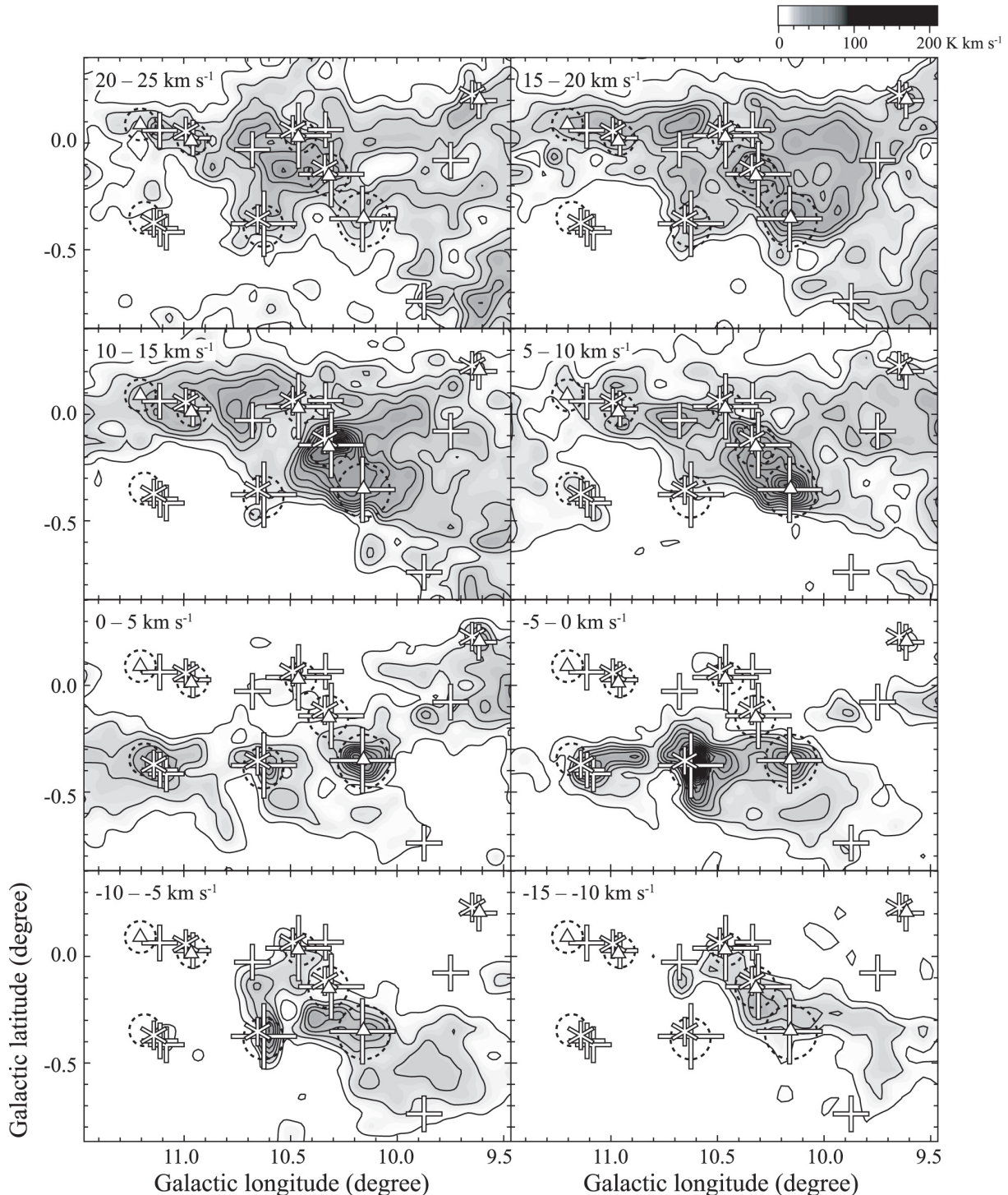


**Fig. 17.** Integrated intensity distributions of  $^{12}\text{CO}$  in a velocity range  $-15.0$ – $25.0 \text{ km s}^{-1}$  toward the W 31 region. The integration range is given at the upper-left corner in each panel. The contour levels are every  $6 \text{ K km s}^{-1}$ , starting from  $10 \text{ K km s}^{-1}$ . Crosses show IRAS point sources and triangles show atomic hydrogen recombination line sources. Asterisks show maser line sources associated with IRAS point sources. The dashed circles depict the approximate boundaries of thermal radio continuum emission sources (Altenhoff et al. 1978; Handa et al. 1987). Large crosses are IRAS point sources with more than  $10^4$  Jy in the  $100 \mu\text{m}$  band.

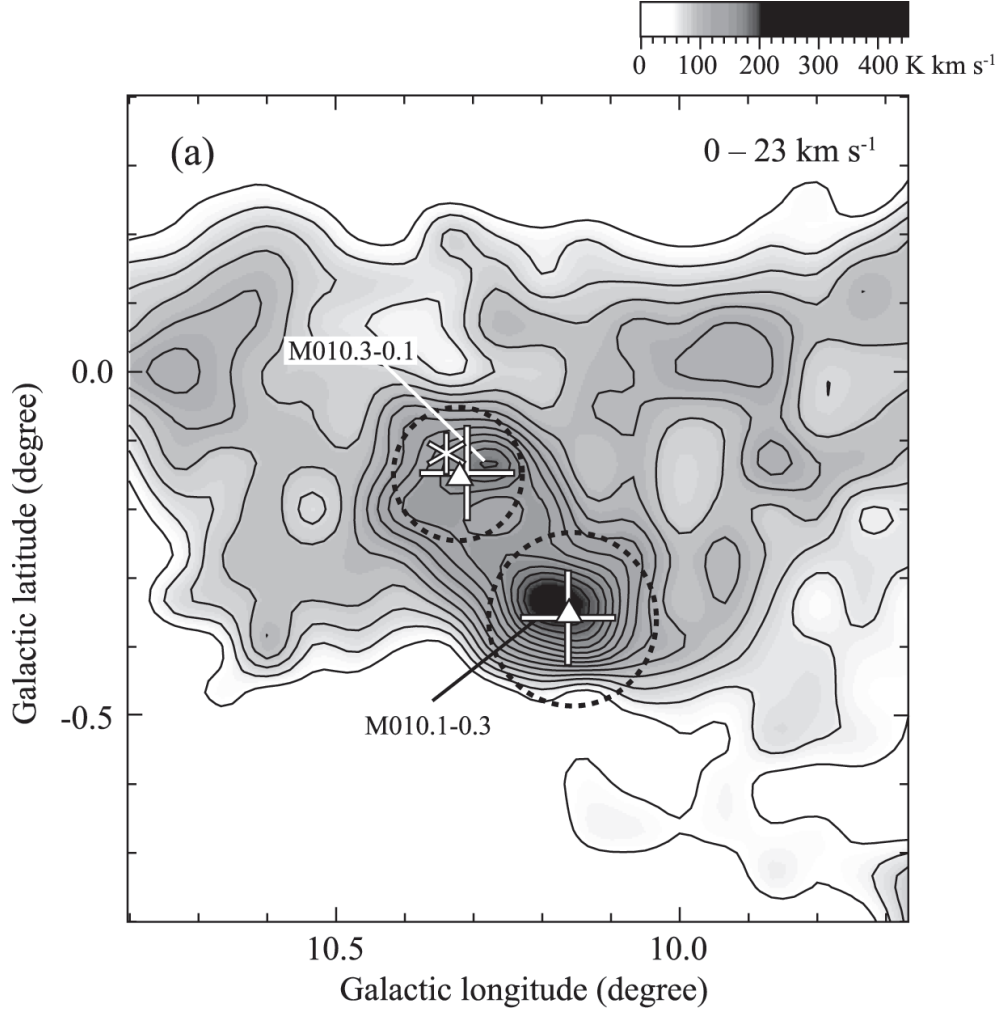


**Fig. 18.** Integrated intensity distributions of  $^{12}\text{CO}$  toward five selected areas in the W 31 region. The integration range in velocity, tuned so as to represent physically connected features, is given at the upper-right corner in each panel. (a) Contour levels are every  $12 \text{ K km s}^{-1}$ , starting from  $50 \text{ K km s}^{-1}$ . (b) Contour levels are every  $12 \text{ K km s}^{-1}$ , starting from  $20 \text{ K km s}^{-1}$ . (c) Contour levels are every  $11 \text{ K km s}^{-1}$ , starting from  $30 \text{ K km s}^{-1}$ . (d) Contour levels are every  $5 \text{ K km s}^{-1}$ , starting from  $15 \text{ K km s}^{-1}$ . (e) Contour levels are every  $6 \text{ K km s}^{-1}$ , starting from  $35 \text{ K km s}^{-1}$ . Crosses show IRAS point sources and triangles show atomic hydrogen recombination line sources. Asterisks show maser line sources associated with IRAS point sources. Dashed circles show radio continuum boundaries (see figure 17). Large crosses are IRAS point sources with more than  $10^4 \text{ Jy}$  in the  $100 \mu\text{m}$  band.

estimated the age of O-type stars in W 31 to be less than one million years using spectroscopic and photometric data. Each IRAS point source associated with the molecular clouds of G10.2–0.3 and G10.3–0.1 in our catalog has large flux density of more than  $10^4 \text{ Jy}$  in the  $100 \mu\text{m}$  band, and satisfies the color criteria of Wood and Churchwell (1989). This indicates that the H II regions G10.2–0.3 and G10.3–0.1 are young, and that active star formation is occurring there. In W 31 there is also one more molecular cloud, M 010.5+0.0, different from the upper three objects, which is associated with radio recombination line sources, methanol maser sources, and IRAS point sources with large flux densities, respectively (figure 18b).

In the present observations, the W 31 complexes, M 010.1–0.3, M 010.3–0.1, and M 010.6–0.3, have radial velocities of  $16.4$ ,  $13.2$ , and  $-3.2 \text{ km s}^{-1}$ , respectively. The former two velocities correspond to a kinematic distance of around  $2 \text{ kpc}$  while a negative velocity is forbidden, suggesting

being dominated by random motion. Blum, Damineli, and Conti (2001) performed near-infrared spectroscopy and photometry toward stellar clusters in the three regions. They derived a spectro-photometric distance for W 31 by assuming either ZAMS or dwarf luminosity classes for the stars of the cluster, obtaining distances of  $3.1 \text{ kpc}$  and  $3.7 \text{ kpc}$ , respectively. We shall thus tentatively infer  $3.4 \text{ kpc}$  as the distance of W 31, while more detailed observations are highly desirable to have a better estimate of the distance.

## 6. Summary

In order to better understand the molecular clouds and their properties toward the Galactic center region of  $72$  square degrees, we have analyzed a database of  $^{12}\text{CO}$  ( $J = 1-0$ ) and  $^{13}\text{CO}$  ( $J = 1-0$ ) obtained by the NANTEN millimeter-wave telescope to search for associations with objects including

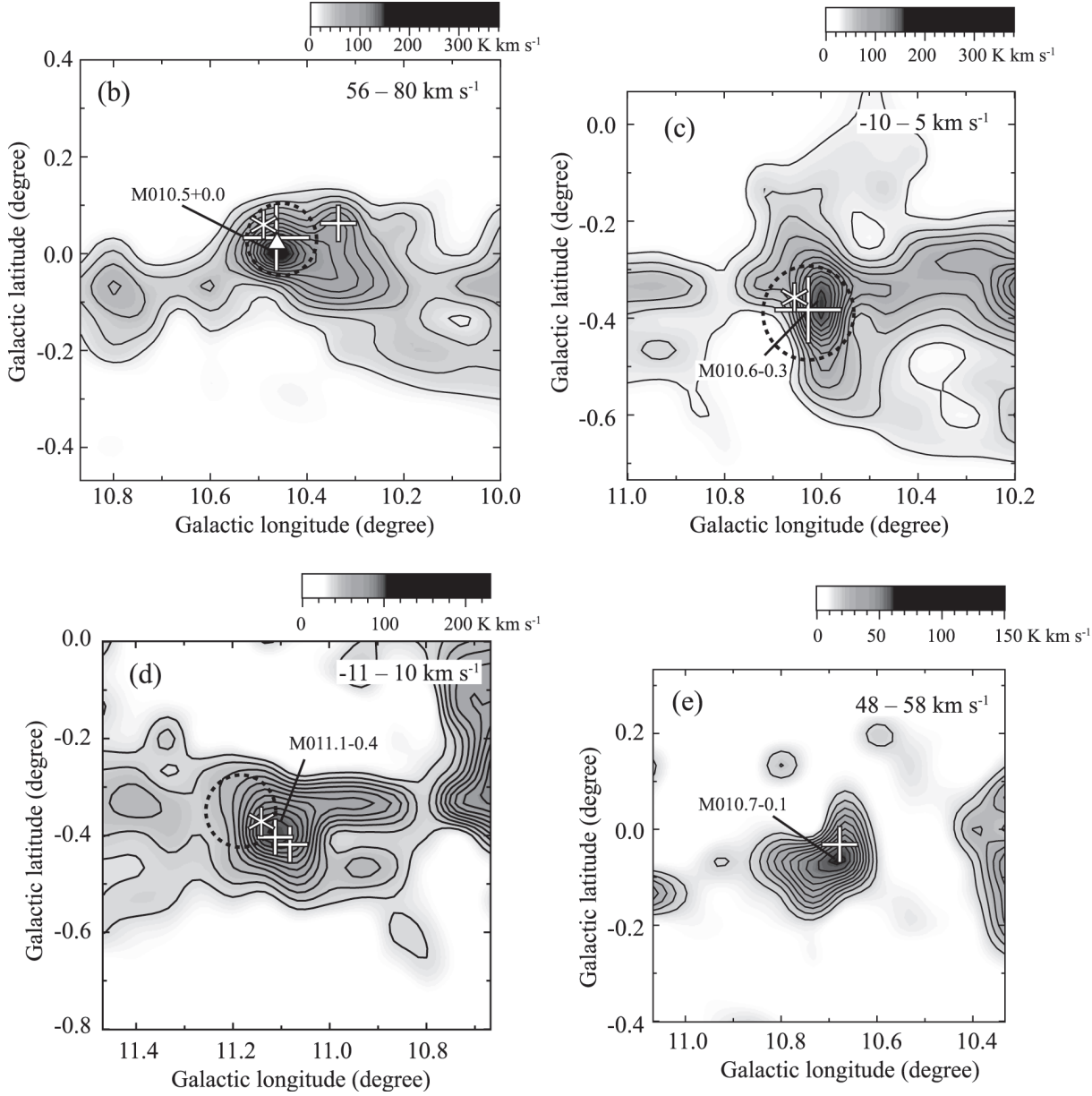


Fig. 18. Continued.

IRAS point sources, radio recombination line sources, maser-line sources, other molecular line sources, and radio continuum sources. The main points of the work are summarized below:

(1) We have identified 167 IRAS point sources, 73 recombination line sources, 58 maser sources, 107 radio continuum sources, and 77 molecular line sources associated with 169 positions of the CO emission. We infer that  $\sim 70\%$  of the identifications with the CO emission are reliable, thanks to velocity information of the other spectral line data. We have compiled the data of comparisons in a table for future utilizations at various wavelengths.

(2) We confirm that the star formation in the Galactic center is not particularly active compared with typical giant molecular clouds, as indicated by the far infrared-luminosity to molecular mass ratio  $5.8 \times 10^{-2} L_{\odot} M_{\odot}^{-1}$  in the central kpc.

(3) We present detailed CO distributions for the three outstanding regions of active star formation with SNRs, i.e., W 28, W 30, and W 31. Among them, we show that the W 28 and W 30 regions show a good correlation with TeV  $\gamma$ -ray sources.

(4) The W 30 region indicates a remarkable correlation between the molecular emission and TeV  $\gamma$ -rays. We suggest that a pulsar, PRS J1803–2137, close to the molecular gas may play a role in accelerating cosmic rays, leading to  $\gamma$ -ray production either by protonic or leptonic origins.

The NANTEN project is based on a mutual agreement between Nagoya University and the Carnegie Institution of Washington (CIW). We greatly appreciate the hospitality of all the staff members of the Las Campanas Observatory of

CIW. We are thankful to many Japanese public donors and companies who contributed to realizing the project. This study has made use of SIMBAD Astronomical Database and NASA's Astrophysics Data System Bibliographic Services. This work is financially supported in part by a Grant-in-Aid for

Scientific Research from the Ministry of Education, Culture, Sports, Science and Technology of Japan (No. 15071203) and from JSPS (No. 14102003, Core-to-core program 17004, and No. 18684003)

## References

- Acord, J. M., Churchwell, E., & Wood, D. O. S. 1998, *ApJ*, 495, L107  
 Aharonian, F., et al. 2005, *Science*, 307, 1938  
 Aharonian, F., et al. 2006, *ApJ*, 636, 777  
 Aharonian, F., et al. 2008, *A&A*, 481, 401  
 Altenhoff, W. J., Downes, D., Pauls, T., & Schraml, J. 1978, *A&AS*, 35, 23  
 Araya, E., Hofner, P., Goss, W. M., Linz, H., Kurtz, S., & Olmi, L. 2007, *ApJS*, 170, 152  
 Araya, E., Hofner, P., Kurtz, S., Bronfman, L., & DeDeo, S. 2005, *ApJS*, 157, 279  
 Argon, A. L., Reid, M. J., & Menten, K. M. 2000, *ApJS*, 129, 159  
 Arikawa, Y., Tatematsu, K., Sekimoto, Y., & Takahashi, T. 1999, *PASJ*, 51, L7  
 Becker, R. H., White, R. L., Helfand, D. J., & Zoonematkermani, S. 1994, *ApJS*, 91, 347  
 Bertsch, D. L., Dame, T. M., Fichtel, C. E., Hunter, S. D., Sreekumar, P., Stacy, J. G., & Thaddeus, P. 1993, *ApJ*, 416, 587  
 Bhatnagar, S. 2002, *MNRAS*, 332, 1  
 Bitran, M., Alvarez, H., Bronfman, L., May, J., & Thaddeus, P. 1997, *A&AS*, 125, 99  
 Blum, R. D., Damineli, A., & Conti, P. S. 2001, *AJ*, 121, 3149  
 Brand, J. et al. 1994, *A&AS*, 103, 541  
 Brand, J., & Blitz, L. 1993, *A&A*, 275, 67  
 Brisken, W. F., Carrillo-Barragán, M., Kurtz, S., & Finley, J. P. 2006, *ApJ*, 652, 554  
 Brogan, C. L., Gelfand, J. D., Gaensler, B. M., Kassim, N. E., & Lazio, T. J. W. 2006, *ApJ*, 639, L25  
 Bronfman, L., Nyman, L.-Å., & May, J. 1996, *A&AS*, 115, 81  
 Caswell, J. L. 1996, *MNRAS*, 283, 606  
 Caswell, J. L. 1997, *MNRAS*, 289, 203  
 Caswell, J. L. 1998, *MNRAS*, 297, 215  
 Caswell, J. L. 2004, *MNRAS*, 352, 101  
 Caswell, J. L., & Haynes, R. F. 1987, *A&A*, 171, 261  
 Caswell, J. L., Haynes, R. F., Goss, W. M., & Mebold, U. 1981, *Aust. J. Phys.*, 34, 333  
 Caswell, J. L., Gardner, F. F., Norris, R. P., Wellington, K. J., McCutcheon, W. H., & Peng, R. S. 1993, *MNRAS*, 260, 425  
 Caswell, J. L., Vaile, R. A., Ellingsen, S. P., Whiteoak, J. B., & Norris, R. P. 1995, *MNRAS*, 272, 96  
 Chan, S. J., Henning, Th., & Schreyer, K. 1996, *A&AS*, 115, 285  
 Chapman, J. M., Leitherer, C., Koribalski, B., Bouter, R., & Storey, M. 1999, *ApJ*, 518, 890  
 Churchwell, E., Walmsley, C. M., & Cesaroni, R. 1990, *A&AS*, 83, 119  
 Claussen, M. J., Frail, D. A., Goss, W. M., & Gaume, R. A. 1997, *ApJ*, 489, 143  
 Clifton, T. R., & Lyne, A. G. 1986, *Nature*, 320, 43  
 Cohen, R. J., Masheder, M. R. W., & Caswell, J. L. 1995, *MNRAS*, 274, 808  
 Corbel, S., & Eikenberry, S. S. 2004, *A&A*, 419, 191  
 Corbel, S., Wallyn, P., Dame, T. M., Durouchoux, P., Mahoney, W. A., Vilhu, O., & Grindlay, J. E. 1997, *ApJ*, 478, 624  
 Cram, L. E., Claussen, M. J., Beasley, A. J., Gray, A. D., & Goss, W. M. 1996, *MNRAS*, 280, 1110  
 De Pree, C. G., Gaume, R. A., Goss, W. M., & Claussen, M. J. 1996, *ApJ*, 464, 788  
 Dickel, J. R., & Milne, D. K. 1972, *Aust. J. Phys.*, 25, 539  
 Dobashi, K., Yonekura, Y., Matsumoto, T., Momose, M., Sato, F., Bernard, J.-P., & Ogawa, H. 2001, *PASJ*, 53, 85  
 Downes, D., Wilson, T. L., Bieging, J., & Wink, J. 1980, *A&AS*, 40, 379  
 Felli, M., Testi, L., Schuller, F., & Omont, A. 2002, *A&A*, 392, 971  
 Finley, J. P., & Ögelman, H. 1994, *ApJ*, 434, L25  
 Fontani, F., Beltrán, M. T., Brand, J., Cesaroni, R., Testi, L., Molinari, S., & Walmsley, C. M. 2005, *A&A*, 432, 921  
 Frail, D. A., Goss, W. M., Reynoso, E. M., Giacani, E. B., Green, A. J., & Otrupcek, R. 1996, *AJ*, 111, 1651  
 Frail, D. A., Goss, W. M., & Slysh, V. I. 1994a, *ApJ*, 424, L111  
 Frail, D. A., Goss, W. M., & Whiteoak, J. B. Z. 1994b, *ApJ*, 437, 781  
 Fukui, Y., et al. 2006, *Science*, 314, 106  
 Fukui, Y., Iguchi, T., Kaifu, N., Chikada, Y., Morimoto, M., Nagane, K., Miyazawa, K., & Miyaji, T. 1977, *PASJ*, 29, 643  
 Gardner, F. F., & Whiteoak, J. B. 1984, *MNRAS*, 210, 23  
 Gensheimer, P. D., Mauersberger, R., & Wilson, T. L. 1996, *A&A*, 314, 281  
 Ghosh, S. K., Iyengar, K. V. K., Rengarajan, T. N., Tandon, S. N., Verma, R. P., Daniel, R. R., & Ho, P. T. P. 1989, *ApJ*, 347, 338  
 Goudis, C. 1976, *Ap&SS*, 45, 133  
 Gray, A. D. 1994, *MNRAS*, 270, 847  
 Green, D. A. 2004, *Bull. Astron. Soc. India*, 32, 335  
 Güsten, R., & Henkel, C. 1983, *A&A*, 125, 136  
 Güsten, R., & Philipp, S. D. 2004, in *The Dense Interstellar Medium in Galaxies: Proc. the Fourth Cologne-Bonn-Zermatt Symposium*, ed. S. Pfalzner et al. (Berlin: Springer), 253  
 Habing, H. J., Olnon, F. M., Winnberg, A., Matthews, H. E., & Baud, B. 1983, *A&A*, 128, 230  
 Handa, T., Sofue, Y., Nakai, N., Hirabayashi, H., & Inoue, M. 1987, *PASJ*, 39, 709  
 Healy, K. R., Hester, J. J., & Claussen, M. J. 2004, *ApJ*, 610, 835  
 Hinz, J. L., Rieke, G. H., Yusef-Zadeh, F., Hewitt, J., Balog, Z., & Block, M. 2009, *ApJS*, 181, 227  
 Hofner, P., & Churchwell, E. 1996, *A&AS*, 120, 283  
 Hofner, P., Wyrowski, F., Walmsley, C. M., & Churchwell, E. 2000, *ApJ*, 536, 393  
 Hüttemeister, S., Dahmen, G., Mauersberger, R., Henkel, C., Wilson, T. L., & Martín-Pintado, J. 1998, *A&A*, 334, 646  
 Hüttemeister, S., Wilson, T. L., Bania, T. M., & Martín-Pintado, J. 1993, *A&A*, 280, 255  
 Kalberla, P. M. W., Goss, W. M., & Wilson, T. L. 1982, *A&A*, 106, 167  
 Kassim, N. E., Baum, S. A., & Weiler, K. W. 1991, *ApJ*, 374, 212  
 Kassim, N. E., & Weiler, K. W. 1990, *ApJ*, 360, 184  
 Kerr, F. J. 1967, in *IAU Symp. 31, Radio Astronomy and the Galactic System*, ed. H. van Woerden (London: Academic Press), 239  
 Kim, H.-D., Balasubramanyam, R., & Burton, M. G. 2002, *Publ. Astron. Soc. Aust.*, 19, 505  
 Kim, K.-T., & Koo, B.-C. 2001, *ApJ*, 549, 979  
 Kim, K.-T., & Koo, B.-C. 2002, *ApJ*, 575, 327

- Koo, B.-C., Kim, K.-T., Lee, H.-G., Yun, M.-S., & Ho, P. T. P. 1996, *ApJ*, 456, 662
- Koralesky, B., Frail, D. A., Goss, W. M., Claussen, M. J., & Green, A. J. 1998, *AJ*, 116, 1323
- Kuchar, T. A., & Clark, F. O. 1997, *ApJ*, 488, 224
- Kurtz, S., & Hofner, P. 2005, *AJ*, 130, 711
- LaRosa, T. N., Kassim, N. E., Lazio, T. J. W., & Hyman, S. D. 2000, *AJ*, 119, 207
- Liszt, H. S. 1992, *ApJS*, 82, 495
- Lockman, F. J. 1989, *ApJS*, 71, 469
- Lockman, F. J., Pisano, D. J., & Howard, G. J. 1996, *ApJ*, 472, 173
- Lynds, B. T., Canzian, B. J., & O'Neil, E. J., Jr. 1985, *ApJ*, 288, 164
- Martin, C. L., Walsh, W. M., Xiao, K., Lane, A. P., Walker, C. K., & Stark, A. A. 2004, *ApJS*, 150, 239
- Martín-Hernández, N. L., van der Hulst, J. M., & Tielens, A. G. G. M. 2003, *A&A*, 407, 957
- Miettinen, O., Harju, J., Haikala, L. K., & Pomrén, C. 2006, *A&A*, 460, 721
- Milne, D. K. 1970, *Australian J. Phys.*, 23, 425
- Mizuno, A., & Fukui, Y. 2004, *ASP Conf. Ser.*, 317, 59
- Morris, M., 2006, *J. Phys. Conf. Ser.*, 54, 1
- Morris, M., & Serabyn, E. 1996, *ARA&A*, 34, 645
- Murakami, H., et al. 2007, *PASJ*, 59, S369
- Odegard, N. 1986, *AJ*, 92, 1372
- Ogawa, H., Mizuno, A., Hoko, H., Ishikawa, H., & Fukui, Y. 1990, *Int. J. Infrared Millimeter Waves*, 11, 717
- Ojeda-May, P., Kurtz, S. E., Rodríguez, L. F., Arthur, S. J., & Velázquez, P. F. 2002, *Rev. Mex. Astron. Astrofis.*, 38, 111
- Oka, T., Hasegawa, T., Sato, F., Tsuboi, M., & Miyazaki, A. 1998, *ApJS*, 118, 455
- Pestalozzi, M. R., Minier, V., & Booth, R. S. 2005, *A&A*, 432, 737
- Pirogov, L., Zinchenko, I., Caselli, P., Johansson, L. E. B., & Myers, P. C. 2003, *A&A*, 405, 639
- Planesas, P., Gómez-González, J., Rodríguez, L. F., & Cantó, J. 1991, *Rev. Mex. Astron. Astrofis.*, 22, 19
- Plume, R., Jaffe, D. T., & Evans, N. J., II 1992, *ApJS*, 78, 505
- Pottasch, S. R., Bignell, C., Olling, R., & Zijlstra, A. A. 1988, *A&A*, 205, 248
- Ramírez, S. V., Arendt, R. G., Sellgren, K., Stolovy, S. R., Cotera, A., Smith, H. A., & Yusef-Zadeh, F. 2008, *ApJS*, 175, 147
- Rodríguez-Fernández, N. J., & Martín-Pintado, J. 2005, *A&A*, 429, 923
- Russeil, D., & Castets, A. 2004, *A&A*, 417, 107
- Sawada, T., et al. 2001, *ApJS*, 136, 189
- Scoville, N. Z., Solomon, P. M., & Penzias, A. A. 1975, *ApJ*, 201, 352
- Sewilo, M., Churchwell, E., Kurtz, S., Goss, W. M., & Hofner, P. 2004, *ApJ*, 605, 285
- Shaver, P. A., & Goss, W. M. 1970, *Aust. J. Phys. Astrophys. Suppl.*, 14, 77
- Shaver, P. A., Pottasch, S. R., Salter, C. J., Patnaik, A. R., van Gorkom, J. H., & Hunt, G. C. 1985b, *A&A*, 147, L23
- Shaver, P. A., Salter, C. J., Patnaik, A. R., van Gorkom, J. H., & Hunt, G. C. 1985a, *Nature*, 313, 113
- Slysh, V. I., Val'tts, I. E., Kalenskii, S. V., Voronkov, M. A., Palagi, F., Tofani, G., & Catarzi, M. 1999, *A&AS*, 134, 115
- Stark, A. A. 1984, *ApJ*, 281, 624
- Stewart, R. T., Haynes, R. F., Gray, A. D., & Reich, W. 1994, *ApJ*, 432, L39
- Sung, H., Chun, M.-Y., & Bessell, M. S. 2000, *AJ*, 120, 333
- Szymczak, M., Hrynek, G., & Kus, A. J. 2000, *A&AS*, 143, 269
- Taylor, G. B., Morris, M., & Schulman, E. 1993, *AJ*, 106, 1978
- te Lintel Hekkert, P., Versteeghe-Hensel, H. A., Habing, H. J., & Wiertz, M. 1989, *A&AS*, 78, 399
- Torii, K., et al. 2009, *PASJ* submitted
- Tsuboi, M., Handa, T., & Ukita, N. 1999, *ApJS*, 120, 1
- Val'tts, I. E., Ellingsen, S. P., Slysh, V. I., Kalenskii, S. V., Otrupcek, R., & Larionov, G. M. 2000, *MNRAS*, 317, 315
- van der Walt, D. J., Retief, S. J. P., Gaylard, M. J., & MacLeod, G. C. 1996, *MNRAS*, 282, 1085
- Walsh, A. J., Burton, M. G., Hyland, A. R., & Robinson, G. 1998, *MNRAS*, 301, 640
- Walsh, A. J., Hyland, A. R., Robinson, G., & Burton, M. G. 1997, *MNRAS*, 291, 261
- Wardle, M., & Yusef-Zadeh, F. 2002, *Science*, 296, 2350
- Whiteoak, J. B. Z., & Green, A. J. 1996, *A&AS*, 118, 329
- Whiteoak, J. B., Otrupcek, R. E., & Rennie, C. J. 1982, *Proc. Astron. Soc. Aust.*, 4, 434
- Wilson, T. L. 1974, *A&A*, 31, 83
- Wink, J. E., Wilson, T. L., & Bieging, J. H. 1983, *A&A*, 127, 211
- Wood, D. O. S., & Churchwell, E. 1989, *ApJ*, 340, 265
- Yusef-Zadeh, F., Goss, W. M., Roberts, D. A., Robinson, B., & Frail, D. A. 1999, *ApJ*, 527, 172
- Yusef-Zadeh, F., Uchida, K. I., & Roberts, D. 1995, *Science*, 270, 1801
- Yusef-Zadeh, F., Wardle, M., & Roberts, D. A. 2003, *ApJ*, 583, 267
- Zinchenko, I., Henkel, C., & Mao, R. Q. 2000, *A&A*, 361, 1079
- Zoonematkermani, S., Helfand, D. J., Becker, R. H., White, R. L., & Perley, R. A. 1990, *ApJS*, 74, 181